

2015-08-24

A Mobile MEMS-based Sensors System for Ubiquitous Personal Navigation

Zhao, Xing

Zhao, X. (2015). A Mobile MEMS-based Sensors System for Ubiquitous Personal Navigation (Doctoral thesis, University of Calgary, Calgary, Canada). Retrieved from <https://prism.ucalgary.ca>. doi:10.11575/PRISM/24793

<http://hdl.handle.net/11023/2405>

Downloaded from PRISM Repository, University of Calgary

UNIVERSITY OF CALGARY

A Mobile MEMS-based Sensors System for Ubiquitous Personal Navigation

by

Xing Zhao

A THESIS

SUBMITTED TO THE FACULTY OF GRADUATE STUDIES
IN PARTIAL FULFILMENT OF THE REQUIREMENTS FOR THE
DEGREE OF DOCTOR OF PHILOSOPHY

GRADUATE PROGRAM IN GEOMATICS ENGINEERING

CALGARY, ALBERTA

AUGUST, 2015

© Xing Zhao 2015

Abstract

Global Navigation Satellite Systems (GNSS) are widely used for most navigation applications. However, GNSS quality and availability suffer greatly in certain environments, such as urban canyons, or indoors due to signal blockage. This thesis investigates estimation algorithms to integrate data from multiple MEMS sensors in a low-cost personal navigation system to bridge those signal gaps.

MEMS-based accelerometer, gyroscope, magnetometer, and barometer sensor technologies are surveyed in depth. The main MEMS sensor design parameters and their connection to navigation performance are presented. Major error sources from the mechanical Brownian motion of the MEMS mass and electronics noise in the readout circuitry are analyzed. Furthermore, this thesis presents a way of decomposing the sensor error terms then applying proper stochastic and deterministic error models. Subsequently, navigation estimation states and online calibration methods are elaborated accordingly.

Several key sensors-based positioning algorithms are explored in this thesis. First, a nine-axis fusion engine of accelerometers, gyroscopes, and magnetometers is formulated into an attitude Kalman filter for orientation determination. Then a Pedestrian Dead Reckoning (PDR) algorithm is developed based on the accelerometer's step detection and stride length estimation with the heading determined from the attitude fusion filter. In addition, Wi-Fi positioning is investigated for indoor environments based on received signal strengths. Finally altitude integration of the barometer and GPS height measurements is introduced to improve vertical position accuracy. The complete navigation system is constructed using an Extended Kalman Filter (EKF) to perform the data fusion from multiple positioning above. This thesis introduced the observability analysis for quantitative analysis about the degree of observability of each

estimated state; hence more insights of navigation solutions using different sensors configurations can be obtained.

Field tests are presented to verify the system and developed algorithms using three different portable navigation prototypes. The first prototype explores optimal integration of the PDR and GPS for a continuous positioning solution. The second prototype is focused on Wi-Fi assistance when GPS is not available in deep indoor environments. The third prototype is a more compact form factor design that mimics the smartphone experience in real-life applications. The test trajectories include various outdoor and indoor pedestrian navigation scenarios. The results show that the prototype systems can effectively deal with short GPS signal outages and correctly estimate navigation states online using EKF. Thus this thesis shows a cost effective design for a mobile, reliable and accurate system that enables continuous navigation anywhere.

Acknowledgements

I would like to express my sincere appreciation to many people who have helped me along my long journey of thesis study.

- My supervisor, Naser El-Sheimy, for giving me a promising thesis topic to work on; your continuous guidance and support are deeply appreciated. In particular, thanks for your endless encouragement and patience throughout my thesis work.
- I would also like to extend my gratitude to my supervisory committee Dr. O’Keefe and Dr. Aboelmagd Noureldin for their advice on my research and thesis. Thesis examiners Dr. Swavik Spiewak and Dr. Allison Kealy are also appreciated for their valuable suggestion.
- My gratitude goes for my family: my parents Renxin Zhao, Daoxun Shi, my wife Ruiling Yuan and son Jiayuan Zhao. Your unconditional support and love are beyond what words can express. The completion of this thesis is a small reflection of what you have empowered me to become.
- Thanks to all of my dear colleagues and classmates at the University of Calgary for their friendship, support, and assistance in many aspects of the study; In particular, Dr. Zainab Syed, Dr. Chris Goodall, Dr. Peng Xie, Mr. Bruce Wright, Mr. Hang Liu, Dr. XiaoJi Niu, Dr. Hsui-wen Chang, Dr. Sara Saeedi, Dr. Mohamed Atia, Dr. Adel Moussa, Dr. Abdelrahman Ali, Dr. Wesley Tesky, Mr. Siddharth, Dr. Tao lin.
- Finally thanks to following parties for research funding support: Tecterra, the Natural Science and Engineering Research Council of Canada (NSERC) and Geomatics for Informed Decisions (GEOIDE), Network Centers of Excellence (NCE).

Dedication

To my parents, Daoxun Shi and Renxin Zhao

To my wife Ruiling Yuan

To my son Jiayuan Zhao

Table of Contents

Abstract	ii
Acknowledgements	iv
Dedication	v
Table of Contents	vi
List of Tables	ix
List of Figures and Illustrations	x
List of Abbreviations	xiii
List of Symbols and Nomenclature	xvi
CHAPTER ONE: INTRODUCTION	1
1.1 Background	1
1.2 Literature Review on PNS Solutions	3
1.3 Research Objectives	7
1.4 Dissertation Outline	8
CHAPTER TWO: PERSONAL NAVIGATION SYSTEMS OVERVIEW	11
2.1 GNSS Overview	12
2.2 Motion Sensors in Navigation System	17
2.3 Wireless Positioning System	18
2.3.1 Introduction	18
2.3.2 Indoor Radio Propagation Modeling	21
2.3.3 Received Signal Fluctuation	24
2.3.4 Wi-Fi Positioning Algorithm	26
2.4 Altitude Integration	28
2.4.1 Height Definition	29
2.4.2 Conversion from Pressure to Height	30
2.5 Other Aiding Sensors	31
2.6 Choice of Suitable Technology	32
CHAPTER THREE: MODELING AND CALIBRATION OF MEMS SENSORS	35
3.1 Gyroscope scope Design Analysis	36
3.1.1 Operation Principle	36
3.1.2 Gyroscope Parameters Design Analysis	40
3.1.2.1 Resolution and Noise Performance	40
3.1.2.2 Bias	43
3.1.2.3 Environment Sensitivity	44
3.2 Gyro Error Modeling	46
3.3 Gyroscope Noise Analysis	50
3.4 Sensors Calibration	58
3.4.1 Gyro Online Calibration	60
3.4.2 Magnetometer Online Calibration	61
CHAPTER FOUR: ATTITUDE SENSORS FUSION	68
4.1 Attitude Kalman Filter Design	68
4.1.1 The State Equation	68

4.1.2 Kalman Filter Processing Flow	73
4.1.2.1 Filter Initialization	75
4.1.3 Discrete-time State Equations	77
4.1.3.1 Quaternion Propagation	77
4.1.3.2 State Transition Equations	79
4.1.3.3 Process Noise Covariance	80
4.1.3.4 State Covariance Matrix	81
4.1.4 Measurement Update	82
4.1.4.1 Accelerometer Measurement	82
4.1.4.2 Magnetometer Measurement	84
4.1.4.3 Measurement Noise and Adaptive Selection	85
4.1.4.4 Kalman Filter Gain Matrix	86
4.1.4.5 State and Covariance Update	87
4.2 Attitude Fusion Test	88
4.2.1 Rotation Test Setup	88
4.2.2 Rotation Test Result	89
CHAPTER FIVE: HYBRID PERSONAL NAVIGATION ALGORITHMS	97
5.1 Pedestrian Dead Reckoning Mechanization	97
5.1.1 Step Detection	98
5.1.2 Stride Length Estimation	101
5.1.3 Pedestrian Dead Reckoning	102
5.2 Kalman Filter Integration and State Selection	104
5.2.1 Kalman Filter Integration	104
5.2.2 Pedestrian Navigation System Error Models	106
5.2.3 Integrity Monitoring	112
5.3 Observability Analysis and State Selection for PNS	114
5.3.1 Analysis of Observability and Observable Degree	115
5.3.2 Observability Analysis Procedure for Pedestrian Navigation System	120
5.4 Altitude Integration	127
5.4.1 GPS/Barometer Height Fusion	128
5.4.2 Height Fusion Test Result	129
5.5 Wi-Fi Positioning for Indoor Environment	130
5.5.1 Indoor Wi-Fi Signal Propagation Modeling	130
5.5.2 Wi-Fi Positioning Field Test	133
CHAPTER SIX: MULTI-SYSTEM INTEGRATION AND PROTOTYPING	137
6.1 First Prototype: GPS-Sensor Integration	138
6.1.1 System Introduction	138
6.1.2 Results	139
6.2 Second Prototype: Wi-Fi-GPS-Sensor Integration	141
6.2.1 System Introduction	141
6.2.2 Results	142
6.3 Third Prototype: Consumer Grade Multi-Sensors System	145
6.3.1 System Introduction	145
6.3.2 Orientation Alignment	146
6.3.3 Results	148

CHAPTER SEVEN: CONCLUSIONS AND RECOMMENDATIONS	153
7.1 Conclusions.....	153
7.2 Contributions.....	157
7.3 Recommendations for Future Work.....	158
REFERENCES	160
APPENDIX A: MEMS SENSORS FABRICATION.....	174
APPENDIX B: MEMS SENSORS OPERATION PRINCIPLE.....	178
B.1 MEMS Sensors: State-of-the-art and Future Trend.....	179
B.2 Sensor Operation Principle	183
B.2.1 Accelerometers	183
B.2.2 Gyroscopes.....	188
B.2.3 Magnetometers	194
B.2.4 Barometer.....	198
APPENDIX C: ATTITUDE REPRESENTATION	201
C.1 Coordinate Definition	201
C.1.1 Navigation Frame.....	201
C.1.2 Body Frame.....	203
C.2 Euler Angle	203
C.3 Direction Cosine Matrix and Rotation Matrix	205
C.4 Quaternions	207
C.5 Conversion between Quaternion, DCM and Euler Angles.....	209
C.5.1 Euler Angles -> DCM	209
C.5.2 DCM -> Euler Angles	210
C.5.3 Quaternion -> DCM	210
C.5.4 DCM -> Quaternion	210
C.5.5 Euler Angles -> Quaternion.....	212
C.5.6 Quaternion -> Euler Angles.....	212
APPENDIX D: EQUATION DERIVATIONS IN CHAPTER FOUR	213
D.1: Derivation of $\delta\dot{\vec{q}}(t)$	213
D.2: Derivation of Quaternion Transition Matrix.....	214
D.3: Derivation of State Transition Matrix Φ	216

List of Tables

Table 1-1 Literature review on PNS	4
Table 1-2 Thesis Contribution in relation to hypothesis questions.....	10
Table 2-1 Comparison of GNSS constellation	12
Table 2-2 Comparison of personal navigation technology	32
Table 3-1 Key parameters of consumer-grade MEMS gyroscopes.....	45
Table 4-1 Heading error comparison	96
Table 5-1 Three EKF configurations for PDR/GPS integration.....	107
Table 5-2 EKF based magnetometer DR/GPS integration (6-state).....	108
Table 5-3 EKF based gyro DR/GPS integration (9-state).....	110
Table 5-4 EKF based gyro DR/GPS integration (6-state).....	111
Table 5-5 Comparison of observability methods for time-variant system.....	120
Table 5-6 Observation matrix rank for three EKFs	121
Table 5-7 6-state magnetometer observability matrix SVD.....	122
Table 5-8 6-state gyro observability matrix SVD.....	124
Table 5-9 9-state gyro observability matrix SVD.....	125
Table 5-10 Radio propagation models for different scenarios	132
Table 5-11 Selected access point for positioning	136
Table 6-1 Maximum position drifts during GPS signal outage of 45 seconds.....	140
Table 6-2 Performance metrics for real-time EKF solution.....	145
Table 7-1 Thesis contribution and uniqueness	157
Table B-1 Comparison of IMU performance	180
Table C-1 Quaternion elements recalculation	211

List of Figures and Illustrations

Figure 1-1 Thesis organization	9
Figure 2-1 GPS satellite constellation.....	13
Figure 2-2 Generic GPS receiver architecture.....	15
Figure 2-3 SNR fluctuations with the time (LOS case)	25
Figure 2-4 SNR distribution histogram (LOS and NLOS case).....	26
Figure 2-5 Trilateration of Wi-Fi positioning.....	28
Figure 2-6 Illustration of three height definitions.....	30
Figure 3-1 A simplified model for Z-axis gyroscope.....	37
Figure 3-2 Block diagram of vibratory gyroscope.....	40
Figure 3-3 MEMS sensor error sources	47
Figure 3-4 Allan variance analysis of gyroscope.....	52
Figure 3-5 Filtered and raw gyroscope output.....	57
Figure 3-6 Filtered gyroscope autocorrelation plot	57
Figure 3-7 Allan variance plot of the filtered and raw gyroscope signals	58
Figure 3-8 Multiple orientation magnetometers calibration.....	64
Figure 3-9 Magnetometers output without calibration.....	64
Figure 3-10 Magnetometers calibration using first orientation	65
Figure 3-11 Magnetometers calibration using first and second orientation.....	66
Figure 3-12 Magnetometers calibration using first, second and third orientation.....	67
Figure 4-1 Kalman filter flow for 9-axis orientation fusion.....	75
Figure 4-2 Rotation test setup.....	89
Figure 4-3 Rotation test results of attitude Test1.....	90
Figure 4-4 Rotation test results of attitude Test2.....	91
Figure 4-5 Rotation test results of attitude Test3.....	93

Figure 4-6 Rotation test results of attitude Test4.....	94
Figure 4-7 Rotation test results of attitude Test5.....	95
Figure 5-1 Gait cycle analysis	98
Figure 5-2 Accelerometer signals during a gait cycle.....	99
Figure 5-3 Step detection	100
Figure 5-4 Linear regression of stride length estimation	101
Figure 5-5 Dead reckoning concept.....	103
Figure 5-6 Kalman filtering procedure.....	105
Figure 5-6 Measurement sequence in PWCS approximation.....	116
Figure 5-7 SVD for 6-state magnetometer (constant heading).....	122
Figure 5-8 SVD for 6-state gyro (constant heading).....	123
Figure 5-9 SVD for 6-state gyro (change ω).....	124
Figure 5-10 SVD for 9-state gyro (constant heading).....	125
Figure 5-11 SVD for 9-state gyro (change heading/ ω 1).....	126
Figure 5-12 SVD for 9-state gyro (change heading/ ω 2).....	126
Figure 5-13 Barometer/GPS height fusion comparison	130
Figure 5-14 Access point radio propagation modeling in different scenarios.....	131
Figure 5-15 Field test reference trajectory	134
Figure 5-16 Selected Wi-Fi access points	135
Figure 5-17 GPS + Wi-Fi solution after innovation testing	136
Figure 6-1 PNS system architecture.....	138
Figure 6-2 First prototype of portable navigation system.....	139
Figure 6-3 Illustration of the belt-mounted prototype unit.....	140
Figure 6-4 Field test solutions for outdoor navigation.....	141
Figure 6-5 Wi-Fi+GPS+IMU prototype system.....	142

Figure 6-6 Comparison of GPS/Wi-Fi/PDR stand-alone solutions	143
Figure 6-7 Real-time GPS/Wi-Fi/PDR EKF integrated solution	144
Figure 6-8 Third prototype	145
Figure 6-9 Illustration of misalignment angle	146
Figure 6-10 Testing environment and GPS position uncertainty	149
Figure 6-11 10-Axis MEMS sensors signals	149
Figure 6-12 Step detection and stride length estimation	150
Figure 6-13 Heading results comparison	151
Figure 6-14 Height results comparison	151
Figure 6-15 Positioning results comparison	152
Figure A-1 From wafer to IC: basic fabrication process	175
Figure B-1 Spring-mass-dashpot system	185
Figure B-2 A basic differential structure of accelerometer	187
Figure B-3 A simplified model for Z-axis gyroscope	189
Figure B-4 Block diagram of vibratory gyroscope	192
Figure B-5 Mechanical structure design of Coriolis vibrating gyroscope	192
Figure B-6 AMR sensor circuit	195
Figure B-7 Concept of magneto-impedance effect	196
Figure B-8 Hall effect principle	197
Figure B-9 Silicon fabrication of piezoresistive diaphragm	199
Figure C-1 East-North-Up (ENU) definition for navigation frame	202
Figure C-2 Right-Forward-Up (RFU) definition for body frame	203
Figure C-3 Roll, pitch and yaw definition	204
Figure C-4 Navigation to body frame transformation: yaw→pitch→roll sequence	206

List of Abbreviations

Symbol	Definition
AEKF	Additive Extended Kalman Filter
AGPS	Assisted GPS
AFLT	Advanced Forward Link Trilateration
AMR	Anisotropic Magneto-Resistance
AP	Access Point
ARW	Angular Random walk
BTS	Base Transceiver Station
BSS	Base Station System
BW	Bandwidth
CSR	Cambridge Silicon Radio
DCM	Direction Cosine Matrix
DOF	Degrees-Of-Freedom
DR	Dead Reckoning
EKF	Extended Kalman Filter
ENE Ω	Electrical Noise Equivalent Rotation
ENU	East-North-Up
FCC	Federal Communications Commission
FOG	Fiber Optic Gyroscopes
GMI	Giant Magneto-Impedance
GMR	Giant Magneto-Resistive
GNSS	Global Navigation Satellite Systems

IMU	Inertial measurement unit
IOT	Internet of Things
INS	Inertial Navigation System
LBS	Location-based services
LSB	Least Significant Bit
LOS	Line-Of-Sight
LPF	Low-Pass Filter
MEKF	Multiplicative EKF
MEMS	Micro-Electro-Mechanical Systems
MMSS	Mobile Multi-Sensor Systems
MNE Ω	Mechanical Noise Equivalent Rotation
MS	Mobile Station
NED	North-East-Down
NLOS	Non-Line-Of-Sight
PLL	Phase-Locked Loop
PNS	Personal Navigation Systems
PSD	Power Spectrum Density
PWCS	Piece-Wise Constant Systems
RFU	Right-Forward-Up
TA	Timing Advance
TDOA	Time Difference Of Arrival
TFG	Tuning Fork Gyroscope
TNEA	Total Noise Equivalent Acceleration

TNEΩ	Total Noise Equivalent Rotation
TOA	Time Of Arrival
TOM	Total Observability Matrix
TPI	Trusted Positioning Inc.
TTFF	Time To First Fix
SSID	Service Set IDentifier
STM	STMicroelectronics
SVD	Singular Value Decomposition
RMS	Root Mean Square
RSS	Received Signal Strength
WCL	Weighted Centroid Localization
ZRO	Zero-Rate Output
ZUPT	Zero velocity UPdaTe

List of Symbols and Nomenclature

Symbol	Definition
\otimes	Multiplication of quaternions
Ω	Angular velocity vector with respect to the rotating frame
$[\hat{\omega}\times]$	cross product or skew symmetric matrix form of ω
Φ	transition matrix
ρ	pseudo range
η_v	a white-noise process of vector v
$\delta\alpha$	attitude vector of roll, pitch, and yaw error
δb	gyro bias error vector
γ	sensor scale factor
$\sigma^2(T)$	Allan variance of cluster time T
C_b^n	rotation matrix from the body frame to the navigation frame
$E(x)$	expectation of x
F	dynamics matrix of the state transition
H	design matrix for measurements
I	identity matrix
K	Kalman gain matrix
O	observability matrix of the state
P	covariance matrix of state vector
\bar{q}	notation for quaternions defined as $q_1i + q_2j + q_3k + q_4$
\bar{q}^*	The conjugate quaternions
\bar{q}^{-1}	inverse quaternions

Q_k	covariance matrix of system noise sequence vector
R	covariance matrix of measurement error vector
(R, P, H)	Roll, pitch, and yaw angles of the rotation
\mathbf{R}^3	three-dimensional Euclidean space
$S_{\Omega}(f)$	power spectrum density (PSD) of the rotational signal
T_c	time correlation constant
v	measurement noise vector
v^i	a vector viewed in the inertial frame-i
v^r	a vector viewed in the rotational frame-r
v^b	a vector resolved in the body fixed coordinate system
v^n	a vector resolved in the navigation frame
\mathbf{x}	state vector
x_k^-	state vector prediction at time epoch k
x_k^+	state vector at time epoch k after the measurement update
\hat{x}	estimated value of vector x
\mathbf{z}	measurement vector

Chapter One: INTRODUCTION

While vehicle navigation is a well-established service, Personal Navigation Systems (PNS) have just started to gain momentum fuelled by the proliferation of mobile applications, hardware evolution, and consumer adoption. Positioning systems and Location-Based Services (LBS) based on Global Navigation Satellite Systems (GNSS) are now commonly available. These systems provide absolute positions by using signals from satellites. However, navigation in GNSS-impeded environments, such as indoor areas and urban canyons, still remains a very challenging task. As such, this dissertation investigates hybrid-positioning methods using low-cost Micro-Electro-Mechanical System (MEMS) sensors and Wi-Fi positioning integrated with GNSS. By exploring the nature of these complimentary systems and combining their location data with fusion algorithms, positioning systems can provide a cost-efficient solution that enables seamless and accurate positioning everywhere.

1.1 Background

LBS have become more pervasive with emerging applications focused on navigation, social networking, asset tracking, and people positioning functions. On the other hand, today's mobile devices, such as smartphones and smart wearable devices, are equipped with more powerful processors, better connectivity, GNSS chipsets, and various MEMS sensors. Therefore, a new era of hybrid data fusion is coming for a ubiquitous, accurate, and reliable positioning solution. GNSS based devices are still the dominant solution for these navigation applications. However, GNSS signal reception requires direct line of sight to the satellites in the sky, which are not always available and this poses a great deal of challenge for the weak-signal environments such

as dense urban canyons, under tree canopies, and indoors. To overcome this obstacle, multiple complementary navigation technologies are integrated together for a seamless navigation. Propelled by the rapid development of low-cost MEMS technology, MEMS sensors have greatly penetrated many devices ranging from popular handsets, such as smartphones and tablets, to gaming consoles, remote controllers, cameras, and wearable devices, to name a few. This thesis aims to utilize the state-of-the-art and low-cost MEMS sensors including three-axis accelerometers, gyroscopes, magnetometers, and barometer to explore their potentials for positioning. Such configuration, sometimes called 10-DOF (Degrees-Of-Freedom) sensor combination, provides more accurate measurements of linear and angular motion in three-dimensional space.

To get better indoor location information, some major players in the industry use wireless infrastructure systems based on RF fingerprinting, Assisted-GPS/Advanced Forward Link Trilateration (A-GPS/AFLT), and beacon technologies. In this thesis, Wi-Fi positioning is selected as an absolute positioning update when GNSS signals are blocked. For one reason, Wi-Fi embedded devices are very popular in many mobile devices; moreover, Wi-Fi hotspots have already covered many densely populated urban and suburban areas such as airports, schools, and shopping malls, so the operation cost is less than other technologies.

Embedded mobile systems always have some constraints in practical development. For example, low-cost parts selection, dimension and weight limitations, and power consumption constraints. All these factors impose challenges on positioning performance. In addition, gathering and processing location data in real-time for navigation purposes imposes some limitations that are not often considered in scenarios where post-processing is an option [Petovello 2003].

Computation overhead, memory space, and processing latency are all important factors to

consider. This thesis takes all these limitations into account and investigates the appropriate algorithms for multiple sensor fusion under varying circumstances.

The FCC identifies indoor location positioning as a critical safety concern for E911 emergency responses. In 2014, the FCC proposed these positioning accuracy requirements [FCC 2014]:

- 50 meters horizontally (x,y-axis), with a reliability threshold of 67 percent.
- 3 meters vertically (z-axis), with a reliability threshold of 67 percent.

The reliability threshold of 67% above means that location results fall within the acceptable accuracy range 67% of the time. This thesis targets the exploration of a cost-effective solution to meet this target. In other applications and services (transportation, tourism, game etc.), the positioning accuracy requirement for PNS vary from with sub-meter to tens of meters.

1.2 Literature Review on PNS Solutions

Over the last decade, there has been a growing interest in personal navigation systems, driven by market demand and electronics technology development. Table 1-1 presents reviews from the literature that can be representative to show the state-of-the-art research in this field. Of particular interest, the table summarizes the sensors configuration selected in the systems, highlights the uniqueness of the navigation algorithms, shows the achieved testing performances, and comments on some of the main characteristics.

Table 1-1 Literature review on PNS

Sensors Configuration	Algorithm Highlights	Accuracy	Comments	Reference
Triaxial gyro+accel+mag (InertiaCube3) GPS (LassenSQ)	- 15-state EKF mechanization - ZUPT for each stride as measurement - Magnetometer heading as measurement	Position error ~1% distance traveled	- Shoe mounted - Calibration - Navigation dual modes	-Intersense Inc. [Foxlin 2005]
Triaxial gyro+accel +mag + baro +GPS (Nastorm)	- Human motion algorithms using vertical accel (walk forward /backward/running/stop) - Terrain correlation algorithm	Position error ~1% distance traveled	-Mounts on wearer's belt -Step time interval to determine motion mode	-Honeywell Inc. [Soehren et al. 2008]
Triaxial mag (HMR3000) baro (PTB220) IMU (HG1700) OEM4 GPS	- Three operation modes (calibration/DR/Hybrid navigation) - Knowledge-based system for parameterization (ANN and fuzzy logic for stride length; EKF for gyro/mag stride direction integration)	CEP 3-5m for indoor	- Backpack configuration - Human locomotion pattern recognition - 2-D algorithm	-Ohio State University(OSU) [Moafipoor et al. 2008]
Triaxial gyro+accel+mag (Xsens) GPS (ublox)	- 3D quaternion-based orientation mechanization -Uses gravity and magnetic field vectors as measurement in static mode -Adaptive EKF	Position error <5% distance traveled	-Trunk mounted - 80% improvement with verification test	- École polytechnique fédérale de Lausanne (EPFL) [Tome & Yalak 2008]
Wi-Fi+ triaxial gyro+accel+mag	-2D strapdown navigation mechanization with ZUPT -Cascaded EKF heading/position integration -Wi-Fi fingerprinting (5 meter database)	Wi-Fi only: 3.2m std. Hybrid solution: 1.6m	-Shoe mounted - No GPS used	-German Aerospace Center (DLR) [Frank et al.2009]

Sensors Configuration	Algorithm Highlights	Accuracy	Comments	Reference
Wi-Fi+ triaxial gyro+accel+mag+ GPS/Glonass	<ul style="list-style-type: none"> - PDR algorithm using MEMS sensors - Crowd-sourced learning of Wi-Fi APs - Star-V high sensitivity GNSS - Star-Fusion Kalman filter 	accuracy exceeds 10m 50% (CEP).	-Good solution for smartphones	- Cambridge Silicon Radio (CSR) [Bullock 2012]
Wi-Fi+ triaxial gyro+accel+mag+ GPS on commercial smart phones and tablets	<ul style="list-style-type: none"> - Detect mode of transit (e.g. walk, vehicle, static, elevator) - Identify the device orientation changes 	< 17 m error for 5 mins of indoor navigation	<ul style="list-style-type: none"> - Good solution with different mode usage - Smartphone form factor 	- Trusted Positioning Inc.(TPI) [Syed 2013]

To sum up, there are a few inspirations from the PNS literature studied in this thesis. First of all, most systems in the references listed above adapt GPS and MEMS Inertial Navigation System (INS); additionally, some emerging sensor technologies such as magnetometers and barometer are included in the hardware configuration. Secondly, a few earlier systems [Foxlin 2005, Frank et al. 2009] use foot-mounted placement to implement Zero velocity Updates (ZUPT) in their navigation algorithms. It is an effective method to control the system position drift during GPS signal outages. Other user modes are being considered in more practical applications, such as backpack placement [Moafipoor et al. 2008], trunk mounting [Tome & Yalak 2008] and with mode transit between vehicle and pedestrian [Syed 2013]. Thirdly, Wi-Fi positioning is an effective alternative positioning method for GNSS denied area. Wi-Fi access point database is built either for fingerprinting method [Frank et al. 2009] or based on received signal strength method [Bullock 2012, Syed 2013]. Overall, as seen From Table 1-1, solutions from TPI and CSR showed the best robustness for a mass consumer product.

This thesis aims to address some gaps in the literature. First, unlike some legacy navigation systems using high-end MEMS sensors, this thesis focuses on inexpensive MEMS sensors for practical product development in the mass market. Therefore, analysis on low-cost sensors' error sources, modeling and efficient compensation methods and hybrid positioning algorithms for personal navigation are of interest. Secondly, the reference papers didn't provide implementation details on the sensors fusion algorithms of accelerometers, gyroscopes and magnetometers for three-dimensional attitude fusion. Thus this thesis will discuss in depth how the attitude fusion is derived; in addition, a framework of 3/6/9-axis attitude fusion is presented to flexible deployment of different motion sensors. Thirdly, to the best of the author's knowledge, observability analysis of the hybrid positioning system addressing pedestrian dynamics has not been well studied in the literature before. So this thesis will present method for quantitative observability analysis under a hybrid positioning Kalman filter integration.

In terms of achievable accuracy with GPS outage, all the results in the Table1-1 showed excellent accuracy for personal navigation. However, for practical deployment in mass production, there is still a lack of a standard universal benchmark for equivalent comparison since the results from field tests exhibit stochastic characteristics and are affected by hardware noise and many other environmental factors. In this thesis, several prototypes using selected algorithms will be verified under different sensors configurations to examine the robustness of the processing. The goal is to meet the FCC's E911 positioning accuracy specification (<50m horizontal error; <3m vertical error) in most GNSS challenging areas.

1.3 Research Objectives

The main objective of this thesis is to investigate the system and algorithms design for a cost-efficient mobile system for ubiquitous personal navigation in areas with weak or no GNSS signals. To this end, hybrid positioning system consisting of MEMS accelerometers, gyroscopes, magnetometers and barometer sensors are integrated with GNSS and Wi-Fi receiver as a complete solution. Such a system configuration can be found in many modern consumer electronics such as smartphones, smart wearable or other portable navigation devices.

In order to achieve this major objective, several algorithms design and implementation issues need to be studied throughout this thesis. Hence the main thesis objects are further categorized to address the following research questions individually.

- Sensors estimation issues

Question (1): What are the main error sources for very low-cost MEMS sensors? How to build suitable error models so that the estimation algorithms can be properly designed in Kalman filter?

Question (2) How to develop efficient on-line calibration methods for MEMS sensors used in personal navigation applications?

- Attitude estimation issue

Question (3) How to integrate MEMS sensors for attitude determination in pedestrian navigation?

Question (4) How to make the sensor configuration flexible and implementation efficient?

- System observability issue

Question (5) Given the dynamics of pedestrian navigation, how to evaluate and quantify the degree of observability?

Question (6) How will weak observability impact navigation performance?

- Navigation system integration issue

Question (7) Given a particular environment or application scenario, how to integrate the most appropriate navigation algorithms and subsystems for personal navigation?

The subsequent section will give an outline of thesis organization to answer the above research hypothesis.

1.4 Dissertation Outline

This thesis investigates the system and algorithm design of personal navigation system. Figure 1-1 summarizes the thesis organization.

Chapter 2 introduces different personal navigation systems based on GNSS, inertial navigation systems, wireless positioning, altitude fusion and various alternative assistances. In addition, MEMS sensor fabrication and operation principles are given in Appendix A and B.

Chapter 3 presents the technology of the emerging MEMS sensors including accelerometers, gyroscopes, magnetometers and barometer, and then the error modeling and calibration methods are discussed which lays the foundation for the system implementation at the device level. It handles the sensors estimation issues set in Section 1.3.

Chapter 4 deals with the attitude fusion of a navigation device. Attitude determination filter based on accelerometers, gyroscopes and magnetometers are formulated in a flexible configuration. Rotation tests results are demonstrated to compare the performance. Thus this

chapter solves the attitude estimation issue set in Section 1.3. More attitude representation details and mathematical derivation are introduced in Appendix C and D respectively.

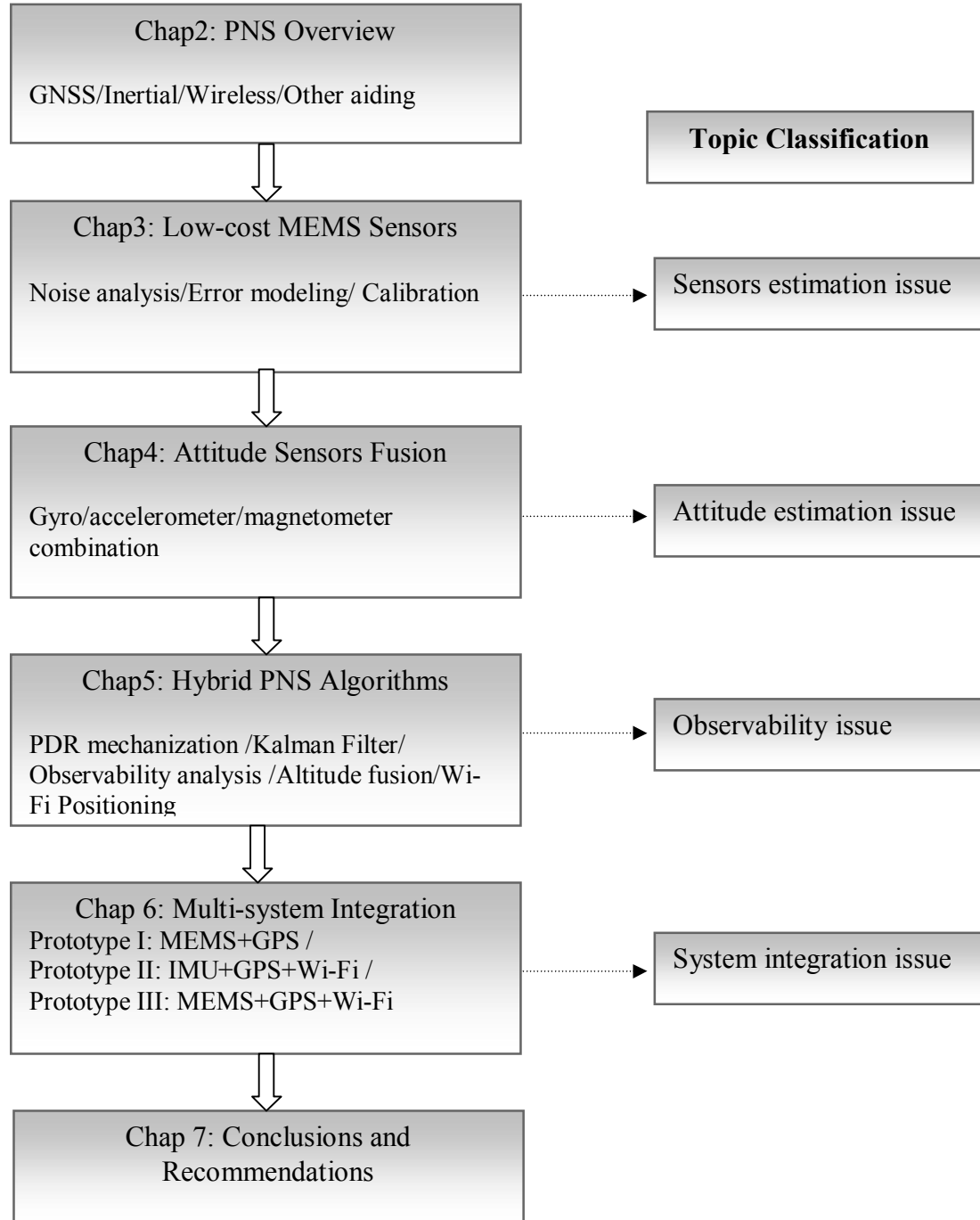


Figure 1-1 Thesis organization

Chapter 5 focuses on the essential PNS algorithm designs including PDR mechanization, system integration in a Kalman filter, Wi-Fi positioning methods for indoor environment, and a barometer-based altitude fusion with GPS height. All these hybrid positioning algorithms form the core navigation engine under a unified Kalman filter framework. A systematic observability analysis is introduced for optimal state selection and estimation enhancement. Therefore, observability issue set in Section 1.3 is tackled.

Chapter 6 illustrates three prototypes built at various stages of the research with different hardware configurations. Typical indoor and outdoor field test results are shown so practical system integration and implementation issues of the PNS are discussed.

Chapter 7 concludes the thesis contributions and uniqueness and gives recommendations for future work.

Table 1-2 summarizes the thesis contribution and its relationship addressing the thesis hypothesis questions set in this chapter.

Table 1-2 Thesis Contribution in relation to hypothesis questions

Contribution	Relation to the Thesis Hypothesis Questions
1. Analyze low-cost MEMS sensors error sources; then apply error modeling and calibration methods for estimation.	Address thesis hypothesis questions 1 and 2.
2. Develop algorithms for 3/6/9-axis motion sensors fusion for attitude determination.	Address thesis hypothesis questions 3 and 4.
3. Apply observability analysis for pedestrian dead reckoning integration with GPS/WiFi measurement.	Address thesis hypothesis questions 5 and 6.
4. Build a solution framework with 10-axis MEMS sensors, GPS and Wi-Fi, the system will adapt different subsystem according to application scenarios.	Address thesis hypothesis questions 7.

Chapter Two: **PERSONAL NAVIGATION SYSTEMS OVERVIEW**

This chapter will introduce a broad range of positioning technologies for personal navigation systems. Besides the popularly used GNSS, other potential alternative technologies suitable for personal navigation can be divided into four categories:

1. Motion sensors based navigation system, such as magnetometers, gyroscopes, accelerometers.
2. Wireless positioning system including cellular systems, Wi-Fi, digital TV, GNSS pseudolite and other short-range mobile radio signal of opportunities, such as Bluetooth beacon, NFC, etc.
3. Altimeter, such as barometer, that gives better vertical accuracy.
4. Feature matching systems, such as cameras, lasers, and map matching.

Considering what is available, accuracy, and cost factors for consumer products, each candidate technology has its strength and weakness. Motion sensing systems are self-contained, but the derived position drifts over time and the accuracy decreases for longer GNSS signal outages.

Wireless infrastructure-based systems have good global coverage in urban areas. However, lack of the required infrastructure information, like the cell tower and Wi-Fi access point positions, may be a major impediment. Short-range wireless systems are applicable for some niche markets with good accuracy; however, as the name suggests, the proximity approach depends on local availability of the system, thus these systems fail to cover large service areas. Image aiding systems can be very accurate; however they are relatively expensive and power hungry for mobile devices. Therefore each individual system faces some challenges and there is no clear standalone winner.

2.1 GNSS Overview

Global Navigation Satellite System (GNSS) technology encompasses a plurality of satellite-based navigation systems: Global Positioning System (GPS) has long been a standard feature in many modern devices not only for portable navigation devices but also in smartphones, tablets, and many other embedded devices. In addition to GPS, other satellite-based navigation systems have been deployed such as GLONASS by Russia, Beidou (Compass) by China, Galileo by the European Union, and regional systems including the Indian Regional Navigational Satellite System (IRNSS) by India and the Quasi-Zenith Satellite System (QZSS) by Japan[Agilent 2013]. Additional satellite coverage can improve in location determination and accuracy. The comparison of four major GNSS constellations is given in Table 2-1 with data up to date as of the first half of 2014[Langley 2014].

Table 2-1 Comparison of GNSS constellation

Constellation	Operational Satellites	Carrier Frequency	Baseband
GPS	8 IIA+ 12 IIR+ 7IIR-M + 4 IIFs = 31SVs	L1: 1575.42 MHz	1024-bit C/A-Code @1.023 Mbps, BPSK
Glonass	24 healthy GLO-M SVs	L1: 1602+ 0.5625*k MHz (K=-7~ +6)	511-bit M-Code, @511 Kbps, BPSK
Beidou	4 MEO+ 5 GEO + 5 IGSO =14 SVs	B1I: 1561.098 MHz	2046-bit random code @2.046 Mbps *20-bit N-H secondary code@1 kbps, QPSK
Galileo	4 SVs	E1: 1575.42MHz	4092-bit random code@ 1.023Mbps * 25-bit secondary code@ 250 bps , BOC

Since GPS is still the most popular system, this thesis will use GPS as the global positioning engine to integrate with other alternative technologies. The GPS space segment consists of a constellation of satellites transmitting radio signals to users. GPS satellites, also known as Satellite Vehicles (SV), fly in a Medium Earth Orbit (MEO) at an altitude of 20,200 km and inclination of 55 degrees with 12 hour periods approximately. The satellites in the GPS constellation are arranged into six equally-spaced, circular orbital planes surrounding the Earth, each containing four "slots" occupied by baseline satellites. GPS now effectively operates as a 27-slot constellation with improved coverage in most parts of the world, as depicted in Figure 2-1[GPS 2014].

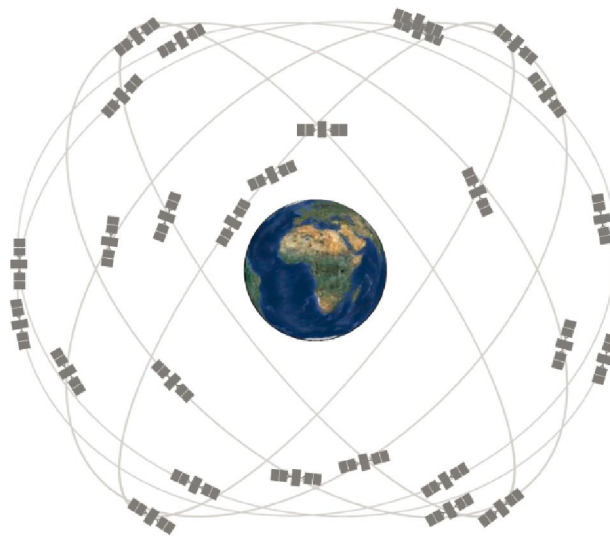


Figure 2-1 GPS satellite constellation

The control segment consists of a global network of ground stations that monitor and track the health and status of the GPS satellites. They send commands and navigational data to satellites in the constellation. The user segment consists of the GPS receivers that decode and process GPS satellite signals into position, velocity, and time estimates.

GPS uses a Coarse Acquisition (C/A) code for ranging, which is a Pseudo Random Noise (PRN) sequence that the satellite transmits to differentiate itself from other satellites in the active constellation. It repeats every 1023 bits or every one millisecond. This noise-like code modulates the L1 carrier signal, "spreading" the spectrum over a 1.023 MHz bandwidth. The Navigation Message is a 50 Hz signal consisting of data bits that describe the GPS satellite orbits, clock corrections, and other system parameters; it also modulates the L1-C/A code signal. Each GPS satellite in the constellation continuously transmits ephemeris data and almanac data. Ephemeris data parameters describe the precise orbit of the current satellite vehicle (SV) for approximately 30 minutes. Almanacs include approximate orbital data parameters for all SVs over extended periods of time and it can be several months old.

Figure 2-2 presents a general description of the signal processing modules in a GPS receiver [Seco-Granados 2012]. The GPS front end receives signals from the antenna, amplifies and filters them, and then down-converts them from the L-band frequency to an intermediate frequency. At the acquisition stage, the receiver searches for signals in both code delay and Doppler frequency drift. Once it has aligned the received code with the locally generated PRN code within less than half of the chip period, a fine carrier tracking loop takes over and keeps the code aligned, it enables a receiver to track and process carrier phase information in order to demodulate the navigation message data.

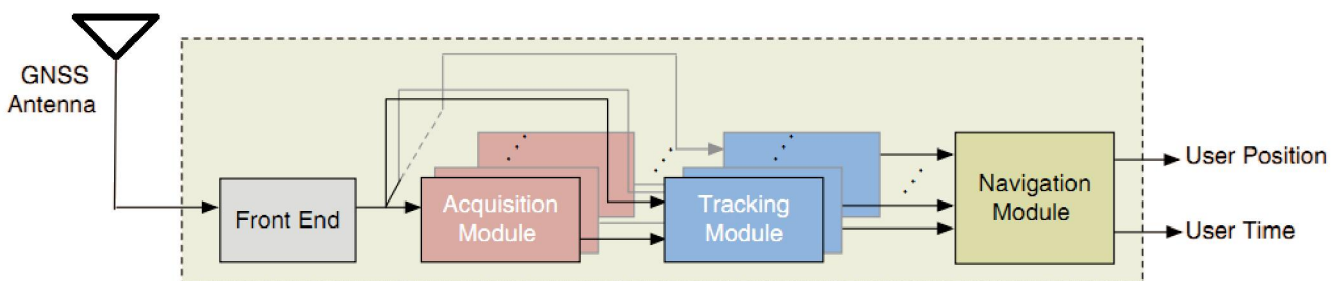


Figure 2-2 Generic GPS receiver architecture

A GPS receiver determines three unknown spatial coordinates (latitude, longitude and altitude) and clock bias in the navigation module shown in the above figure. The GPS pseudorange observation model for least-squares estimation [Lachapelle 2001] is:

$$P_i = \rho_i + C \cdot dt + \varepsilon_i \quad (2.1)$$

Where:

P_i is the pseudorange measurement

ρ_i is the geometric range between the satellite and the receiver

C is the speed of light in vacuum (299,792,458 m/s)

dt is the GPS receiver clock bias (common to all observations made at the same time),

and

ε_i is the combined effect of satellite orbit error, troposphere delay, ionosphere delay, multipath and noise, usually assumed as a zero-mean, uncorrelated and identically distributed Gaussian noise.

The range measurements can be further expanded as:

$$\rho_i = \sqrt{(x_i^s - x_{Rx})^2 + (y_i^s - y_{Rx})^2 + (z_i^s - z_{Rx})^2} \quad (2.2)$$

Where:

$(\dots)^s$ is the known coordinate of the satellite

i is based on the precise orbital elements (the ephemeris data) sent by each SV

$(\dots)_{Rx}$ is the unknown user coordinate

Positions are computed by the receiver in Earth-Centered, Earth-Fixed (ECEF) coordinates. In addition, Doppler shift of the satellite signal gives the range rate to each satellite, which can be used to determine the vehicle's velocity. Navigation algorithms such as least squares and the Kalman filter are most frequently used in GPS navigation solutions.

While GPS offers a ubiquitous, precise, and reliable positioning and timing service to the world, it has availability limitations for mobile platforms. Firstly, GPS works in open sky where at least four direct line-of-sight GPS satellite signals can be received. There are many difficult signal environments where satellite signals are too weak for acquisition and tracking. Also, GPS solutions are more error prone when object obstructs a direct line of sight between the receiver and satellites. These types of errors are known as multipath errors and cause jumps in location results. Thirdly, information from multiple satellites needs to be decoded, so it may take a substantial amount of time to acquire an initial location, a performance measurement known as Time-To-First-Fix (TTFF). Finally, power-efficiency is a critical challenge in any mobile device [Zhang 2012]: most receivers typically consume 20-40 mA in full-power operation with a 1.8 V supply. Low-power tracking modes can reduce the average power consumption to less than 10 mA, but at the expense of position accuracy.

High sensitivity GPS receivers have been developed to improve availability under difficult signal environments [MacGougan 2003]. Due to high bit error rates with weak signals, the receiver requires external assistance data for computation, such information includes a combination of approximate user position, ephemerides, almanac data, time, and the frequency of signals from the cellular platform. Such assisted GPS messages can reduce the TTFF and possibly increase the sensitivity of recorded data. The concentration of this thesis is not on the latest advancement

of GNSS receivers; rather, it explores alternative positioning methods for solutions in areas with weak GNSS signals.

2.2 Motion Sensors in Navigation System

Traditionally, MEMS sensors have been predominantly used in the automotive, industrial, and medical sectors. The recent availability of low cost, compact sized, and low power MEMS sensors have made these devices proliferate into consumer applications such as smartphones, tablets, gaming consoles, and wearable devices. Typical inertial navigation system (INS) consists of three orthogonal gyroscopes and three orthogonal accelerometers which are compulsory to capture the device's motion in a three dimensional space. The six-axis sensor configuration forms an inertial measurement unit (IMU) and is straightforward to generate position, velocity, and attitude from raw sensor data with respect to a non-accelerating frame. In practical deployment of the INS unit, however, the system can be working in many orientations. There is no way of guaranteeing that the sensors are placed perfectly aligned with the direction of travel. Therefore, strapdown INS mechanization algorithms are usually applied to transform the IMU measurements in the device's body frame into navigation quantities.

INS has several advantages. They are self-contained in that they have no requirement for an external infrastructure like a radio network; they provide a continuous navigation solution that is available anywhere, such as under foliage cover, in tunnels and inside buildings; and they are unaffected by any outside interference or jamming. However, due to the accuracy of the low-cost sensors used in consumer products, a standalone INS degrades with time and without bound.

Another limitation is that INS is a relative positioning method and it needs to be provided with an initial position to determine absolute location data.

Magnetometers offer complementary performance of INS by sensing the intensity and inclination of the Earth's magnetic field, thus determine a user's heading. There are many MEMS magnetic sensors that are small in size and low cost, perfect for mobile devices. The accuracy of derived azimuths from magnetic compasses depends heavily on the degree to which the local magnetic field is being disturbed. Local disturbances in Earth's magnetic field are caused by nearby permanent magnets, electric currents, or large iron bodies. When properly calibrated, heading accuracy can be on the order of a few degrees.

Yole Développement estimated the inertial MEMS sensors industry will reach \$5.4 billion by 2018, up from \$4 billion in 2013 [Yole 2013]. Combining MEMS accelerometers with gyroscopes, magnetometers, and a barometer allows for accurate computation of the position, velocity, acceleration, and altitude of the device. Integrating these with a GNSS receiver in the device empowers seamless outdoor and indoor navigation to become a reality. Appendix A gives more detailed introduction of MEMS sensors operation theory; Chapter 3 will analyze main MEMS errors then show methods for sensors error modeling and calibration to mitigate accuracy degradation.

2.3 Wireless Positioning System

2.3.1 Introduction

The basic task of most wireless communication systems is to transfer data from one terminal to others. However, by using characteristics of the transmitted signal itself, wireless

communications systems can be used as wireless positioning systems that determine a mobile device's location [Bensky 2008]. Positions are calculated using two main categories of wireless systems: network based and handset based. The latter is generally preferred for commercial roaming devices due to its convenience of implementation.

Positioning information can be obtained from cellular telephone systems. The main advantage of these systems is that the mobile handset is widely available at a low cost and the cellular infrastructure has the best coverage globally. By looking up the location of the unique cell ID of the cell tower that the handset is connected to at any given time, the handset can determine the cell tower's location and then estimate its approximate geographic location based off of the tower's signal strength. Since cellular base stations sometimes have very wide coverage, the location is very inaccurate. To improve cellular positioning performance, either the Time Of Arrival (TOA) or Time Difference Of Arrival (TDOA) of signals transmitted between the handset and the base stations can be used. For example, In GSM, a Timing Advance (TA) is used to compensate for the propagation delay as the signal travels between the Mobile Station (MS) and Base Transceiver Station (BTS). The timing advance value is based on the distance of the device to the cell tower, which is used to predict the time that the cell will receive a signal from the tower. The cell tower uses this TA prediction to sequential timeslots to the individual users sharing a frequency. If the BSS sees that the synchronization is late by 1 bit, then it knows that the two-way distance propagation delay is $3.69\mu\text{s}$, as the data throughput in GSM is 270.833 kb/s . Then we can determine the distance of the MS from the BTS as follows [GSM 2013]:

$$300\text{ m}/\mu\text{s} \times 3.69\mu\text{s}/2 = 553.5\text{m}$$

The Base Station System (BSS) assigns the TA to the MS based on how far away it perceives the MS to be. Then the BSS determines MS's location by combining the knowledge of the Cell-ID and the TA parameter.

The main disadvantage of cellular positioning systems is that the geometry of the base stations is optimized for communications, not positioning. As a result, the geometry may be very poor for positioning, resulting in degraded accuracies on the order of 100 m. Also, additional software or hardware may be required on the mobile phone network and handset.

Wi-Fi positioning is based on the measurements of Received Signal Strength (RSS) from the Access Point (AP). An AP broadcasts its Service Set Identifier (SSID) via packets known as beacons, which are usually every 100 ms in the 2.4/5 GHz frequency bands. There are two approaches using RSS. One class uses a signal propagation model to convert signal strength to a distance measurement from the AP. Trilateration can then be derived from multiple APs to provide final position fixes. The second class involves matching the real time signal strength measurements with surveyed database; this is known as location fingerprinting. The first approach is generally preferred in systems covering large-scale ranges. However, the main implementation issue is the lack of the geographic information of Wi-Fi APs. Therefore, the motivation of this thesis is to develop algorithms that can derive the AP coordinates by themselves; then the derived knowledge can be maintained locally on the device or remotely in a server.

Wi-Fi localization started to become an active research area about a decade ago. Bahl and Padmanabhan from Microsoft conducted the RADAR project [Bahl et al., 1999], which became the first RF wireless LAN system used for locating and tracking users inside a building. Later companies like Ekahau and Skyhook became pioneers in commercializing Wi-Fi positioning

systems. Ekahau provides a real-time location system for locating people, assets, and inventory indoors using Wi-Fi networks [Ekahau 2010]. It uses a method called multi-hypotheses tracking, which constantly calculates multiple possible location estimates for tracked objects and gives each possible location a numerical score. The location that receives the highest score is considered as the location estimate for wireless site survey. Skyhook maintains a massive worldwide database of known Wi-Fi access points. As of 2014, the reference network is comprised of over 800 million Wi-Fi access points and cellular towers in tens of thousands of cities and towns worldwide [Skyhook, 2014]. Then it provides hybrid-positioning engine configured to integrate and synthesize the location output of Wi-Fi Positioning System, GPS and cellular towers (Cell ID). In this thesis, Wi-Fi signal is selected as the main positioning assistance for indoor environment, the signal propagation modeling and positioning methods are discussed subsequently.

2.3.2 Indoor Radio Propagation Modeling

The power of a radio signal travelling between two nodes contains information related to the distance or range between them. This parameter is commonly referred to as Received Signal Strength (RSS). There are basically two classes of techniques that are used for determining location using RSS. The first class of location methods involves matching the real-time signal strength measurements with a known surveyed database. The advantage of this database estimation method is that it is based on actual path loss at points near the target location, which accounts for shadowing and multipath [Bensky 2008]. Several ways can be adopted to compare the real-time measurements with the database: one commonly used method is to find minimum

Euclidian distance, also known as nearest neighbor method or fingerprinting. The other type of approach is to use statistical method optimized in Bayesian sense [Gezici 2008].

Suppose each of the surveyed positions can form a vector Vn consisting of the reliable access points from the database. The user's online AP signal strength forms another vector Vu .

Therefore, these two vectors can be compared by calculating their Euclidean distance as

$$Dn = |Vn - Vu| = \sqrt{\sum_{i=1}^K (Vn_i - Vu_i)^2} \quad (2.3)$$

Where:

Vn is the signal strength vector at surveyed positions

Vu is the signal strength vector at the user positions

K is the number of effective access points,

n is the number of surveyed positions in the database with the known coordinates.

Technically this method renders best performance but it is not preferable in practical application because on-site surveys of large indoor areas are required to obtain and retain good resolution and accuracy. Therefore, this solution is not economical and scalable.

The second class of techniques estimates location by estimating the distances between the mobile terminal and a number of fixed stations with known coordinates. Distances can be derived from formulas of wireless propagations models as discussed in the next section. Using this approach, the positions can be derived without any on-site survey. Therefore, it is more economical and scalable and will be utilized for the focus of this research.

This section will look more closely at the modeling of residuals that reflect the fluctuation of the actual received signal. Practically speaking, many factors impact the RSS, including how the transmitted signal reaches the receiver. This first factor is known as multipath, which causes

distortion in received signal envelope and phase. The second factor is the physical obstruction of the signal due to people, closed doors and walls etc., which changes the RSS. The third factor is caused by the variations in the transmission power of the access points and the receiver front-end, leading to different RSS. There are some other factors such as receiver antenna's orientation, radio interference etc. that impact RSS.

As mentioned above, the motivation of the wireless channel modeling is to build a relationship between the RSS and the distance to access points. In this section, we will examine the wireless path loss behavior in multiple indoor environments before empirically deriving a model.

Accurate positioning from Wi-Fi signal strength readings is a very difficult task, due to the fact that radio signals are noisy, fluctuate constantly, and have high variance. As such, an accurate statistical evaluation of the location errors is important which allows for appropriate weighting in the Kalman filter integration with other systems.

From the perspective of radio wave propagation, there are two models predicting the RSS at a given distance from the transmitter [Rappaport 2002]. The large-scale propagation model characterizes signal strength over large transmitter-receiver separation distances. On the other hand, propagation models that characterize the rapid fluctuations of the received signal strength over very short travel distances or short time durations are called small-scale models. The measurement error caused by small-scale model fading is greatly mitigated by performing time-averaging on all received signals. Hence, the main task here is to find large-scale model.

The large-scale path-loss can be obtained as [Bensky 2008]:

$$PL(d) = 20\log\left(\frac{4\pi d_0}{\lambda}\right) + 10n\log\left(\frac{d}{d_0}\right) + s \text{ (for } d > d_0) \quad (2.4)$$

Where:

- d is the distance between the access point and the user terminal
- λ is the radio wave length
- d_0 is the distance between the access point and a reference point
- n is the exponential path loss factor
- s is the lognormal distributed variation of the received signal accounting for shadowing factors.

Since s is a Gaussian distributed and has a zero mean, it can be averaged out resulting in further simplification of the radio loss modeling. Consequently, Equation (2.4) reduces to a curve fitting between path loss and distance given in Equation (2.5) as shown below:

$$PL(d) = A + B \log(d) \quad (2.5)$$

2.3.3 Received Signal Fluctuation

This section will look more closely at the modeling of residuals that reflect the fluctuation of the actual received signal. Practically speaking, many factors impact the RSS, including how the transmitted signal reaches the receiver. This first factor is known as multipath, which causes distortion in received signal envelope and phase. The second factor is the physical obstruction of the signal due to people, closed doors and walls etc., which changes the RSS. The third factor is caused by the variations in the transmission power of the access points and the receiver front-end, leading to different RSS. There are some other factors such as receiver antenna's orientation, radio interference etc. that impact RSS.

As these factors are not accounted for in the channel modeling provided in Equation (2.5), the model presented is not very accurate. We can estimate the deviation from the actual channel model using statistical analysis on stationary point with line-of-sight (LOS) as given in Figure 2-

3. From wireless communication theory, the small-scale fading envelope distribution is Ricean distribution in Equation (2.6) as the RSS has a mean SNR of 41.3dB which is a dominant signal component with a standard deviation of 2.4 dB. In Equation (2.6), parameter A is the amplitude of the direct line-of-sight signal and σ is the standard deviation of Rician distribution. $I_0(\cdot)$ is the modified Bessel function of the first kind with order zero.

$$p(r) = \begin{cases} \frac{r}{\sigma^2} e^{-\left(\frac{r^2+A^2}{2\sigma^2}\right)} I_0\left(\frac{Ar}{\sigma^2}\right) & (0 \leq r \leq \infty) \\ 0 & (r < 0) \end{cases} \quad (2.6)$$

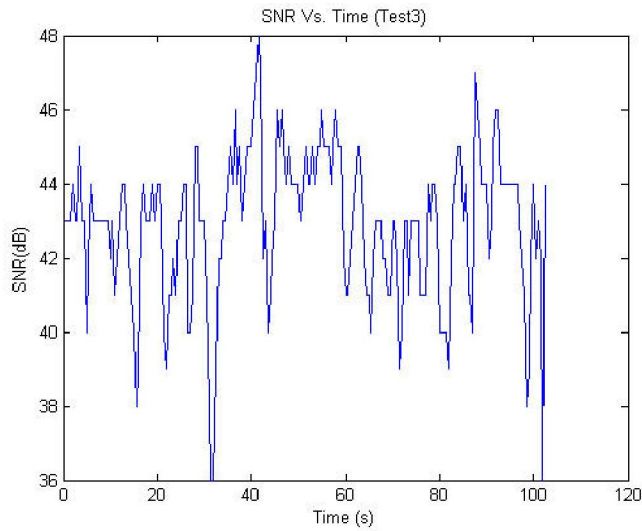


Figure 2-3 SNR fluctuations with the time (LOS case)

In the absence of a strong received component, such as in non-line-of-sight (NLOS) cases, the Rayleigh distribution is widely used to describe multipath fading. The Rayleigh distribution has a probability density function given by:

$$p(r) = \begin{cases} \frac{r}{\sigma^2} e^{-\left(\frac{r^2}{2\sigma^2}\right)} & (0 \leq r \leq \infty) \\ 0 & (r < 0) \end{cases} \quad (2.7)$$

Where:

r is the root mean square (RMS) value of the received signal voltage

σ is the standard deviation of the time-average of the received signal power

Figure 2-4 gives the SNR distributions and histograms from two stationary points. As can be seen, the LOS and NLOS cases agree nicely with the theoretical distributions in Equations (2.6) and (2.7). When the average received signal strength is above a certain threshold, the above models have a high confidence level. Therefore, setting a threshold to ensure positioning will only be performed for received signals with high signal to noise ratios. This will be discussed in more detail in Sector 5.5.

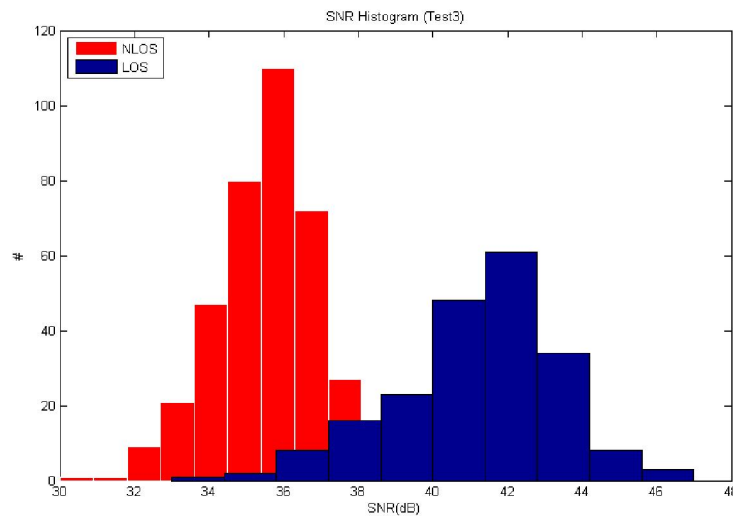


Figure 2-4 SNR distribution histogram (LOS and NLOS case)

2.3.4 Wi-Fi Positioning Algorithm

This section will introduce how to estimate the Wi-Fi receiver position in the case of received signal strength from multiple access points. One effective way is called Weighted Centroid

Localization (WCL), which introduces variable weights ω_{ij} for each access point position (x_j, y_j, z_j) to ensure an improved position estimate [Schuhmann, 2008]. The new approximation (x_i', y_i', z_i') is calculated from Equation (2.8).

$$(x_i', y_i', z_i') = \frac{\sum_{j=1}^n \omega_{ij} \cdot (x_j, y_j, z_j)}{\sum_{i=1}^n \omega_{ij}} \quad (2.8)$$

These weights are adapted dynamically depending on the distance between the access point and the receiver. According to free radio loss Equation (2.4), the detected signal strength decreases quadratically with the distance. Consequently, we can assign the weight to be proportional to the received signal power P_{rx} , where it equals to the transmission power minus the path loss in dB.

$$P_{rx} = P_{tx} - PL \quad (2.9)$$

As mentioned earlier, indoor wireless modeling is inaccurate due to attenuation of the signal and hence, an SNR threshold of 49 dB is chosen for signal selection. When the SNR is above this threshold, it suggests the user is close to the access point and the impact of signal attenuation is relatively small. For SNR values less than the threshold, the signal is not used for positioning to avoid adverse impact on the result. Empirically, an SNR of 49 dB is a good threshold that roughly corresponds to a range of 10-12 m between the user and access point. WCL method is used to estimate user location when less than three access points are available.

Similar to GPS, trilateration is used for the position fix when three or more access points are available, as illustrated in Figure 2-5. As each RSS can be converted to pseudo range r_i , the observation equation for the i th access point at (X_i, Y_i) is given as follows:

$$(X - X_i)^2 + (Y - Y_i)^2 + (Z - Z_i)^2 = r_i + v_i \quad (2.10)$$

Where v_i is the measurement noise.

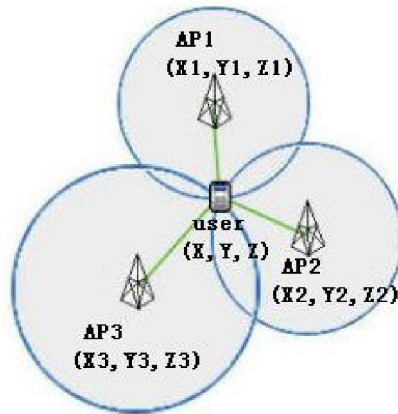


Figure 2-5 Trilateration of Wi-Fi positioning

The final position is computed using least squares as given in Equation (2.11).

$$\hat{x} = (H^T R^{-1} H)^{-1} H^T R^{-1} z \quad (2.11)$$

Where H is design matrix from Equation (2.3), z is the observation vector and R is the observation covariance matrix.

2.4 Altitude Integration

GPS is usually less accurate vertically than horizontally and inertial navigation systems are unstable in the vertical axis if unaided. Barometric altimeters provide a measure of altitude based on the measure of static atmospheric pressure. This pressure measurement is directly related to the height above mean sea level. Thus, a vertical axis positioning solution can be deployed using inexpensive MEMS barometers in the market. One challenge is that the pressure readings vary with weather conditions thus must be corrected on a regular basis with a reference barometric altimeter at a known height and nearby location for long duration applications.

Therefore, barometer readings offsets need to be calibrated to improve vertical positioning accuracy.

This sector gives introduction on how height is derived from barometer measurement and Chapter 5.3 will introduce how to calibrate barometer offset and estimate height properly when GPS height is available. Better vertical positioning solutions enable applications such as identifying which floor a user is on inside of a large building.

2.4.1 Height Definition

There are usually three heights: orthometric height (H), geodetic height (h), and geoid height (N), as shown in the Figure 2-6 below.

Orthometric Height

A geoid is an equi-potential surface that coincides with the mean ocean surface of the Earth. The geoid does not only represent the actual physical shape of the Earth, but it is also a reference surface for elevations. An elevation above the geoid is often referred to as an orthometric height, elevation, or mean sea level (MSL), denoted as H . It is usually what a pressure sensor measures.

Geodetic Height

The geodetic (or ellipsoid height), h , is the height with respect to WGS84 reference ellipsoid, i.e., the distance between a point on the Earth's surface and the WGS84 ellipsoidal surface, as measured along the normal (perpendicular) to the ellipsoid at the point and taken positive upward from the ellipsoid. It is usually what a GPS receiver measures.

Geoid Height

The height of the geoid with respect to the ellipsoid is denoted N , also known as geoid height, or undulation height. The current WGS84 geoid model is also known as the Earth Gravity Model 1996 [GCM 1996] defining the N , and gravitational potential as a spherical harmonic function of geodetic latitude and longitude [Groves 2008].

The orthometric height H is related to the geodetic height h by:

$$h=H+N \quad (2.12)$$

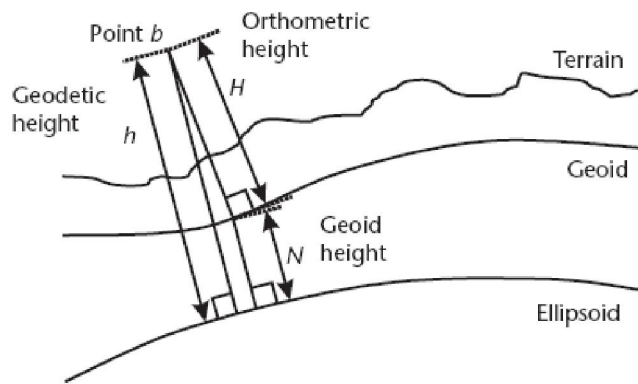


Figure 2-6 Illustration of three height definitions

2.4.2 Conversion from Pressure to Height

Barometer sensors usually provide pressure and temperature measurements which can be converted to the orthometric height H . According to 1976 US Standard Atmosphere, H is a function of pressure P and temperature T as given in Equation (2.13).

$$H = T / (-dT / dH) \cdot [1 - (P / P_0)^{(-dT/dH) \cdot R/g}] \quad (2.13)$$

Where:

T is local temperature, unit in Kelvin; Kelvin=273+Celcius Degree.

dT / dH is temperature gradient, usually assumed a constant value of -6.5 Kelvin/km.

P is pressure sensed by barometer, unit in mbar.

P_0 is equal to 1013.25 mbar, standard atmospheric pressure.

R is equal to 287.052 m²/s²/kelvin, gas constant.

g is equal to 9.8 m/s², gravity.

2.5 Other Aiding Sensors

Other aiding sources may come from feature-matching techniques that determine position by comparing and matching the gathered position information with a database. Maps play an important role in providing a geolocation context for positioning, location, and navigation. Map aiding, as its name suggests, provides information extracted from maps to improve the user experience of path-finding, pinpoint positioning, etc. Among various capabilities from the aiding, Map matching is a method for projecting the estimated position from the navigation system to a digital vector map. The general purpose of MM algorithms is to identify the correct road segment on which a moving object is traveling and to determine the position on that segment. Therefore, MM algorithms improve positioning accuracy.

Lastly, new MEMS sensor types are emerging and the underlying technology is still evolving rapidly. Among them, non-intrusive infrared (IR) proximity sensors for proximity sensing are very popular. These can detect bodies in the vicinity of the device and are perfectly used on smartphones. Active light sensors can provide the ambient light intensity within a certain measurement distance. The combination of air pressure, humidity, temperature sensors, ultraviolet sensor and gas sensor provides a finer granularity of the local environment and location awareness, offering environment context useful for navigation.

2.6 Choice of Suitable Technology

The positioning techniques for personal navigation systems discussed in this chapter all have advantages and drawbacks; there is no single solution that is versatile enough to provide accurate location data in a full range of operational conditions, and the final choice is largely driven by the application. Therefore, integration of multiple hybrid sensors and systems is the obvious solution for future applications.

Table 2.2 summarizes the most popular positioning technologies and their characteristics for personal navigation. The purpose here is to find the most suitable alternative technologies for personal navigation in GNSS-denied places [Samama 2008], such as deep indoors or in the urban canyons where the received satellite signal strength is less than -160dBm.

Table 2-2 Comparison of personal navigation technology

Techniques/ Sensors	Typical Performance	Characteristics
GNSS	~10m (Single GPS) ~1-3m (DGPS) ~ 1 cm (Carrier phase DGPS)	Line-of-sight system Result in global reference system
Cellphone	50-500m Wide coverage range	Low accuracy for cell-in approach TOA approach needs carrier's external info
WLAN	3-20m (signal strength based) 1-5m (fingerprinting based)	Good for indoor positioning locally Requires infrastructure coordinates
Bluetooth /RFID	0.1-1 meter level accuracy 5-50m coverage range	Better signal quality indoors Need dedicated system setup
INS	1%-5% error of distance travel <10° attitude error	Time dependent Relative positioning
Magnetometer	~1-10° attitude error without disturbances	Time invariant Subject to external disturbances
Barometer	~1m altitude resolution	Good relative accuracy Subject to local disturbances
Camera /Map matching	~1-5m	Image processing, Build topological matching, assist turn detection, Need known GIS database

As listed in Table 2-2, the candidates include ground-based RF systems, such as Bluetooth, RFID and pseudolites; mainstream wireless communication systems, such as cellular phone and Wi-Fi; vision aiding systems, such as cameras and map matching [Attia 2013]; and dead reckoning sensors, such as magnetometers, gyroscopes, accelerometers, and barometers [Parviainen 2008]. Considering the availabilities, accuracy, and cost factors for mass production, the above candidate technologies face some limitations for practical implementations.

Laser/camera systems are relatively expensive and too power hungry to apply in mobile devices; Bluetooth/RFID/map matching entails significant infrastructure deployment and maintenance; cellular infrastructure is widely available, however lacks the accuracy desired for most applications.

Finally, an integrated Wi-Fi, GNSS, and MEMS solution stands out as a good combination for this application. Dead reckoning systems, including accelerometers, gyroscopes, and magnetometers are beginning to receive wide acceptance on consumer electronics with the continuous cost reduction of their base components. On the other hand, Wi-Fi enabled devices are pervasive in most mobile devices as well. Wi-Fi hotspots have already covered many densely populated urban areas such as airports, campuses, and shopping malls, which means a low operating cost in comparison to other technologies. Technically speaking, MEMS sensors and Wi-Fi technologies are complementary. Dead reckoning sensors can determine a person's orientation, distance traveled, and height while the sensors are self-contained and render good relative positions in short periods of time. In contrast, Wi-Fi positioning can provide absolute positions over the long term as an update for dead reckoning when GPS signals are blocked. In addition, magnetometers and barometer are considered in this thesis as redundant measurements to improve the heading and height estimation.

For consumer mobile devices such as smartphones and tablets, GNSS, Wi-Fi, and motion sensors stand out as a good combination. These three technologies are complementary to each other:

- GNSS provides absolute positions globally and gives good accuracy outdoors.
- Motion sensors enables dead reckoning mechanism; it determines a person's orientation, distance traveled and height change which render good relative positions in short periods of time.
- Wi-Fi is one of the most popular local wireless systems that provide absolute position updates indoors at any time

Integrating data from each of these systems results in a hybrid solution with the combined strength of each module. Such a hybrid positioning system can be easily implemented on mobile devices using a Kalman filter fusion which will be discussed in details throughout the rest of this thesis.

Chapter Three: **MODELING AND CALIBRATION OF MEMS SENSORS**

Key performance metrics of MEMS sensors such as resolution, sensitivity, biases, and power consumption have improved by an order of magnitude during the past decade [El-Sheimy 2007]. This is due to the development of IC processes, new materials, MEMS structural design, integrated circuitry design, and advanced digital signal processing. As a result, inexpensive MEMS sensors have reached automotive-grade standards and will likely continue advancing to penetrate standards for low-end tactical-grade uses in the near future.

To meet the requirements of motion tracking introduced in Chapter 2, a ten degrees-of-freedom sensor fusion of three-axis accelerometers, three-axis gyroscopes, three-axis magnetometers, and a barometer are selected to measure three dimensional rotation, acceleration, and altitude. As measurement errors inherently exist in sensor output, a thorough understanding of MEMS sensor design and behavior are essential for navigation system design. Among the above MEMS sensors, gyroscopes and magnetometers performance are particularly relevant to overall system performance. The weaknesses of low-cost MEMS gyroscopes lie in critical performance parameters degradations such as noise, bias instability and environment sensitivity, which dominant to overall sensors fusion performance. On the hand, magnetometers are useful to give absolute heading correction but are vulnerable to environment disturbance.

Therefore, this chapter will focus on these two sensors. Chapter 3.1 gives an overview of MEMS gyro operation mechanism and then extracts some key parameters and tradeoffs in gyro design that are related to error analysis. Chapter 3.2 presents gyroscope error modeling and noise analysis which will be used in the navigation filter later. Chapter 3.3 covers error compensation

and calibration method for gyroscope and magnetometer. MEMS sensors fabrication and operation theory and technologies are given in Appendix A and B respectively.

3.1 Gyroscope scope Design Analysis

3.1.1 Operation Principle

Almost all modern consumer MEMS gyroscopes are of a vibratory type, based on sensing Coriolis acceleration, which is acceleration produced due to the changing direction in space of the velocity of a moving system. The operation of vibratory gyroscopes is governed by the equation of relative motion, the particle velocity $V^i = \dot{r}^i$ as viewed in the inertial frame-i is related to the velocity $V^r = \dot{r}^r$ in the rotating frame-r by:

$$\dot{r}^i = \dot{r}^r + \Omega \times r^r \quad (3.1)$$

Where:

r^r is the time-dependent position vector in the rotating frame

$\Omega = (\Omega_x, \Omega_y, \Omega_z)^t$ is the rotation vector with respect to the rotating frame.

Applying this time derivative operation again, we can get the acceleration of the particle in the inertial frame as:

$$\ddot{r}^i = \ddot{r}^r + 2\Omega \times \dot{r}^r + \Omega \times (\Omega \times r^r) + \dot{\Omega} \times r^r \quad (3.2)$$

As Newton's Second Law only applies in the inertial frame, $F^i = m\ddot{r}^i$, hence the apparent acceleration in the rotating frame, \ddot{r}^r , yields the following relationship in Equation (3.3).

$$m\ddot{r}^r = F^l - 2m\Omega \times \dot{r}^r - m\Omega \times (\Omega \times r^r) - m\dot{\Omega} \times r^r \quad (3.3)$$

Where:

$-2m\Omega \times \dot{r}^r$ is known as Coriolis acceleration force;

$-m\Omega \times (\Omega \times r^r)$ is the centrifugal force. Usually when the angular rate is much smaller than proof mass resonant frequency, this term can be neglected;

$-m\dot{\Omega} \times r^r$ is due to a non-constant rotation rate of the rotating frame, it can be neglected as well when the sensors have relatively small output bandwidth.

With the knowledge of \ddot{r}^r and neglecting the last two terms in Equation (3.3), the following mechanical equation of proof mass motion can be derived [Younis 2011].

$$M\ddot{r}^r + D\dot{r}^r + Kr^r = F^l - 2m\Omega \times \dot{r}^r \quad (3.4)$$

Where M, D and K are positive definite mass, damping and stiffness matrices respectively.

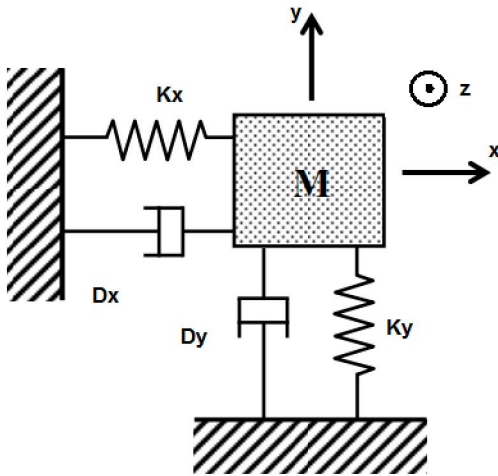


Figure 3-1 A simplified model for Z-axis gyroscope.

Based on the above classical mechanics principles, a single axis vibrating gyroscope are further analyzed. As illustrated in Figure 3-1, the gyroscope frame rotates about the z axis, orthogonal to the x-y plane. A proof mass M is attached to the rotating sensor frame by elastic suspensions. Two degrees of mechanical freedom are required, one for motion driving and one for motion sensing.

The proof mass is first put into drive mode of vibration along the x-axis, with a controlled-amplitude of oscillation. Once in motion, the proof-mass is sensitive to angular rotation about the z-axis perpendicular to the plane. This rotation thus induces a vibratory displacement from the Coriolis force along the y-axis, known as sense mode to measure the angular rate. Referring to Equation (4), the motion equations in x-y plane become:

$$m_x \ddot{x}^r + d_x \dot{x}^r + k_x x^r = F_x^i + 2m\Omega_z \dot{y}^r \quad (3.5)$$

$$m_y \ddot{y}^r + d_y \dot{y}^r + k_y y^r = F_y^i - 2m\Omega_z \dot{x}^r \quad (3.6)$$

Assume the solution to Equation (3.5), which is the x-displacement along the drive axis, is given by a sinusoidal form as

$$x = -X_d \sin(\omega_d t) \quad (3.7)$$

And there is also no external excitation to the sense mode, i.e. $F_y^i = 0$. The resulting system has one degree of freedom along the sensing y-axis, governed by

$$m_y \ddot{y}^r + d_y \dot{y}^r + k_y y^r = 2m\Omega_z X_d \omega_d \cos(\omega_d t) \quad (3.8)$$

Equation (8) is a typical second-order non-homogeneous linear different equation [Sharma 2008]. By introducing natural frequency ω_s and quality factor Q_s of the sense mode, Equation (3.8) becomes

$$\ddot{y}^r + \frac{w_s}{Q_s} \dot{y}^r + w_s^2 y^r = 2\Omega_z X_0 w_d \cos(w_d t) \quad (3.9)$$

Where:

$$w_s = \sqrt{k_y/m_y}$$

$$Q_s = w_s m_y / d_y$$

A convenient way to express this solution is through a form of an amplitude Y and a phase θ as:

$$y_s(t) = Y \cos(w_s t - \theta) \quad (3.10)$$

Where:

$$Y = \frac{2w_s X_d \Omega_z}{\sqrt{(w_s^2 - w_d^2)^2 + \left(\frac{w_s w_d}{Q_s}\right)^2}} \quad (3.11)$$

$$\theta = \tan^{-1}\left(\frac{w_s w_d}{Q_s (w_s^2 - w_d^2)}\right) \quad (3.12)$$

From Equation (3.11), we can see that the sensing amplitude output is proportional to the input angular rate Ω_z . If the sense and drive resonant frequency is equal (i.e. $w_s = w_d$), the output signal will be amplified by quality factor Q_s of the sense mode, resulting in high gain.

Figure 3-2 shows the block diagram of a typical MEMS vibratory gyroscope. It consists of a drive actuator represented by the equivalent drive-mode dynamics transfer function. The drive amplitude X_0 must be maintained very accurately since any variation will contribute directly to the sense output. Therefore, the drive loop is controlled by an automatic gain control (AGC) loop. In the sense branch, the Coriolis term is twice the product of the input angular rate and the velocity of the drive axis oscillator in quadrature which produces a modulated signal. The spring-

mass sensing MEMS is equivalent to a sense-mode dynamics transfer function. Consequently, the gyroscope output needs to be demodulated by multiplying the in-phase drive signal coming from a phase-locked loop (PLL). The multiplication then passes through a low-pass filter (LPF). Lastly, the gain was adjusted to compensate for temperature and any other scale factors before output rate is generated.

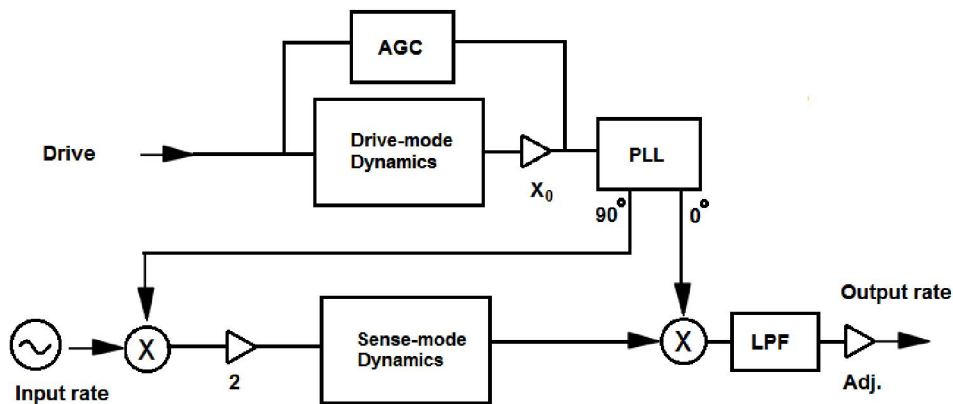


Figure 3-2 Block diagram of vibratory gyroscope

3.1.2 Gyroscope Parameters Design Analysis

3.1.2.1 Resolution and Noise Performance

The resolution of a sensor represents the smallest increment of the input measurement that the sensor can be detected. For modern sensors with digital outputs, their resolution can determine their sensitivity. In these cases, the Least Significant Bit (LSB) in the ADC output changes with small variations of the input signal. The standard resolution from the gyroscopes' outputs is mainly limited by the sensor's noise density and the bandwidth parameter. The system noise density, also referred to as Total Noise Equivalent Rotation (TNE Ω), consists of two

uncorrelated components: the Mechanical Noise Equivalent Rotation (MNEΩ) and the Electrical Noise Equivalent Rotation (ENEΩ) [Sharma 2008]. These components are measured in (°/s).

$$TNE\Omega = \sqrt{MNE\Omega^2 + ENE\Omega^2} \quad (3.13)$$

MNEΩ represents thermo-mechanical noise (or Brownian noise) noise floor of the mechanical sensor element and is given by Equation (3.14). The noise is due to Brownian motion of the gas molecules surrounding the proof mass and the Brownian motion of the proof mass suspensions or anchors.

$$MNE\Omega = \frac{1}{2A_{dr}} \sqrt{\frac{4k_B T}{\omega_0 M Q_{eff}}} \sqrt{BW} \quad (3.14)$$

Where:

k_B is the Boltzmann constant;

T is the absolute temperature in K;

A_{dr} is the amplitude of proof-mass vibration along the drive axis ;

M is the effective mass;

ω_0 is the sensor resonant frequency;

Q_{eff} is the effective mechanical quality factor;

BW is the measurement bandwidth.

The electronic noise floor of the gyroscope is related to the design sensor readout electronics, it is directly proportional to the total input referred current noise i_n , and inversely proportional to the electromechanical sensitivity S_z as shown below [Ayazi 2011].

$$\text{ENE}\Omega = \frac{i_n}{S_z} \sqrt{\text{BW}} \quad (3.15)$$

For a mode-matched gyroscope ($w_s = w_d$), a fixed DC potential V_p has been maintained across the sense gap d_{so} , then in response to the input rotation Ω_z , Coriolis-induced displacement of the proof-mass changes the sense rest capacitance C_{so} generating a motional current I_{out} . Thus, the electromechanical S_z is given by:

$$S_z = \frac{I_{out}}{\Omega_z} = \frac{2V_p C_{so} Q_{eff}}{d_{so}} A_{dr} \quad (3.16)$$

Substituting (16) into (15), $\text{ENE}\Omega$ yields:

$$\text{ENE}\Omega = \frac{d_{so}}{2V_p C_{so} Q_{eff} A_{dr}} i_n \sqrt{\text{BW}} \quad (3.17)$$

Since $\text{TNE}\Omega$ above assumes white noise to be the main contributor, this value is equivalent to the RMS of rotation rate noise (g_n). If the measurement bandwidth BW is known, then the noise density parameter equals the angular random walk in ($^\circ/\text{s}/\sqrt{\text{Hz}}$).

$$\text{ARW} = \frac{\text{TNE}\Omega}{\sqrt{\text{BW}}} \quad (3.18)$$

The above derivation shows an intrinsic limitation of the MEMS sensors set by its sensitivity and noise performance. From Equation (3.11), sensitivity of the gyroscope sensor can be enhanced by lowering the resonant frequency ω_0 ; however, this adversely increases the $\text{MNE}\Omega$.

Equations (3.17) clearly showed the trade-off between noise performance and measurement bandwidth in inertial sensors. Gyroscope bandwidth determines the frequency range of the angular velocity signal that can be measured. A higher bandwidth enables measurement of faster motions at the expense of a higher noise level or lower resolution. The bandwidth is set by the electronics and is usually on the order of 100 Hz.

Furthermore, there are some practical considerations in mode matching frequencies between drive and sense modes. Maximum resolution is obtained when the driven mode is the same as the sensing mode at the resonant frequency, causing the sensitivity to be amplified by the mechanical quality factor Q of the sense structure. However, this involves extreme control of device dimensions and may lead to large bias drift problems if environmental factors, such as temperature, vary and cause a mismatch between drive and sense frequencies. Therefore some mechanical structures deliberately configure frequency to be slightly different in sense and drive modes.

Finally, it should be noted that the fundamental limiting noise component of the mechanical structure is due to the Brownian motion of the sense vibration mode [Yazdi 1998]. However, with non-resonant sensing ($\omega_s \neq \omega_d$), the Brownian noise is attenuated by the system transfer function, thus resolution may be limited by the noise of readout, signal-processing, and control electronics [Nguyen 2012]. High-performance MEMS gyroscopes require low noise, parasitic-insensitive interface circuits capable of resolving atto-farad changes in capacitance.

3.1.2.2 Bias

The bias of a gyroscope is its apparent output in no-rotation mode. It is also called Zero-Rate Output (ZRO). ZRO is primarily determined by mechanical sources such as geometrical

imbalances in the vibrating mechanical drive/sense structures and off-axis motion of the proof mass, both caused by the fabrication imperfections. In addition, electrical error sources such as cross-coupling between driving and sensing electrodes, phase setting imperfection for demodulation, and the electronic offset will contribute the bias error [Kempe 2011]. Note although random gyroscope noise and drift are additive error sources like a bias, it is important to differentiate this systematic bias with the random changes of output.

3.1.2.3 Environment Sensitivity

MEMS sensors exhibit some environmental dependencies. For example, angular velocity output of the MEMS gyroscope is correlated to temperature change. It is caused by several factors including changes in the Young's modulus of silicon (100 ppm/deg) and the damping coefficient. Both of these variables are sensitive to temperature. Gyroscope sensitivity is also affected by circuit temperature coefficients. All low cost MEMS gyroscopes exhibit some ZRO and scale factor variation over temperature change, specified as a % change of scale factor per °C. Therefore, it is important for users to calibrate and compensate them when the device experiences large variations in temperature.

Another type of environmental factor is vibration sensitivity (g-sensitivity). In practice, all gyroscopes have some sensitivity to acceleration due to the asymmetry of their mechanical designs and/or zeroing of the null bias. Vibration can be modeled as noise in the gyroscope output, possibly resulting in inaccuracies that are too large to accommodate. Sensors signal processing, such as filtering, can help minimize vibration issues.

Table 3-1 below summarizes the most critical system parameters for consumer-grade gyroscopes. The table shows many design parameters are impacting each other and good trade-

offs need to be made: the resolution and sensitivities of gyroscopes can be improved by maximizing effective quality factor Q_{eff} , however large Q_{eff} leads to excessive sensitivity to the environment change; noise performance comes at the trade-off of the gyroscope bandwidth; relatively high power consumption is a concern in vibratory gyroscopes, but large driving current and bias voltage can reduce the electrical noise; also, large proof mass size can lower the thermo-mechanical noise floor, the penalty is the increase of the die size.

Table 3-1 Key parameters of consumer-grade MEMS gyroscopes

Parameter	Explanation	Associated design parameters
Rate resolution (ARW)	Smallest detectable input measurement; An indicator of short-term noise level.	White noise from mechanical element and electrical readout circuitry, improve by increasing quality factor Q_{eff} .
Bandwidth (BW)	Frequency range of the angular velocity signal that can be measured linearly.	Inversely proportional to noise level.
ZRO Bias (ZRO)	Apparent output in zero input rate.	Large proof mass, better MEMS matching and circuitry compensation will improve.
Environment sensitivity of SF	Scale factor variation over temperature, acceleration and vibration change.	Improve by decreasing quality factor Q_{eff} .
Power	Energy consumption related to current and power voltage.	Inversely proportional to noise level.
Package Size	Three dimensional IC size	Limited by mechanical structure and MEMS/CMOS integration technology

High performance navigation systems entail accurate sensors modeling of deterministic and stochastic errors [17]. For deterministic error analysis, it requires careful analysis of the relationship between the quantities represented in the system reference frames to determine the proper system dynamic and measurement models. For the stochastic error analysis, there are some issues to be considered: First, the system and measurement noise need to be evaluated, which can be represented by an error covariance matrix. Second, the sensors performance needs to be addressed by state augmentation, which can be modeled based on sensor calibration and

Allan variance tests. Finally, to make the system more robust, some on-line calibration methods are preferred so the system can be adaptive in varying environments. In most sensors fusion applications, a gyroscope's performance is the most critical, thus its sensor characteristics dominate the overall system performance. Therefore, in the subsequent section, gyroscope performance analysis and modeling will be analyzed as an example.

3.2 Gyro Error Modeling

Based on the understanding of the MEMS mechanisms presented in the previous section, in this section sensor modeling takes into account all the possible error sources that are relevant to navigation. Inertial navigation system design depends on accurate knowledge of sensor behavior. Any number of the noise and imperfection discussed above will be present in the data as error. Thus, a unified mathematical modeling of MEMS gyroscopes is essential for system-level algorithm design and performance prediction. Since low-cost MEMS inertial sensors are restricted by real-world manufacturing tolerances, these models can be applied to calibrate and compensate for system errors.

Figure 3-3 gives a classification of MEMS sensor error sources. All errors can be broken down into two main categories: deterministic and stochastic errors. The deterministic components, such as ZRO bias, nonlinearity scale factor, and cross-axis misalignment are dependent on manufacturing tolerances or other external factors that are repeatable, thus they can be calibrated and compensated for by the product vendor's or the user's initial calibration. Stochastic component are errors that vary randomly after each turn-on. They include bias drift attributable to angle random walk, bias instability, environmentally sensitive Markov noise, output

quantization noise, and any other electronic or mechanical noise lumped together as an additive zero-mean white noise. Stochastic models are used to represent the remaining errors after the deterministic parts have been removed.

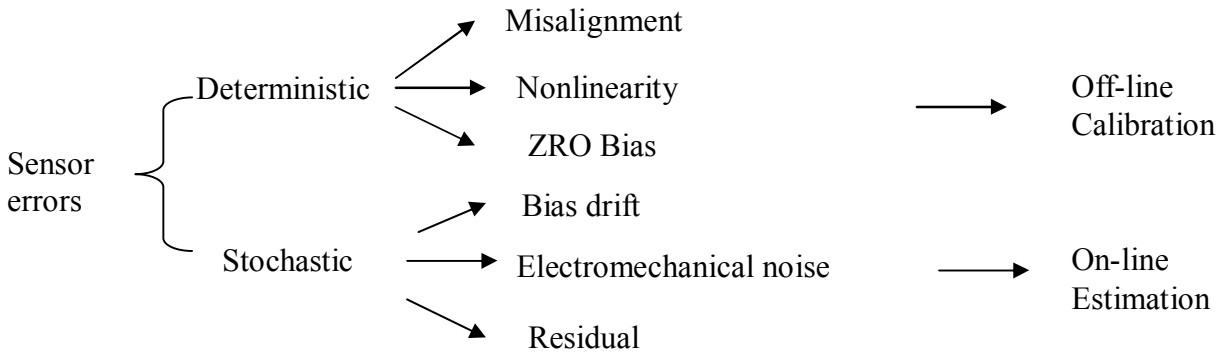


Figure 3-3 MEMS sensor error sources

In spite of individual differences on MEMS design and manufacturing, a general-purpose parametric model can be developed to take into account the main error terms discussed above. A unified model between the true gyroscope signal $X_t(t)$ and measurement $X_m(t)$ can be constructed as:

$$X_m(t) = SF(t) \cdot X_t(t) + B_0 + B_{corr}(t) + B_w(t) \quad (3.19)$$

Where:

B_0 is the deterministic gyroscope bias;

$SF(t)$ and $B_{corr}(t)$ are environmentally sensitive scale factors and biases that sometimes exhibit exponentially correlated characteristics as Markov noise;

$B_w(t)$ is the residual noise predominantly band-limited ARW white noise in most MEMS gyroscopes.

MEMS sensor calibration is essential to ensure navigation performance. Based on the model above, calibration and compensation can be estimated at different stages. Initial offline calibration can be performed after the gyroscope is assembled, where calibration coefficients, such as deterministic bias and scale factor, are derived from calibration tests over the operating temperature range. The gyroscope bias calibration procedure can be divided into two categories:

- **Initial offline ZRO and SF calibration:** In a temperature stable environment, the gyroscopes' biases and scale factors are calibrated offline as the initial default value. To do this, simply bring the gyroscope up to the intended operating temperature and measure the null rotation output B_0 . To determine the scale factor (SF), applying a rotation table the angular rate is set to a known value X_t . Because most gyroscopes have very little nonlinearity, it is adequate to measure the output X_m at one rotational rate, preferably near full scale. Then the scale factor can then be calculated by:

$$SF = (X_m - B_0) / X_t$$

- **Online bias drift calibration:** this method is preferred because, unlike initial offline sensor calibration, drifting sensor errors are not accounted for. The bias of gyroscopes can be estimated by detecting the zero rate offset at the right time. The gyroscope bias drift online calibration method is straightforward: continuously monitor if the device is in a stationary status; if so, average the output of the stationary time as a zero-rate offset. Therefore, stationary feature extraction is the key in this design.

Since accelerometers are available in most gyroscope platforms such as in an IMU, they are selected as always on, stationary monitoring sensors for their low power consumption. Firstly, a recursive moving window is used to monitor sensor data. This window size is set as 1 second. The standard derivation of the accelerometer output within the window is calculated recursively in Equation (3.20)-(3.24) as follows.

$$x_n = \sqrt{a_x^2 + a_y^2 + a_z^2} \quad (3.20)$$

$$\bar{x}_n = \frac{(n-1)\bar{x}_{n-1} + x_n}{n} \quad (3.21)$$

$$\text{var}_{n-1} = (n-2) \cdot s_{n-1}^2 \quad (3.22)$$

$$\text{var}_n = \text{var}_{n-1} + \frac{n}{n-1} (\bar{x}_n - x_n)^2 \quad (3.23)$$

$$s_n = \sqrt{\frac{\text{var}_n}{n-1}} \quad (3.24)$$

Where:

n is the total sample number within recursive window

x_n is the sensor input of the current epoch

\bar{x}_{n-1} is the mean value of window in last epoch

\bar{x}_n is the mean value of window in current epoch

s_{n-1} is the standard deviation of window in last epoch

s_n is the standard deviation of window in current epoch

A stationary mode is declared when the standard derivation of the accelerometer amplitude within the recursive window is less than a pre-defined threshold, as shown below:

If $s_{accel} < \text{Static_accel_threshold}$, then

Static.accel_flag=1;

Static.gyro_bias=mean(gyro_input).

Inspecting Equation (3.19), the residual noise $B_w(t)$ and time-correlated term $B_{corr}(t)$ require some statistical noise analysis, such as Allan Variance and time correlation analysis, in order to choose an appropriate model and parameters for the sensors stochastic behavior; the subsequent two sections will show more details. Additionally, real-time calibration can be performed during the operation, often by using a Kalman filter to estimate cumulative random gyroscope errors as error states. For example in an inertial navigation system (INS), gyroscope sensor models are used to recalibrate the INS continuously while GPS data is available. Furthermore, error models are critical to determine the optimal weighting in the integration of the GPS and INS navigation filter. Finally, it should be noted that the error state of INS sensors needs to be carefully selected considering the observability of error states in the system estimation.

3.3 Gyroscope Noise Analysis

Noise is one of the most important aspects for MEMS sensors performance. Gyroscope noise can be characterized by its noise density, in deg/s/ $\sqrt{\text{Hz}}$ RMS, and the square root of the power spectral density of the noise output. Consequently, total noise, defined as the random deviation from the ideal output, is equal to the product of the noise density and the square root of the noise bandwidth (BW):

$$\text{Total Noise} = \text{Noise Density} \times \sqrt{\text{BW}} \quad (3.25)$$

Allan Variance is a useful method to identify and quantify various random noise sources. It is a time-domain analysis representing the root mean square random-drift errors as a function of averaging times [El-Sheimy 2008]. Assume there are a total of N consecutive data points being constantly sampled at a rate fs, a group of n consecutive data points ($n < N/2$) can be formed as a cluster, associated with cluster time $T = n/fs$. Expressing in discrete-time form, the cluster average of the output rate between times t_k and t_{k+n} is then given by:

$$\bar{\Omega}_k(T) = \frac{\theta_{k+n} - \theta_k}{T} \quad (3.26)$$

Where $T = n/fs$ and θ_k is the cumulative sum of the sensor output $\Omega(i)$ as

$$\theta_k = \sum_{i=1}^k \Omega(i) \quad (3.27)$$

The Allan variance is then defined as variance of the difference between two adjacent clusters as

$$\sigma^2(T) = \frac{1}{2} \langle (\bar{\Omega}_{k+n} - \bar{\Omega}_k)^2 \rangle = \frac{1}{2T^2} \langle (\theta_{k+2n} - 2\theta_{k+n} + \theta_k)^2 \rangle \quad (3.28)$$

Where the contents enclosed in $\langle \dots \rangle$ represent the ensemble average.

Finally, the Allan variance calculation can be estimated as follows:

$$\sigma^2(T) = \frac{1}{2T^2(N-2n)} \sum_{k=1}^{N-2n} (\theta_{k+2n} - 2\theta_{k+n} + \theta_k)^2 \quad (3.29)$$

Allan variance analysis provides a convenient way of decomposing various types of random noises with different autocorrelation properties by observing the Allan variance plot in a

different cluster time, T . Since there is a unique relationship between the Allan variance $\sigma^2(T)$ and the power spectrum density (PSD) of the rotational signal $S_\Omega(f)$ shown in Equation (3.30), the Allan variance curve essentially contains the same information as the signal's PSD analysis in the frequency domain.

$$\sigma^2(T) = 4 \int_0^\infty S_\Omega(f) \frac{\sin^4(\pi f T)}{(\pi f T)^2} df \quad (3.30)$$

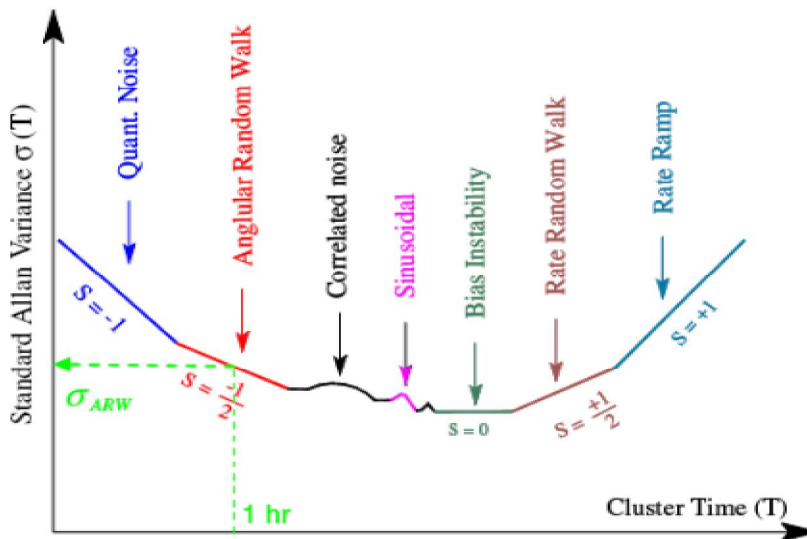


Figure 3-4 Allan variance analysis of gyroscope

Figure 3-4 above gives an illustrative sample of an Allan variance plot, which contains various noise sources at comparable magnitudes. By analyzing the characteristic regions on a log-log scale, the slope of the Allan variance plots different slopes can be clearly classified [IEEE 2008]. In most consumer-grade MEMS gyroscopes, there are a few terms dominantly more observable in the Figure 3-4.

(1) Angle Random Walk (ARW)

Given in $\text{deg}/\sqrt{\text{h}}$, ARW characterizes the standard deviation of the integrated output signal.

Since this type of noise is white noise directly added on the gyroscope output, when integrated, it is a random walk in angle. The associated noise PSD is represented by:

$$S_{\Omega}(f) = N^2 \quad (3.31)$$

Where N is the velocity random walk coefficient [IEEE 2008].

Substituting Equation (3.31) into Equation (3.30) and performing the integration yields:

$$\sigma^2(T) = \frac{N^2}{T} \quad (3.32)$$

Therefore, on a log-log scale, it has slope of -1/2.

(2) Exponentially correlated (Markov) noise

Some gyroscopes exhibit time correlation as well. This noise is characterized by an exponential decaying function with a finite correlation time T_c . The stochastic differential equation of the state variable x in time domain is described by:

$$\dot{x}(t) = -\frac{1}{T_c}x(t) + w(t) \quad (3.33)$$

Where T_c is the correlation time and $w(t)$ is the driving white noise with constant PSD q_w . The variance of time-correlated noise is:

$$\sigma_{T_c}^2 = \frac{T_c q_w}{2} \quad (3.34)$$

The noise PSD for such a process is:

$$S_{\Omega}(f) = \frac{q_w T_c^2}{1 + (2\pi f T_c)^2} \quad (3.35)$$

Similarly, substituting Equation (3.35) in Equation (3.30), the Allan variance is shown below

$$\sigma^2(T) = \frac{(q_c T_c)^2}{T} \left[1 - \frac{T_c}{2T} \left(3 - 4e^{-\frac{T}{T_c}} + e^{-\frac{2T}{T_c}} \right) \right] \quad (3.36)$$

Interestingly, for cluster time, T, much longer than the correlation time T_c, it is found that:

$$\sigma^2(T) \sim \frac{(q_c T_c)^2}{T}, \text{ for } T \gg T_c \quad (3.37)$$

The Allan variance for angular random walk where N = $q_c T_c$ is the angle random walk coefficient. On the other hand, for T much smaller than the correlation time, Equation (3.36) reduces to:

$$\sigma^2(T) \sim \frac{q_c^2}{3} T, \text{ for } T \ll T_c \quad (3.37)$$

This is the Allan variance for rate random walk, therefore the slope for Markov noise is between -1/2 ~ 1/2 [IEEE 2008].

(3) Bias Instability

Bias (in) stability is a fundamental measure that characterizes the best bias-drift performance under optimal averaging conditions. The origin of this noise is the electronics susceptible to random flickering (1/f) noise [IEEE 2008]. The related noise PSD is:

$$S_{\Omega}(f) = \begin{cases} \frac{B^2}{2\pi f} & f \leq f_0 \\ 0 & f > f_0 \end{cases} \quad (3.38)$$

Where:

B is the bias instability coefficient

f_0 is the cutoff frequency

It is derived as the minimum of the Allan-variance curve with a slope of zero. Bias stability describes long term stability of the gyroscope usually expressed in deg/h., i.e. how the bias changes over time at a constant condition. For short data samples, it is not usually possible to determine the bias instability as it is masked by the ARW.

Other types of noise contributors, such as quantization noise, rate random walk, and random rate can be examined as well; but they are not significant in MEMS gyroscopes. Assuming that the existing random processes are all statistically independent, the total Allan variance at any given τ is the sum of Allan variances due to the individual random processes at the same τ .

$$\sigma^2_{tot}(\tau) = \sigma^2_{ARW}(\tau) + \sigma^2_{BiasInst}(\tau) + \sigma^2_{Markov}(\tau) + \dots \quad (3.39)$$

3.3.2 Experimental Validation

Without losing the generality, here is a gyroscope modeling example to illustrate the modeling method above. The data is from Epson's XV-8100 MEMS heading gyroscope used in the first generation of PNS device. 1-hour's worth of static data was collected with the device in a stationary position at 25 Hz in a lab environment. Xing [Xing 2008] presents a systematic methodology for identifying constant, wide band Gaussian, and time-correlated errors from the post-calibration MEMS gyroscope data using Allan variance analysis. The limitation of this

method is the extracted parameters are quite sensitive to the signal processing and they are based on the assumption of separate independent models, so the estimation is not very robust. Here, a combination of Allan variance and time domain auto-correlation is applied to identify different bias terms introduced in Equation (3.19).

Since both the wide band Gaussian noise and first order Gauss-Markov processes have zero means, the time average of an ensemble of the experiments $x(t)$ can determine b_0 modeled as a random constant process. Zero rate bias: $b_0 = E\{x(t)\} = -0.0065 \text{ }^\circ/\text{s}$.

The choice of an appropriate model necessitates studying the autocorrelation $R(\tau)$ sequence of the sensor output: $R(\tau) = E(x(t)x(t+\tau))$. Some pre-processing is needed to separate wide band white noise and the time-correlated process in the gyroscope output. It is difficult to identify the correlated process directly from an autocorrelation plot, as wide band Gaussian noise is usually dominant in magnitude. Thus, a low-pass filter with a 1 Hz bandwidth is first applied on the gyroscope output. The time-correlated noise will remain almost unaltered during this filtering since T_c is usually much larger than 1 second. However, the Gaussian noise will be greatly attenuated so that the $R(\tau)$ becomes distinctive to extract. Figure 3-5 illustrates the raw and filtered gyroscope output; and Figure 3-5 shows the autocorrelation plotting after the filter.

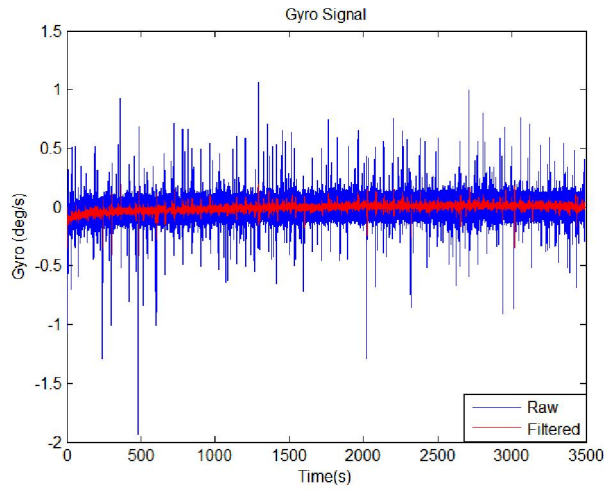


Figure 3-5 Filtered and raw gyroscope output

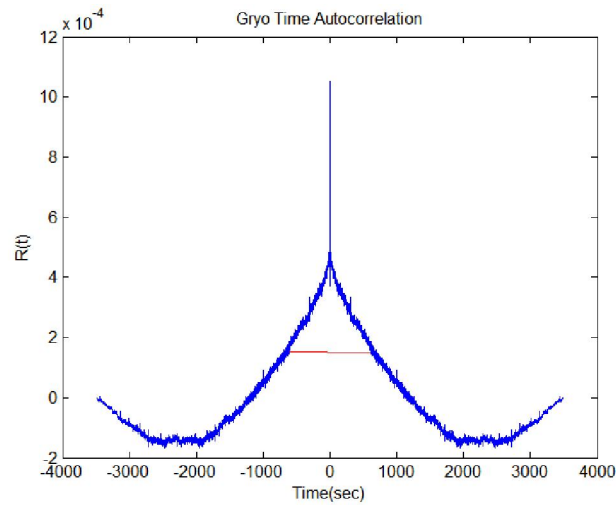


Figure 3-6 Filtered gyroscope autocorrelation plot

From the above figures, correlated time constant $T_c = 633s$, and first-order Markov process can well approximate the time-correlated noise with autocorrelation function as:

$$R(\Delta t) \approx 5 \times 10^{-4} \times e^{-\frac{|\Delta t|}{633}} \quad (3.40)$$

Finally, Allan Variance is plotted in Figure 3-7. ARW Gaussian noise can be seen as the dominate contributor. An ideal ARW curve of $0.015 \text{ } ^\circ/\text{s}/\sqrt{\text{Hz}}$ with a $-1/2$ slope is given and it overlaps with the overall Allan variance curve in the region with small cluster time (e.g. $T < 10\text{s}$). Note that $\sigma_{\text{bw}} \approx 0.06 \text{ } ^\circ/\text{s}$, which is equal to the value of the Allan variance when $T = T_s$ (T_s is the signal sampling period, 0.04 s in this example). The residual error is obtained by subtracting ARW from the overall Allan variance as shown by the red curve, which is approximate to an ideal time correlated noise; further indicating white noise and the 1st-order Markov process model is appropriate for this gyroscope output.

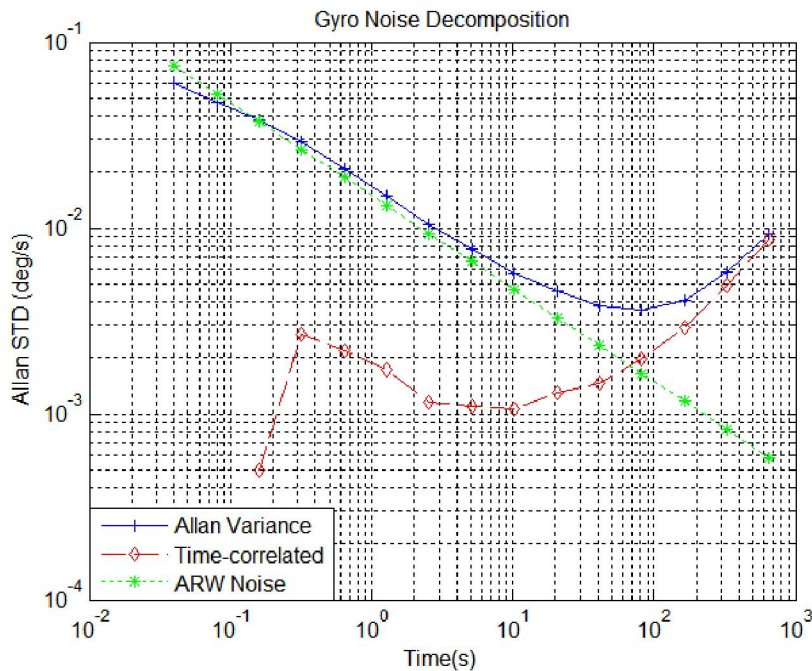


Figure 3-7 Allan variance plot of the filtered and raw gyroscope signals

3.4 Sensors Calibration

MEMS sensor calibration is essential to ensure navigation performance, especially for the nine-axis motion sensors fusion. This section deals with main error sources identified previous. It

includes biases calibration for gyroscopes and biases/scale factor calibration for magnetometers.

Usually the calibration procedure can be divided into two categories:

- **Initial offline sensors calibration:** accelerometers are calibrated using a static 6-position method [El-Sheimy 2009]. Biases and scale factors are estimated by aligning the measurement axis with positive and negative gravity vectors in three dimensions. The gyros' biases and scale factors are calibrated using a rotation table with known positive and negative angular velocities and magnetometers are calibrated by a 360-degree turning test [Honeywell 2003]. The max and min of the magnetometer readings are found throughout the measurement locus, and then used estimate the biases and scale factors accordingly to bring the mean of max and min to be zero, with the difference between them scaled to be the same for all three axes.
- **Online calibration:** this method is preferred because, unlike initial offline sensor calibration, drifting sensor errors are accounted for. The biases of gyroscopes can be estimated by detecting the zero rate offset and will be introduced in Section 3.4.1 below. The biases and scale factors of magnetometers are estimated by multiple orientation methods introduced in Section 3.4.2, below. However, the biases of the accelerometer are difficult to determine when the device is not leveled online, since the readings are coupled with gravity. Usually the accelerometer errors are not significant in the navigation equations and are thus neglected here. Finally, the barometer's error can be modeled as an additive bias and estimated from the GPS height, which will be introduced in Section 5.3.

3.4.1 Gyro Online Calibration

The gyro online calibration method is straightforward: continuously monitor if the device is in a stationary status; if so, average the output of the stationary time as a zero-rate offset. Therefore, stationary feature extraction is the key in this design.

Accelerometers are selected as stationary monitoring sensors for their low power consumption. Firstly, a recursive moving window is used to monitor sensor data. This window size is set as 1 second. The standard derivation of the accelerometer output within the window is calculated recursively in Equation (3.41)-(3.45).

$$x_n = \sqrt{a_x^2 + a_y^2 + a_z^2} \quad (3.41)$$

$$\bar{x}_n = \frac{(n-1)\bar{x}_{n-1} + x_n}{n} \quad (3.42)$$

$$\text{var}_{n-1} = (n-2) \cdot s_{n-1}^2 \quad (3.43)$$

$$\text{var}_n = \text{var}_{n-1} + \frac{n}{n-1} (\bar{x}_n - x_n)^2 \quad (3.44)$$

$$s_n = \sqrt{\frac{\text{var}_n}{n-1}} \quad (3.45)$$

Where:

n is the total sample number within recursive window

x_n is the sensor input of the current epoch

\bar{x}_{n-1} is the mean value of window in last epoch

\bar{x}_n is the mean value of window in current epoch

s_{n-1} is the standard deviation of window in last epoch

s_n is the standard deviation of window in current epoch

A stationary mode is declared when the standard derivation of the accelerometer amplitude within the recursive window is less than a pre-defined threshold, as shown below:

If $s_{accel} < ZUPT_accel_threshold$, then

ZUPT.accel_flag=1;

ZUPT.gyro_bias=mean(gyro_input).

3.4.2 Magnetometer Online Calibration

The degradation of the navigation solution from magnetometers is largely caused by the vulnerability of magnetometers to the ambient magnetic disturbance. These variations can be parameterized by biases and scale factors that can be corrected in online calibration. The calibration is based on the assumption that the total Earth magnetic field intensity is a constant value, so the calibrated biases and scale factor estimations should minimize this variation when the hard iron and soft iron errors are compensated for.

Referring to [Gebre 2006], iterative batch least squares estimation can be formulated based on multiple positions calibration. The locus of magnetometer measurements is described by:

$$\|h\|^2 = \left(\frac{\hat{h}_x^b - b_x}{\gamma_x} \right)^2 + \left(\frac{\hat{h}_y^b - b_y}{\gamma_y} \right)^2 + \left(\frac{\hat{h}_z^b - b_z}{\gamma_z} \right)^2 \quad (3.46)$$

Where:

$\hat{h}_x^b, \hat{h}_y^b, \hat{h}_z^b$ is the measurement of the raw magnetometer outputs

h is the norm of magnetic strength of the Earth, which can be determined based on the device's current location

b_x, b_y, b_z is the magnetometer biases

$\gamma_x, \gamma_y, \gamma_z$ is the magnetometer scale factors

For calibration using multiple positions, if k attitude measurements are selected, then we can construct k separate equations of (3.46). Expressing them in matrix form as:

$$- \begin{bmatrix} [\hat{h}_x^b(t_1)]^2 \\ [\hat{h}_x^b(t_2)]^2 \\ \dots \\ [\hat{h}_x^b(t_k)]^2 \end{bmatrix} = HX + v = \begin{bmatrix} H_{11} & H_{12} \end{bmatrix} \begin{bmatrix} b_x \\ \mu_1 b_y \\ \mu_2 b_z \\ \mu_1 \\ \mu_2 \\ \mu_3 \end{bmatrix} + v \quad (3.47)$$

Where the unknown vector X is:

$$X = [X(1) X(2) X(3) X(4) X(5) X(6)]^T = [b_x \ \mu_1 b_y \ \mu_2 b_z \ \mu_1 \ \mu_2 \ \mu_3]^T$$

H_{11} and H_{12} are two sub-matrices used to construct the measurement matrix H; v is the measurement noise vector.

$$H_{11} = \begin{bmatrix} -2\hat{h}_x^b(t_1) & -2\hat{h}_y^b(t_1) & -2\hat{h}_z^b(t_1) \\ -2\hat{h}_x^b(t_2) & -2\hat{h}_y^b(t_2) & -2\hat{h}_z^b(t_2) \\ \dots & \dots & \dots \\ -2\hat{h}_x^b(t_k) & -2\hat{h}_y^b(t_k) & -2\hat{h}_z^b(t_k) \end{bmatrix} \quad (3.48)$$

And:

$$H_{12} = \begin{bmatrix} [\hat{h}_y^b(t_1)]^2 & [\hat{h}_z^b(t_1)]^2 & 1 \\ [\hat{h}_y^b(t_2)]^2 & [\hat{h}_z^b(t_1)]^2 & 1 \\ \dots & \dots & \dots \\ [\hat{h}_y^b(t_k)]^2 & [\hat{h}_z^b(t_1)]^2 & 1 \end{bmatrix} \quad (3.49)$$

When the number of measurements, k, is greater than six, the least squares solution \hat{X} for (3.47)

is:

$$\hat{X} = (H'H)^{-1}H'z \quad (3.50)$$

From reference [Gebre 2006], a two-step estimator algorithm can be constructed. The first-step of the least squares solution includes the intermediate variables μ_1 μ_2 μ_3 and μ_4 .

$$\begin{aligned}\mu_1 &= \frac{\gamma_x^2}{\gamma_y^2} \\ \mu_2 &= \frac{\gamma_x^2}{\gamma_z^2} \\ \mu_3 &= b_x^2 + \mu_1 b_y^2 + \mu_2 b_z^2 - \mu_4 \\ \mu_4 &= h^2 \gamma_x^2 = (b_x^2 + \mu_1 b_y^2 + \mu_2 b_z^2) - \mu_3\end{aligned}\quad (3.51)$$

Finally in the second step, the biases and scale factors can be derived from (3.49) and (3.51) as:

$$\begin{aligned}\hat{b}_x &= \hat{x}(1) \\ \hat{b}_y &= \frac{\hat{x}(2)}{\hat{x}(4)} \\ \hat{b}_z &= \frac{\hat{x}(3)}{\hat{x}(5)} \\ \hat{\gamma}_x &= \sqrt{\frac{\mu_4}{h^2}} \\ \hat{\gamma}_y &= \sqrt{\frac{\mu_4}{\mu_1 h^2}} \\ \hat{\gamma}_z &= \sqrt{\frac{\mu_4}{\mu_2 h^2}}\end{aligned}\quad (3.52)$$

An indoor test was conducted to prove this concept. The device was rotated over 360 degrees at three orientations as shown in Figure 3-8 below.



(a) Orientation 1: horizontal (b) Orientation 2: 45° pitch (c) Orientation 3: -45° pitch

Figure 3-8 Multiple orientation magnetometers calibration

The magnetometers output without calibration and the total magnetic field strength is plotted in Figure 3-9 below. As can be seen, the total magnetic field varied significantly with the three orientations because of the large uncompensated z-axis biases.

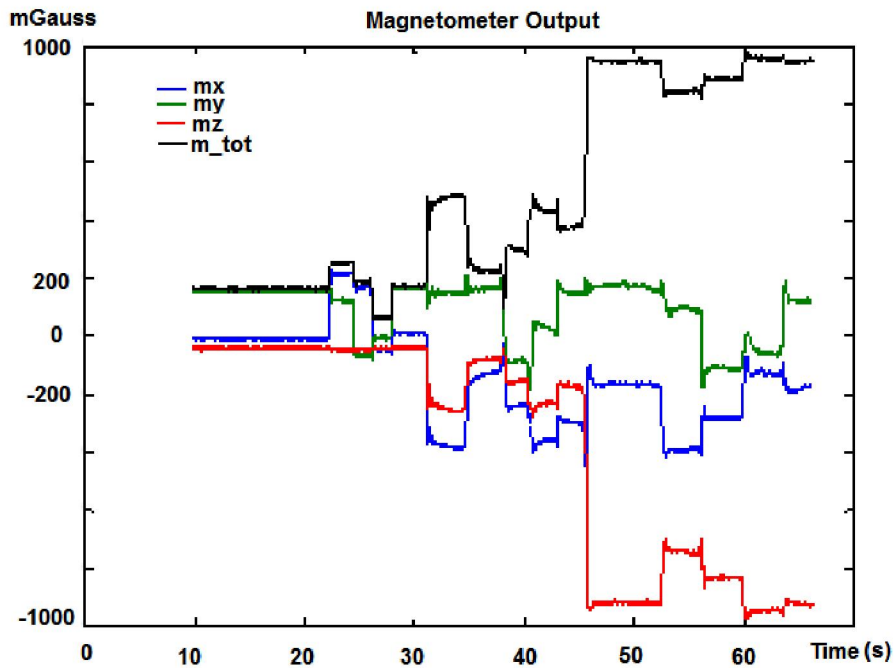


Figure 3-9 Magnetometers output without calibration

The first rotation with horizontal orientation was used for calibration. 6 points with different headings were randomly chosen. The calibration result is shown in Figure 3-10 as follows

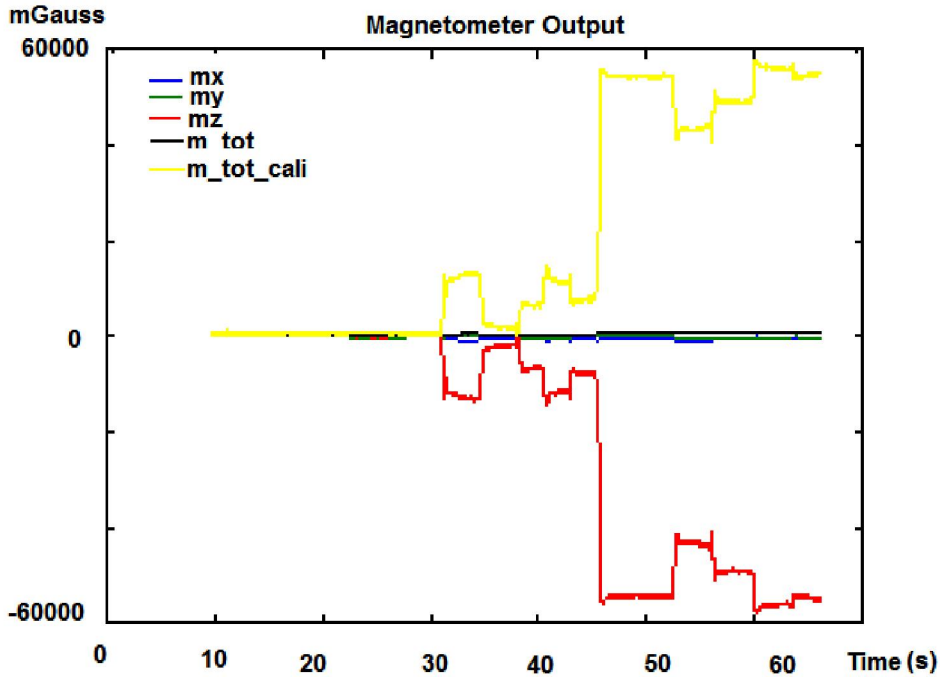


Figure 3-1 Magnetometers calibration using first orientation

The calibration brings the first rotation to constant magnitude, as shown in the yellow curve, but it is obvious that the 2nd and 3rd loops have very dramatic variations. Now, two more observations are added in the observation matrix from the second orientation (45-deg-pitch). The calibrated results are shown in Figure 3-11 below.

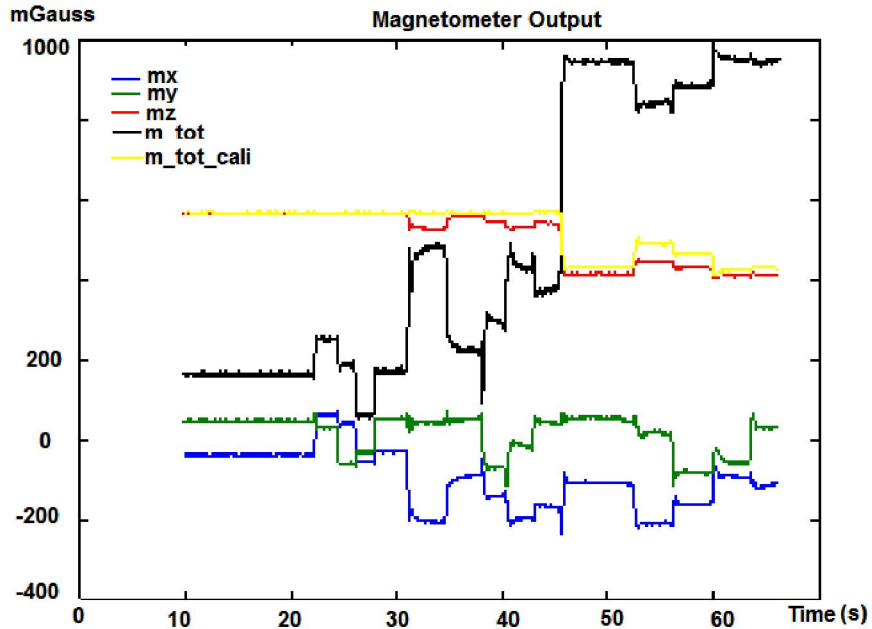


Figure 3-2 Magnetometers calibration using first and second orientation

With the observations data from the second attitude, the fluctuation of the total magnetic strength is reduced. However, the calibration result is still not perfect as variation is seen during the third rotation. Finally, another two observations are appended to the measurement matrix from the third orientation (-45 degree pitch). The result in Figure 3-12 shows a very constant total magnetic field strength.

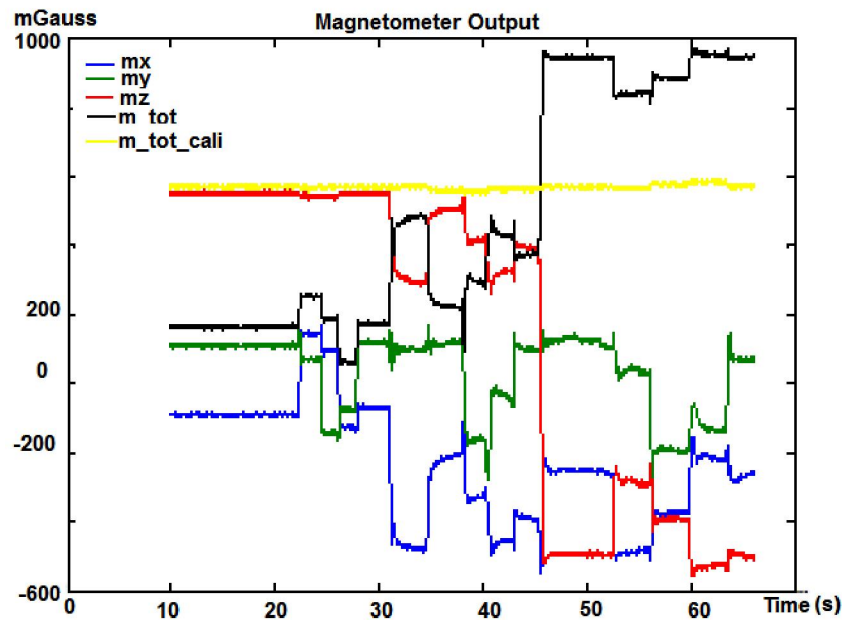


Figure 3-3 Magnetometers calibration using first, second and third orientation

From the above comparison, magnetometer calibration using two orientations sometimes fails to provide a satisfactory solution, especially for those orientations with less vertical variation.

However, calibration done with three orientations can quickly converge to a good calibration value. For practical deployment of online magnetometer calibration, a judicious selection of the magnetometer data collection is necessary. With insufficient heading and orientation changes, the measurement matrix is numerically singular and this leads to poor estimations. From the exemplary result, usually three independent orientations with some heading changes are required. The total number of the measurement points should be equal to or greater than six to solve for the unknown biases and scale factors.

Improved error modeling for low-cost MEMS sensors combined with efficient on-line calibration methods introduced in this chapter can enhance the design and performance of sensor fusion algorithms for personal navigation applications in the subsequent chapters.

Chapter Four: **ATTITUDE SENSORS FUSION**

Sensor fusion is heating up with its commercial implementations in smartphones and wearable devices. Sensors have different numbers of axes, also known as degrees of freedom (DOF), which they can record measurements around. Accelerometers and gyroscopes have up to 3 axes for measuring acceleration rotation rate, respectively, in three dimensional spaces (in X, Y, and Z coordinates); and magnetometers sense the Earth's magnetic field in three dimensional space. Magnetometers and accelerometers work together to provide a 6-axis eCompass solution for determining orientation. With the addition of a gyro, 9-axis attitude fusion can be performed to enable faster and more accurate orientation tracking of a device, on top of many other applications that a gyro can be used for.

Appendix C introduces how attitude is presented in three dimensional space, its coordinate definition and transformation. Then this chapter will construct an orientation Kalman filter design to integrate accelerometers, gyroscopes and magnetometers data. This unified sensors fusion framework can flexibly switch between 3-axis gyro only, 6-axis acc+mag, 6-axis acc+gyro and 9-axis acc+mag+gyro solutions based on sensors availability and input signal quality; therefore, the attitude fusion can maintain accuracy while minimize power consumption and computational complexity.

4.1 Attitude Kalman Filter Design

4.1.1 The State Equation

Real-time attitude estimation has been implemented by Kalman filter based sensor fusion solutions for decades. Given the initial attitudes, the three dimensional attitudes are continuously

calculated from the angular velocity of the device, obtained from the three-axis gyroscope measurements. The attitude kinematic equations represented by quaternions are preferred because of its non-singularities characteristics. In addition, the attitude states are augmented by additional state-vector components of the three gyro biases. Thus gyro data is not treated as Kalman filter measurements and the gyro noise appears as a state noise rather than measurement noise [Lefferts 1982]. In nine-axis sensor fusion architecture, the three-axis accelerometers, gyroscopes and magnetometers are related to the device's orientation, known as vector attitude observations; they are used in the Kalman filter measurements updates. There are two methods in the quaternion attitude prediction, as shown below.

The first method is based on conventional Additive EKF (AEKF), first introduced by I.Y. Bar-Itzhack [Bar 1985]. It treats the four quaternion components as independent parameters. The true attitude quaternion $\bar{q}(t)$ is related to quaternion error $\delta\bar{q}(t)$ and estimate $\hat{q}(t)$ as:

$$\bar{q}(t) = \hat{q}(t) + \delta\bar{q}(t) \quad (4.1)$$

An alternative approach, known as Multiplicative EKF (MEKF), defines the attitude as the quaternion product below [Markley 2004].

$$\bar{q}(t) = \delta\bar{q}(t) \otimes \hat{q}(t) \quad (4.2)$$

Where $\delta\bar{q}(t)$ represents a small rotation from estimated attitude $\hat{q}(t)$ to true attitude $\bar{q}(t)$ in the body frame. Equivalently, the error quaternion can be expressed as:

$$\delta\bar{q}(t) = \bar{q}(t) \otimes \hat{q}^{-1}(t) \quad (4.3)$$

In the AEKF definition above, the additive correction of $\delta\bar{q}(t)$ can impact unity normalization without proper constraint. Consequently, the attitude errors are correlated with the quaternion norm errors. Then the 4 by 4 quaternion covariance matrix becomes singular which poses difficulty for Kalman filter. On the contrary, in the MEKF the definition of $\delta\bar{q}(t)$ is guaranteed to be a normalized quaternion correction by the nature of its quaternion product derivation, thus avoids any singularity of discontinuity of the three dimensional parameterization.

A simple three-axis gyro model is given by [Crasdi 2004]:

$$\omega = \omega_m - \hat{b} - \eta_v = \hat{\omega} - \eta_v \quad (4.4)$$

Where \hat{b} is the gyro bias vector and η_v is Gaussian white noise; \hat{b} itself is driven by a white-noise process η_u as:

$$\dot{\hat{b}} = \eta_u \quad (4.5)$$

By taking the derivative of the above Equation (4.3) and substituting the quaternion kinematic equations of $\dot{\bar{q}}(t)$ and $\dot{\hat{q}}^{-1}(t)$, it leads to:

$$\delta\dot{\bar{q}}(t) = \frac{1}{2} \left\{ \begin{bmatrix} \omega \\ 0 \end{bmatrix} \otimes \delta\bar{q}(t) - \delta\bar{q}(t) \otimes \begin{bmatrix} \hat{\omega} \\ 0 \end{bmatrix} \right\} \quad (4.6)$$

Where the true and estimated angular velocity are denoted by ω and $\hat{\omega}$ respectively with the following relationship:

$$\hat{\omega} = \omega_m - \hat{b} = \omega + b + \eta_v - \hat{b} = \omega + \delta b + \eta_v \quad (4.7)$$

In the above equation, the estimated gyro bias, \hat{b} , is subtracted from the gyro measurement ω_m as the estimated $\hat{\omega}$ in the system equations.

Quaternion error and gyro bias as a state vector form a seven-dimensional attitude representation, which is the most direct implementation. However it is computationally undesired, not only because one extra dimension increases the matrix size, but more importantly, as stated previously, the covariance matrix for the seven-dimensional state-vector is singular because of the one dimensional quaternion redundancy from the quaternion norm constraint [Lefferts 1982]. Therefore, a three-parameter attitude state propagation model is developed to preserve the proper rank. The following section introduces how to develop the state dynamic matrix with a rank of 6.

The first-order $\delta\dot{\bar{q}}(t)$ approximation can be obtained as below:

$$\delta\dot{\bar{q}}(t) = \begin{bmatrix} \delta\dot{\rho} \\ \delta\dot{q}_4 \end{bmatrix} \approx \begin{bmatrix} -[\hat{\omega} \times] \delta\rho - \frac{1}{2}(\delta b + \eta_v) \\ 0 \end{bmatrix} \quad (4.8)$$

It removes the quaternion redundancy by estimating its vector components only, and the scalar component is approximately a constant [Crassidi 2004]. The detailed derivation is given in

Appendix D.1.

For a small quaternion rotation $\delta\bar{q}(t)$, defined by assuming the true quaternion is close to the estimated quaternion, $\delta\rho = \frac{1}{2}\delta\alpha$, where $\delta\alpha$ is the attitude vector of roll, pitch, and yaw error angles, we can rewrite the above Equation (4.6) using error angles representation:

$$\delta\dot{\alpha} = -[\hat{\omega}\times]\delta\alpha - \frac{1}{2}(\delta b + \eta_v) \quad (4.9)$$

$$\delta\dot{b} = \eta_u \quad (4.10)$$

$$\text{Where, } [\hat{\omega}\times] = \begin{bmatrix} 0 & -\hat{\omega}_z & \hat{\omega}_y \\ \hat{\omega}_z & 0 & -\hat{\omega}_x \\ -\hat{\omega}_y & \hat{\omega}_x & 0 \end{bmatrix}$$

Now we express the above dynamic equations in Kalman filter error state model as:

$$\dot{x}(t) = F(t)x(t) + G(t)w(t) \quad (4.11)$$

Then the error state $x(t)$, dynamic matrix $F(t)$, noise vector $w(t)$, and noise driving matrix $G(t)$ are given by:

$$x(t) = \begin{bmatrix} \delta\alpha \\ \delta b \end{bmatrix}, \quad F(t) = \begin{bmatrix} -[\hat{\omega}\times] & -I_{3\times 3} \\ 0_{3\times 3} & 0_{3\times 3} \end{bmatrix} \quad (4.12)$$

$$w(t) = \begin{bmatrix} \eta_v \\ \eta_u \end{bmatrix} \quad (4.13)$$

$$G(t) = \begin{bmatrix} -I_{3\times 3} & 0_{3\times 3} \\ 0_{3\times 3} & I_{3\times 3} \end{bmatrix} \quad (4.14)$$

Based on the above approximation, the system state vector and matrices are reduced to 6 dimensions.

4.1.2 Kalman Filter Processing Flow

Since orientation transformation and fusion is a non-linear process, an Extend Kalman Filter (EKF) is used to linearize the process about the current state. Therefore the transition matrix F and design matrix H are first-order partial derivative of the error states as given in the subsequent Section 4.1.3 and Section 4.1.4. Based on the attitude state estimation developed in Section 4.1.1, the overall framework of nine-axis sensors orientation fusion by a Kalman filter is developed, as shown in the flowchart in Figure 4-1.

The fusion processing is triggered by sensor measurements, that is, whenever a new measurement of any sensor type is available, the Kalman filter routine will be executed. In this framework, three kinds of attitude fusion can be computed based on: (1) gyro-only measurements; (2) six-axis (accelerometer+ magnetometer) measurements; (3) nine-axis (gyro+ accelerometer +magnetometer) measurements. They are used to compare and tune the fusion performance.

The Kalman filter starts with state and covariance initialization, which will be introduced in detail in Section 4.1.2.1. Subsequently, raw sensor measurements will be calibrated, the initial calibration parameters will be derived at the initialization stage with a preferred calibration operation such as measurements from the navigation body in a static state to detect the gyro and accelerometer's zero output rate biases, and/or a figure-8 maneuver to estimate the magnetometer biases and scale factors. The calibration details were introduced in Section 3.5.

Then, if gyro measurements are available, the Kalman filter can predict the quaternion, gyro bias, error covariance matrix P , and process noise matrix Q , based on the current observations.

Subsequently, the gyro-only attitude is computed by converting the quaternions into DCM/Euler angles. Section 4.1.3 gives implementation details for this system process propagation.

Next when Kalman filter measurement data is available, either coming from the accelerometer or magnetometer observation vectors, the Kalman Filter update stage is launched. First the magnetometer and accelerometer-based attitude can be calculated directly without Kalman fusion. Then measurement matrix H and measurement noise matrix R can be formed. After calculating the Kalman Filter gain K , all the states and error covariance can be updated. During the update stage, the complete nine-axis sensors based attitude can be generated, again by converting the updated quaternion into DCM/Euler angles. Section 4.1.4 gives implementation details for the measurements update procedure.

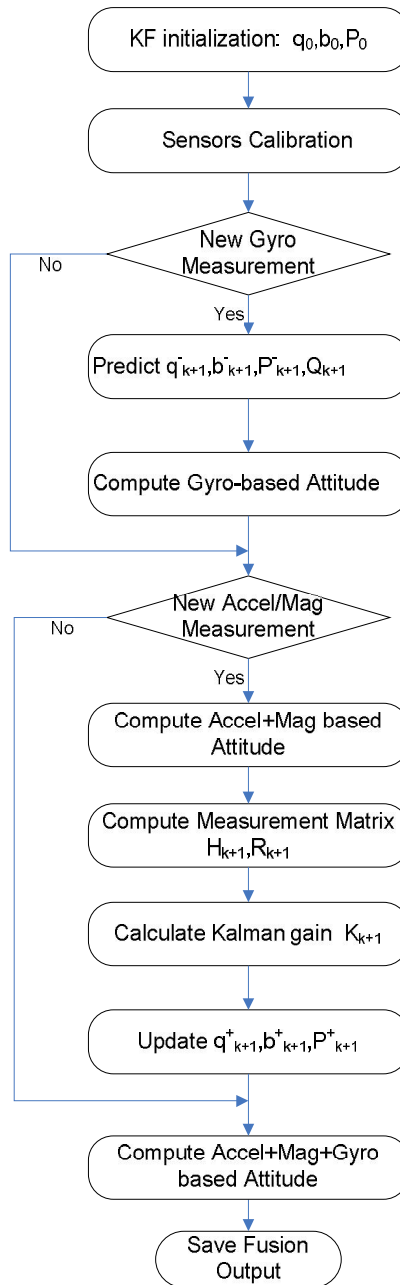


Figure 4-1 Kalman filter flow for 9-axis orientation fusion

4.1.2.1 Filter Initialization

The Kalman filter is first initialized with a known state: the initial gyro biases are assumed to be zero after calibration; the initial attitude is derived using vector matching to derive the rotation

matrix. The state error covariance matrix P_0 has diagonal elements which correspond to attitude and gyro errors.

Initialization starts when the device is in a static state. A certain period of time is used to average the measurement from accelerometers, gyroscopes, and magnetometers. Denote \mathbf{x}^n as a vector in the navigation frame and denote \mathbf{x}^b as a vector in the body frame. Referring to Section 4.1.3, the rotational matrix C_b^n can be constructed as

$$\mathbf{x}^n = C_b^n \mathbf{x}^b = \begin{pmatrix} \mathbf{i}_b \cdot \mathbf{i}_n & \mathbf{j}_b \cdot \mathbf{i}_n & \mathbf{k}_b \cdot \mathbf{i}_n \\ \mathbf{i}_b \cdot \mathbf{j}_n & \mathbf{j}_b \cdot \mathbf{j}_n & \mathbf{k}_b \cdot \mathbf{j}_n \\ \mathbf{i}_b \cdot \mathbf{k}_n & \mathbf{j}_b \cdot \mathbf{k}_n & \mathbf{k}_b \cdot \mathbf{k}_n \end{pmatrix} \mathbf{x}^b \quad (4.15)$$

Where $\mathbf{i}, \mathbf{j}, \mathbf{k}$ are the vector bases along the east, north and up direction.

Ideally two vectors are known apriori in the navigation frame: the specific force vector $[0 \ 0 \ g]^n$ and magnetic north vector $[0 \ m \ 0]^n$. Along with their cross product, they form $\mathbf{k}_n, \mathbf{j}_n, \mathbf{i}_n$ in the DCM equation above. Note this is under the assumption that no extra acceleration and magnetic interference is imposed on the device.

Then the accelerometers and magnetometer measurements and their cross product form the up, north, and east vector in the body frame.

$$up = \begin{bmatrix} \bar{a}_x \\ \bar{a}_y \\ \bar{a}_z \end{bmatrix}^b$$

$$\begin{aligned}
\overline{up} &= \frac{up}{\|up\|} \\
east &= \begin{bmatrix} \overline{m}_x \\ \overline{m}_y \\ \overline{m}_z \end{bmatrix}^b \times \overline{up} \\
\overline{north} &= \overline{up} \times \overline{east} \\
\overline{east} &= \frac{east}{\|east\|}
\end{aligned} \tag{4.16}$$

After applying the dot multiplication in the transformation matrix between the body frame and the navigation frame, we can normalize the vectors. C_b^n can be initialized as:

$$C_b^n = \begin{bmatrix} \overline{east} \\ \overline{north} \\ \overline{up} \end{bmatrix} \tag{4.17}$$

Finally, initial quaternions can be converted from the rotation matrix using the method introduced in the DCM-to-quaternion conversion previously introduced.

4.1.3 Discrete-time State Equations

4.1.3.1 Quaternion Propagation

Although the state covariance matrix reduces to the vector components of the quaternion as introduced in introduced in Section 4.1.1, four elements quaternions are still included as the estimated state due to their strength with attitude representation. Quaternion is propagated by its kinematic equation. Rewriting the quaternion differential equation introduced previously, we get:

$$\begin{aligned} \bar{\dot{q}} = \begin{bmatrix} \dot{q}_1 \\ \dot{q}_2 \\ \dot{q}_3 \\ \dot{q}_4 \end{bmatrix} &= \frac{1}{2} \Omega(\omega) \bar{q} = \frac{1}{2} \begin{bmatrix} -\omega \times & \omega \\ -\omega^T & 0 \end{bmatrix} \begin{bmatrix} q_1 \\ q_2 \\ q_3 \\ q_4 \end{bmatrix} = \frac{1}{2} \begin{bmatrix} 0 & \omega_z & -\omega_y & \omega_x \\ -\omega_z & 0 & \omega_x & \omega_y \\ \omega_y & -\omega_x & 0 & \omega_z \\ -\omega_x & -\omega_y & -\omega_z & 0 \end{bmatrix} \begin{bmatrix} q_1 \\ q_2 \\ q_3 \\ q_4 \end{bmatrix} \end{aligned} \quad (4.18)$$

The discrete-time quaternion can be derived from exponential power series:

$$q_{k+1} = e^{\int_k^{k+1} \frac{1}{2} \Omega(\omega) dt} q_k = \Phi_q(\omega) q_k \quad (4.19)$$

Assuming ω is constant over the integration period, the quaternion transition matrix $\Phi_q(\omega)$ can be obtained as:

$$\Phi_q(\omega) = \begin{bmatrix} \cos \frac{\|\theta\|}{2} I_{3 \times 3} - \hat{\psi}_k^+ \times & \hat{\psi}_k^+ \\ -\hat{\psi}_k^{+T} & \cos \frac{\|\theta\|}{2} \end{bmatrix} = \begin{bmatrix} \cos \frac{\|\theta\|}{2} & \frac{\theta_z}{\|\theta\|} \sin \frac{\|\theta\|}{2} & -\frac{\theta_y}{\|\theta\|} \sin \frac{\|\theta\|}{2} & \frac{\theta_x}{\|\theta\|} \sin \frac{\|\theta\|}{2} \\ -\frac{\theta_z}{\|\theta\|} \sin \frac{\|\theta\|}{2} & \cos \frac{\|\theta\|}{2} & \frac{\theta_x}{\|\theta\|} \sin \frac{\|\theta\|}{2} & \frac{\theta_y}{\|\theta\|} \sin \frac{\|\theta\|}{2} \\ \frac{\theta_y}{\|\theta\|} \sin \frac{\|\theta\|}{2} & -\frac{\theta_x}{\|\theta\|} \sin \frac{\|\theta\|}{2} & \cos \frac{\|\theta\|}{2} & \frac{\theta_z}{\|\theta\|} \sin \frac{\|\theta\|}{2} \\ -\frac{\theta_x}{\|\theta\|} \sin \frac{\|\theta\|}{2} & -\frac{\theta_y}{\|\theta\|} \sin \frac{\|\theta\|}{2} & -\frac{\theta_z}{\|\theta\|} \sin \frac{\|\theta\|}{2} & \cos \frac{\|\theta\|}{2} \end{bmatrix} \quad (4.20)$$

Where:

$$\theta_i = \omega_i \Delta t \quad i=x,y,z$$

$$\|\theta\| = \sqrt{\omega_x^2 + \omega_y^2 + \omega_z^2} \Delta t$$

$$\widehat{\psi}_k^+ = \begin{bmatrix} \frac{\theta_x}{\|\theta\|} \sin \frac{\|\theta\|}{2} \\ \frac{\theta_y}{\|\theta\|} \sin \frac{\|\theta\|}{2} \\ \frac{\theta_z}{\|\theta\|} \sin \frac{\|\theta\|}{2} \end{bmatrix} = \begin{bmatrix} q_1 \\ q_2 \\ q_3 \end{bmatrix}_k^+$$

$$\widehat{\psi}_k^{+\times} = \begin{bmatrix} 0 & -\frac{\theta_z}{\|\theta\|} \sin \frac{\|\theta\|}{2} & \frac{\theta_y}{\|\theta\|} \sin \frac{\|\theta\|}{2} \\ \frac{\theta_z}{\|\theta\|} \sin \frac{\|\theta\|}{2} & 0 & -\frac{\theta_x}{\|\theta\|} \sin \frac{\|\theta\|}{2} \\ -\frac{\theta_y}{\|\theta\|} \sin \frac{\|\theta\|}{2} & \frac{\theta_x}{\|\theta\|} \sin \frac{\|\theta\|}{2} & 0 \end{bmatrix}$$

The detailed derivation for the quaternion transition matrix $\Phi_q(\omega)$ above is given in **Appendix**

D.2.

4.1.3.2 State Transition Equations

To avoid the singularity of the state covariance matrix, the transition matrix and the state covariance matrix are computed as 6 by 6 matrices, as previously introduced.

From the system dynamic matrix, $F(t)$ in continuous time given in Equation (4.12), the state transition matrix Φ is:

$$\Phi(t, t_0) = e^{\int_{t_0}^t F(\tau) d\tau} \quad (4.21)$$

Φ has the block matrix structure as:

$$\Phi = \begin{bmatrix} \Phi_{00} & \Phi_{10} \\ 0 & 1 \end{bmatrix} \quad (4.22)$$

Where:

$$\begin{aligned} \Phi_{00} &= I_{3 \times 3} - \frac{\sin(\|\omega\| \Delta t)}{\|\omega\|} (\omega \times) + \frac{1 - \cos(\|\omega\| \Delta t)}{\|\omega\|^2} (\omega \times)(\omega \times) \\ &= I_{3 \times 3} - \frac{\sin\|\theta\|}{\|\theta\|} (\theta \times) + \frac{1 - \cos\|\theta\|}{\|\theta\|^2} (\theta \times)(\theta \times) \end{aligned}$$

$$\begin{aligned} \Phi_{10} &= \frac{1 - \cos(\|\omega\| \Delta t)}{\|\omega\|^2} (\omega \times) - \frac{\|\omega\| \Delta t - \sin(\|\omega\| \Delta t)}{\|\omega\|^3} (\omega \times)(\omega \times) - I_{3 \times 3} \Delta t \\ &= \left[\frac{1 - \cos(\|\theta\|)}{\|\theta\|^2} (\theta \times) - \frac{\|\theta\| - \sin(\|\theta\|)}{\|\theta\|^3} (\theta \times)(\theta \times) - I_{3 \times 3} \right] \Delta t \end{aligned}$$

$$\omega \times = \begin{bmatrix} 0 & -\omega_z & \omega_y \\ \omega_z & 0 & -\omega_x \\ -\omega_y & \omega_x & 0 \end{bmatrix}$$

$$\theta \times = \begin{bmatrix} 0 & -\theta_z & \theta_y \\ \theta_z & 0 & -\theta_x \\ -\theta_y & \theta_x & 0 \end{bmatrix} = \begin{bmatrix} 0 & -\omega_z & \omega_y \\ \omega_z & 0 & -\omega_x \\ -\omega_y & \omega_x & 0 \end{bmatrix} \Delta t$$

The detailed derivation is introduced in **Appendix D.3**

4.1.3.3 Process Noise Covariance

As introduced in Section 4.1.3.1, two types of gyro errors are important for consideration, one is a short-term component of instability referred to as random drift η_r and is directly included with angular velocity measurements; the other is a random walk η_w , included in the gyro biases term.

Both errors can be considered as zero-mean Gaussian white-noise processes with variances of

σ_v^2 and σ_u^2 , respectively. Assume η_v and η_u to be independent from Equation (4.13), the continuous time noise covariance Q_c can be derived as:

$$Q_c = E[w(t)w(t+\tau)'] = \begin{bmatrix} \sigma_u^2 I_{33} & 0_{33} \\ 0_{33} & \sigma_v^2 I_{33} \end{bmatrix} \quad (4.23)$$

Computing in discrete-time form, the noise covariance matrix Q_d is:

$$Q_d = \int_{t_k}^{t_{k+1}} \Phi(t_{k+1}, \tau) G(\tau) Q_c G^t(\tau) \Phi^t(t_{k+1}, \tau) d\tau \quad (4.24)$$

Substituting Equations (4.14),(4.22),(4.23) into equation above and after some simplifications, Q_d is given by Equation (4.25) below [Crassidi 2004]:

$$Q_d = \begin{bmatrix} (\sigma_v^2 \Delta t + \frac{1}{3} \sigma_u^2 \Delta t^3) I_{33} & (\frac{1}{2} \sigma_u^2 \Delta t^2) I_{33} \\ (\frac{1}{2} \sigma_u^2 \Delta t^2) I_{33} & (\sigma_u^2 \Delta t) I_{33} \end{bmatrix} \quad (4.25)$$

4.1.3.4 State Covariance Matrix

Finally, the state covariance matrix P is derived from the system state transition matrix Φ .

Substitute Φ into covariance propagation equation to get:

$$P_{k+1}^- = \Phi \cdot P_k^+ \cdot \Phi^T + Q_d \quad (4.26)$$

4.1.4 Measurement Update

Attitude Kalman filters require periodic measurement updates to correct system propagation errors. A three-dimensional accelerometer vector and a three-dimensional magnetometer vector are used as orientation measurements. At time t_k , the measurement vector Z_k is related to the state vector X_k by:

$$Z_k = h(X_k) + v_k \quad (4.27)$$

Where v_k is the measurement noise and it is usually modeled as a Gaussian white-noise process. According to the reference in [Crassidi 2004], sensitivity matrix H_k in the nonlinear EKF is given by:

$$H_k(x_k^-) = \frac{\partial h(x)}{\partial x} \quad (4.28)$$

The Kalman filter update is performed whenever accelerometer or magnetometer measurements are valid, which can be available at different time epochs based on the actual sensors rate.

4.1.4.1 Accelerometer Measurement

To derive the measurement sensitive matrix, the measurement residual Δz needs to be related with the state vector. Both the actual measurement, z_m , and the predicted measurement, \hat{z} , are measured in the body frame, thus the rotation matrix can be written as:

$$\Delta z = z_m - \hat{z} = C_n^b(\bar{q})r - C_n^b(\hat{q}^-)r \quad (4.29)$$

Where r is the sensor measurement in the reference navigation frame.

Using multiplicative quaternions given in Equation (4.2),

$$C_n^b(\bar{q}) = C_n^b(\delta\bar{q} \otimes \hat{q}) \approx (I - [\delta\alpha_x])C_n^b(\hat{q}) \quad (4.30)$$

Substituting (4.30) into (4.29) yields

$$\Delta z = -[\delta\alpha_x][C_n^b(\hat{q})r] = [C_n^b(\hat{q})r_x]\delta\alpha \quad (4.31)$$

Therefore the measurement matrix H is given as below:

$$H_k(x_k^-) = \frac{\partial h(x)}{\partial x} = \begin{bmatrix} C_n^b(\hat{q}^-)r_x & 0_{3 \times 3} \end{bmatrix} \quad (4.32)$$

Here, the zero matrix is on the right side because the gyro bias state is independent of the measurement vectors.

The accelerometers measure the specific force f^b in the body frame as

$$f^b = a^b - g^b \quad (4.33)$$

Where a^b is device's kinematic acceleration and g^b is the Earth's gravitational acceleration, it is negative by the ENU definition.

When the device is in a static state, ($a^b = 0$), the predicted specific force, \hat{f}^b , is positive upward and can be expressed as:

$$\hat{f}^b = C_n^b g^n = C_n^b [0 \ 0 \ 1]^T \quad (4.34)$$

Where g^n is the normalized gravity in the reference navigation frame.

The acceleration measurements $[a_x, a_y, a_z]^T$ are also normalized in the orientation update calculation. Referring to Equation (4.31), the accelerometers measurement residual Δz is:

$$\Delta z = Z_a - C_n^b(\hat{q}^-)g^n = \frac{1}{\sqrt{a_x^2 + a_y^2 + a_z^2}} \begin{bmatrix} a_x \\ a_y \\ a_z \end{bmatrix} - C_n^b(\hat{q}^-) \begin{bmatrix} 0 \\ 0 \\ 1 \end{bmatrix} \quad (4.35)$$

The measurement sensitivity matrix H_a is:

$$H_a = [C_n^b(\hat{q}^-)a \times \ 0_{3 \times 3}] \quad (4.36)$$

4.1.4.2 Magnetometer Measurement

Geomagnetic heading from magnetometer measurements are derived in a similar way.

From Equation (4.35), the north vector is formed from magnetometer and accelerometer measurements; the predicted north vector after normalization in the body frame can be written as:

$$\hat{m}^b = C_n^b(\hat{q}^-)m^n = C_n^b(\hat{q}^-)[0 \ 1 \ 0]^T \quad (4.37)$$

Therefore the magnetometers measurement residual Δz is:

$$\Delta z = Z_a - C_n^b(\hat{q}^-)m^n = \overline{north} - C_n^b(\hat{q}^-) \begin{bmatrix} 0 \\ 1 \\ 0 \end{bmatrix} \quad (4.38)$$

The measurement sensitivity matrix H_m is given below:

$$H_m = [C_n^b(\hat{q}^-)m \times \quad 0_{3 \times 3}] \quad (4.39)$$

Note this measurement update is valid only when the magnetic field vector is not aligned with gravity vector, that is, not near the Earth's magnetic north pole.

4.1.4.3 Measurement Noise and Adaptive Selection

The accelerometer measurement expressed in Equation (4.34) above is an ideal case where the device is in a static state. The magnetometer measurement expressed in Equation (4.37) is also an ideal case without any magnetic disturbance. In practice, more factors should be considered.

Rewriting Equations (4.34), (4.37) together, the predicted measurements vector is:

$$\hat{z} = h(\hat{q}^-) = \begin{bmatrix} K_{sf}^a C_n^b(\hat{q}^-) & 0 \\ 0 & K_{sf}^m C_n^b(\hat{q}^-) \end{bmatrix} \begin{bmatrix} -g + a^{dev} \\ m^{earth} + m^{ext} \end{bmatrix} + \begin{bmatrix} b^a \\ b^m \end{bmatrix} + \begin{bmatrix} v^a \\ v^m \end{bmatrix} \quad (4.40)$$

Where:

K_{sf}^a and b^a are the scale factor and bias vector of the accelerometers, respectively;

K_{sf}^m and b^m are the scale factor and bias vector of the magnetometers respectively;

a^{dev} is the device additional acceleration;

m^{earth} is the local geomagnetic field and m^{ext} is the external disturbance;

v^a and v^m are measurement noise modeled by zero-mean Gaussian white-noise process with variance of σ_a^2 and σ_m^2 respectively.

Since the measurements put into EKF filter are normalized, measurement noise should also be divided by its norm. To simplify the Kalman filter estimation, the accelerometer biases and scale factors can be corrected in the calibration stage, thus are not included in the Kalman filter equations. Similarly, magnetometer biases and scale factors can be corrected from an online calibration module, separately.

When a large a^{dev} is detected, σ_a^2 will be set large accordingly to decrease the magnetometer weight or simply not use it at all. When the motion is significant; m^{ext} is hard to estimate when the external disturbance is not obvious since it can be absorbed into the online calibration filter. Nevertheless, when large magnetic deviation from the normal strength of Earth's magnetic field is observed, the measurement noise σ_m^2 should be set large.

4.1.4.4 Kalman Filter Gain Matrix

The Kalman filter gain is calculated as

$$K_{k+1} = P_{k+1}^- H_{k+1}^T (H_{k+1} P_{k+1}^- H_{k+1}^T + R_{k+1})^{-1} \quad (4.41)$$

We can divide the 6 by 6 matrix into sub blocks to reduce the calculation complexity:

$$\begin{aligned}
K_{k+1} &= \begin{bmatrix} K_0 \\ K_1 \end{bmatrix} = \begin{bmatrix} P_{00} & P_{10} \\ P_{01} & P_{11} \end{bmatrix} \begin{bmatrix} H_0^T \\ 0 \end{bmatrix} (H_0 P_{00} H_0^T + R_{k+1})^{-1} \\
&= \begin{bmatrix} P_{00} H_0^T (H_0 P_{00} H_0^T + R_{k+1})^{-1} \\ P_{01} H_0^T (H_0 P_{00} H_0^T + R_{k+1})^{-1} \end{bmatrix}
\end{aligned} \tag{4.42}$$

4.1.4.5 State and Covariance Update

$$X_{k+1}^+ = X_{k+1}^- + K_{k+1} (Z_{k+1} - H_{k+1} X_{k+1}^-) \tag{4.43}$$

Since $x(t) = \begin{bmatrix} \delta\alpha \\ \delta b \end{bmatrix}$, the angle and biases in the state can be calculated separately as:

$$\delta\alpha_{k+1}^+ = K_0 (Z_{k+1} - H_{k+1} \delta\alpha_{k+1}^-) \tag{4.44}$$

$$\delta b_{k+1}^+ = K_0 (Z_{k+1} - H_{k+1} \delta b_{k+1}^-) \tag{4.45}$$

Then update the quaternion accordingly as:

$$\begin{aligned}
q_{k+1}^+ &= \delta\bar{q}_{k+1} \otimes \hat{q}_{k+1}^- = \begin{bmatrix} \frac{\delta\alpha_{k+1}}{2} \\ 1 \end{bmatrix} \otimes \hat{q}_{k+1}^- = \begin{bmatrix} 1 & \frac{\delta\alpha_{kz}}{2} & -\frac{\delta\alpha_{ky}}{2} & \frac{\delta\alpha_{kx}}{2} \\ -\frac{\delta\alpha_{kz}}{2} & 1 & \frac{\delta\alpha_{kx}}{2} & \frac{\delta\alpha_{ky}}{2} \\ \frac{\delta\alpha_{ky}}{2} & -\frac{\delta\alpha_{kx}}{2} & 1 & \frac{\delta\alpha_{kz}}{2} \\ -\frac{\delta\alpha_{kx}}{2} & -\frac{\delta\alpha_{ky}}{2} & -\frac{\delta\alpha_{kz}}{2} & 1 \end{bmatrix} \begin{bmatrix} \bar{q}_{k+1,0}^- \\ \bar{q}_{k+1,1}^- \\ \bar{q}_{k+1,2}^- \\ \bar{q}_{k+1,3}^- \end{bmatrix} \\
&= \bar{q}_{k+1}^- + \frac{1}{2} \begin{bmatrix} q_3 & -q_2 & q_1 \\ q_2 & q_3 & -q_0 \\ -q_1 & q_0 & q_3 \\ -q_0 & -q_1 & -q_2 \end{bmatrix}_{k+1} \begin{bmatrix} \delta\alpha_{kx} \\ \delta\alpha_{ky} \\ \delta\alpha_{kz} \end{bmatrix}
\end{aligned} \tag{4.46}$$

Brute-force normalization is applied to preserve the unity from calculation errors.

Then update gyro bias and rotation rate as:

$$\hat{b}_{k+1}^+ = \hat{b}_{k+1}^- + \delta b_{k+1}^+ \quad (4.47)$$

$$\hat{\omega}_{k+1}^+ = \omega_{k+1} - \hat{b}_{k+1}^+ \quad (4.48)$$

Finally, compute the updated covariance matrix as:

$$P_{k+1}^+ = [I_{6*6} - K_{k+1} H_{k+1}] P_{k+1}^- [I_{6*6} - K_{k+1} H_{k+1}]^T + K_{k+1} R_{k+1} K_{k+1}^T \quad (4.49)$$

4.2 Attitude Fusion Test

4.2.1 Rotation Test Setup

This test was conducted at a conference room in an office building; it is a spacious indoor environment without much electromagnetic interference sources around. A testing unit with tri-axial accelerometers, gyroscopes and magnetometers was used, more details is introduced in Section 6.3.1. The unit was placed on a wooden rotation disk, which can rotate horizontally on a big wooden table as shown in Figure 4-2. Six reference angle points are surveyed at every 60 degrees.

The testing unit and underlying orientation definition follow right-forward-up conventions for X, Y, and Z axis, as illustrated below. At the beginning of the data logging, three rounds of figure-8 calibrations were done first on the rotation disk for a better initial magnetometer calibration. Then the unit was rigidly placed in five different attitudes, denoted as Test 1 to Test5 in next section. The rotation disk experienced a complete 360 degree rotation at a slow speed rotating

clockwise. It stops at each marked 60 degree interval with some static periods in between each rotation.

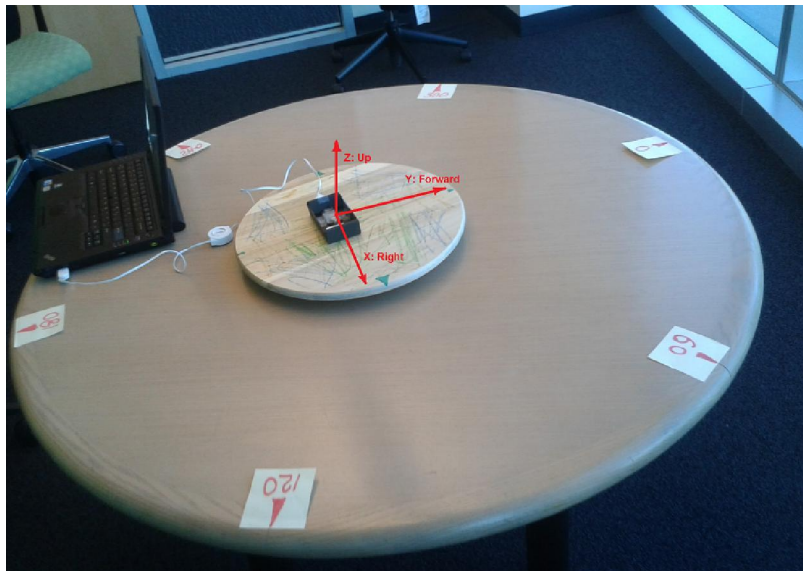


Figure 4-2 Rotation test setup

4.2.2 Rotation Test Result

Attitude Test 1: Pitch: 0° , Roll: 0° , Heading: 0° , rotating horizontally about the Z axis.

Note initial attitudes and intermediate heading stops are roughly estimated within 10 degrees of error; the Right-Forward-Up convention was used to define Euler angles. The attitude fusion results of heading, pitch and roll are plotted in Figure 4-3. The solution from gyro-only based, magnetometer plus accelerometer based, and nine-axis EKF fusion are compared below.

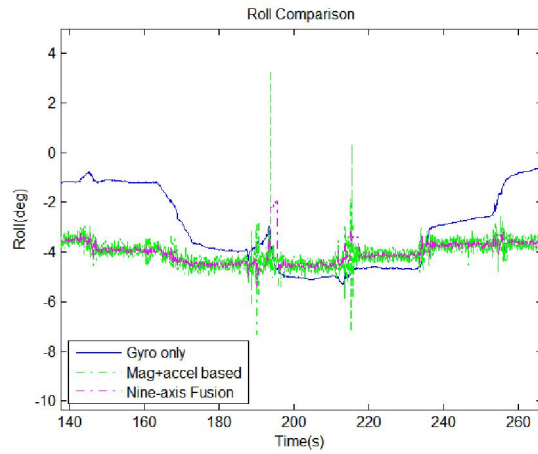
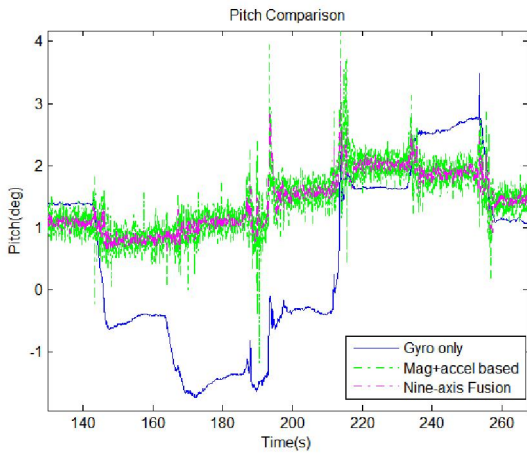
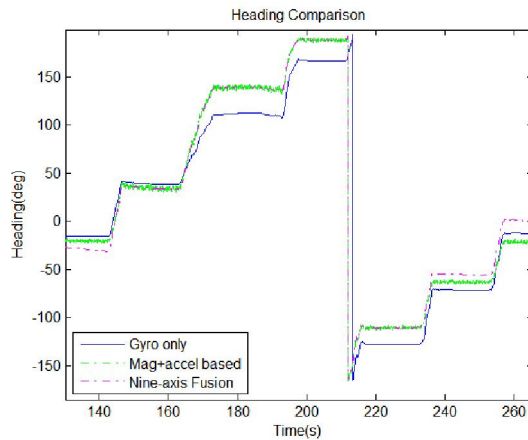


Figure 4-3 Rotation test results of attitude Test1

Attitude Test 2: Pitch: 0°, Roll: 90°, Heading: 0°, rotating about the X axis.

Test2 is similar to Test1 except having a different initial attitude. The initial position and fusion attitude results of gyro-only based, magnetometer plus accelerometer based, and nine-axis EKF fusion are given in Figure 4-4 below.

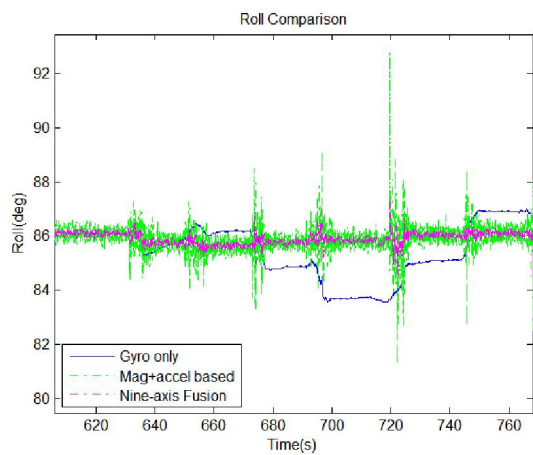
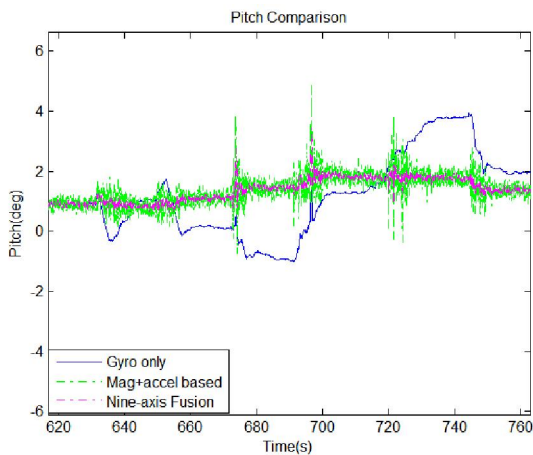
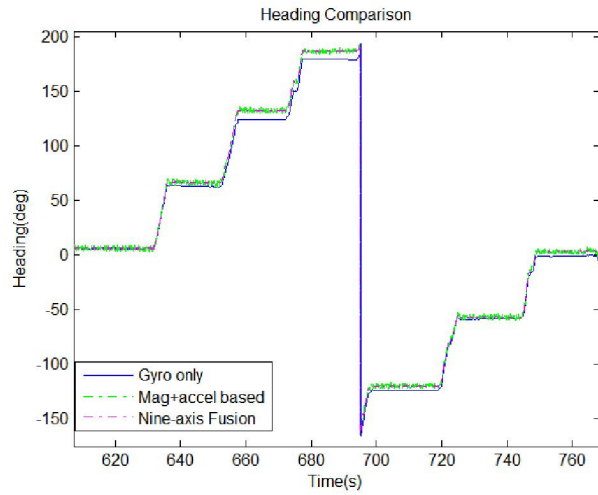


Figure 4-4 Rotation test results of attitude Test2

From Test 1 and Test 2 above, we can see that the fusion engine can output heading, pitch, and roll of the devices properly with three input combinations: the gyro-only solution is smooth but suffers bias errors that drift over time. The magnetometer + accelerometer solution does not drift, but exhibits much noisier output, mostly because the rotation motion has an impact on the accelerometer-based estimation of pitch and roll. Magnetic interference during the rotation also

impacts the heading. The nine-axis fusion EKF takes advantage of the above two solutions and presents the best overall performance.

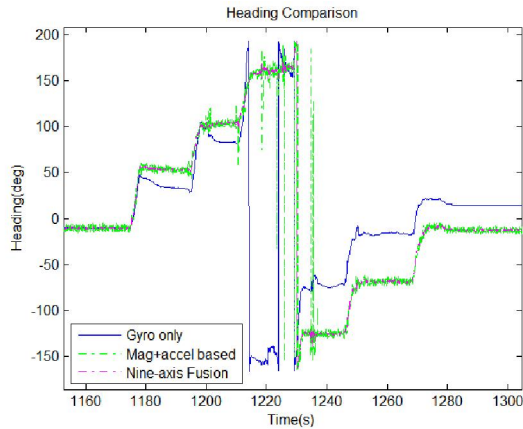
Attitude Test 3: Pitch: 90°, Roll: 0°, Heading: 0°, rotate about -Y axis.

The attitude results of gyro-only based, magnetometer plus accelerometer based, and nine-axis EKF fusion are given in Figure 4-5 below.

Note this is a special case where singularity (gimble lock) exists. When substituting Pitch = 90 degrees into the DCM equation, it is observed that the rotation matrix is degenerated into:

$$C_n^b = \begin{pmatrix} \cos R \cos H - \sin P \sin R \sin H & \cos R \sin H + \sin R \sin P \cos H & -\cos P \sin R \\ -\cos P \sin H & \cos P \cos H & \sin P \\ \sin R \cos H + \sin P \cos R \sin H & \sin R \sin H - \sin P \cos R \cos H & \cos P \cos R \end{pmatrix}$$

$$= \begin{pmatrix} \cos (R + H) & \sin (R + H) & 0 \\ 0 & 0 & 1 \\ \sin (R + H) & -\cos (R + H) & 0 \end{pmatrix} \quad (4.50)$$



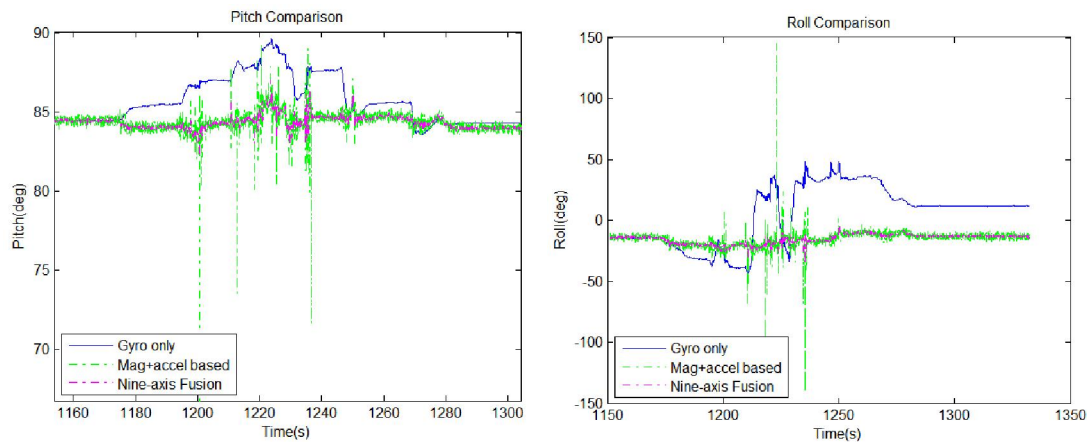


Figure 4-5 Rotation test results of attitude Test3

Clearly, changing the values of R and H in the above matrix has the same effects. Therefore, with the pitch angle fixed to 90 degrees, only one degree of freedom (corresponding to the sum of R and H) remains.

That explains why the gyro-only solution showed large heading roll errors in the test above. 6-axis and 9-axis fusion results are more stable because the roll was better taken into account from the accelerometer-based leveling.

The following Test4 and Test5 rotate along an arbitrary axis with a tilted initial attitude. The orientation and test results are given in Figure 4-6 and Figure 4-7 below respectively.

Attitude Test 4: Pitch: 0°, Roll: 40°, Heading: 0°, rotate about a tilted rotation axis.

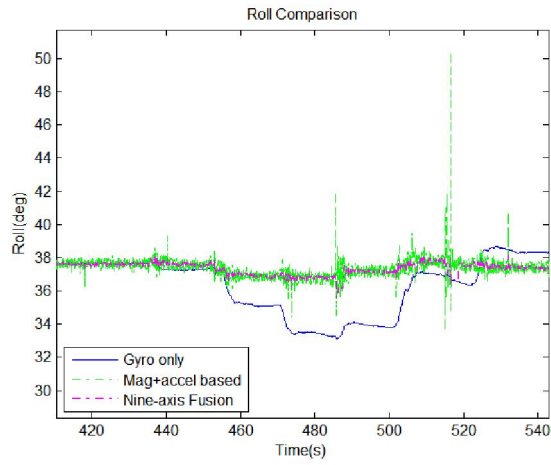
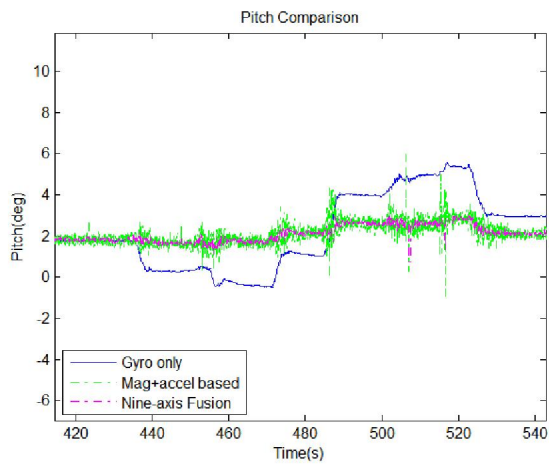
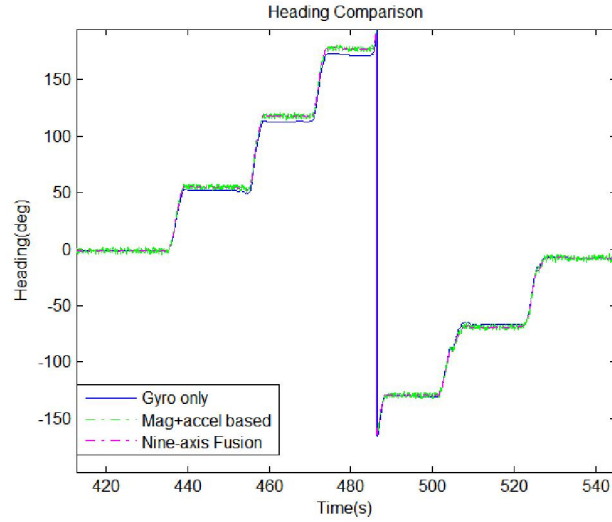


Figure 4-6 Rotation test results of attitude Test4

Attitude Test 5: Pitch: 45°, Roll: 0°, Heading: 0°, rotate about a tilted rotation axis.

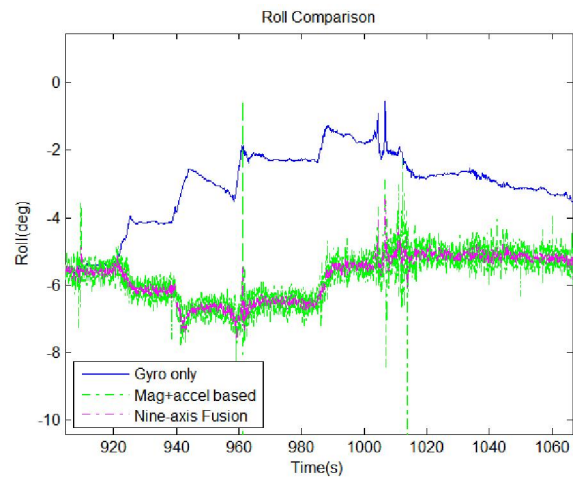
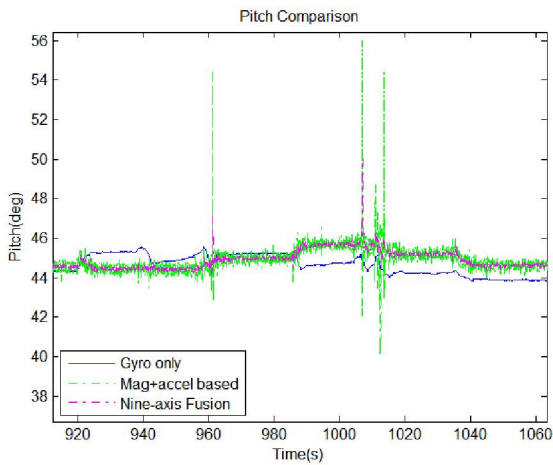
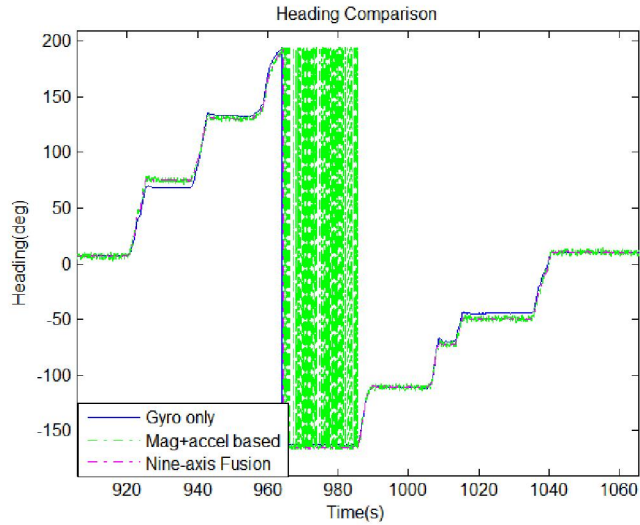


Figure 4-7 Rotation test results of attitude Test5

From the tests above, we can see the pitch and roll are more stable because of the accelerometers measurement update. The heading accuracy is of more concern because it is will be impacted by the magnetometers quality thus is more subject to disturbances. The RMS of the heading error using three orientation filters is summarized in Table4-1 below. The reference value is based on

the six surveyed angles and then compare against the orientation filter output when the device is in static.

From the results, we can see gyro-only solution is more vulnerable to error drift after orientation change; magnetometers can provide heading correction so the mean value is more accurate although exhibit jittery output from the ambient disturbances; finally the nine-axis fusion has the advantage of complimentary sensors characteristics thus showed the best overall performance. It shows the attitude filter introduced in this chapter serves as an effective fusion engine to output heading, pitch, and roll of the devices properly for an arbitrary rotation axis. The performance of the device's orientation is the most critical factor in achieving the overall positioning accuracy in the PNS device.

Table 4-1 Heading error comparison

EKF Configuration	RMS Test1 (deg)	RMS Test2 (deg)	RMS Test3 (deg)	RMS Test4 (deg)	RMS Test5 (deg)
Gyro only	18	8.8	23	6.5	7.1
A+ M EKF	5.5	3.7	7.4	3.7	3.6
A+G+M EKF	2.4	2.1	5.9	2.8	2.7

Chapter Five: **HYBRID PERSONAL NAVIGATION ALGORITHMS**

A personal navigation system provides estimation of its position, velocity, and attitude with respect to a navigation frame as defined in Chapter 4. This chapter discusses the key algorithms involved in this estimation. The chapter will cover the following development:

- A Pedestrian Dead Reckoning (PDR) method is developed to determine horizontal position.
- Three Extended Kalman Filter (EKF) configurations are discussed to integrate MEMS sensors-based PDR positions with GPS.
- A systematic observability analysis is introduced next to select the estimated states in the Kalman filter.
- To determine vertical position, the integration of a barometer and GPS height measurements is given.
- Wi-Fi indoor positioning is presented as an additional aiding source for indoor positioning.

5.1 Pedestrian Dead Reckoning Mechanization

The mechanization of a navigation device describes the physical arrangement of the sensors relative to the human body then transforms sensor measurements to the navigation coordinate frame. The mechanization can be implemented by two approaches: direct INS mechanization and indirect model-based PDR. The conventional way of INS mechanization derives position based on integrating accelerometer data first to get velocity, and then integrates velocity to get displacement. However, as consumer devices usually adapt low-cost MEMS, accurate position is difficult to obtain with this method due to noisy MEMS sensor errors. Besides, most navigation

devices are not rigidly connected to the body in motion, such as when a person holds a smartphone, as additional orientation changes and vibration of the device occur during the walking, which contributes more error to the derived position.

Arguably, using consumer quality MEMS sensors, the PDR estimation method outperforms the conventional INS mechanizations with better robustness. By exploiting the kinematics of the human gait with the traveled distance and heading information, this method is less sensitive to sensor errors and orientation relative to the user. A PDR system uses a platform's initial position and velocity and then updates its new position based on measured or estimated velocity, heading, and elapsed time. Instead of deriving positions from velocity, positions can be predicted by step detection and stride length estimation. Once heading is known, current position can be derived by traveling stride length along the direction of the motion from previous position.

5.1.1 Step Detection

A person's walking follows a distinguishably repetitive pattern in acceleration. Referring to [Kwakkel 2008], the human gait cycle analysis is given below in Figure 5-1.

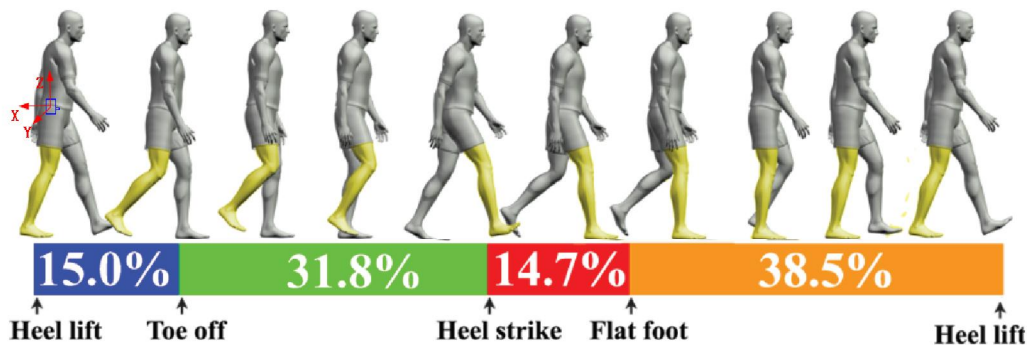


Figure 5-1 Gait cycle analysis

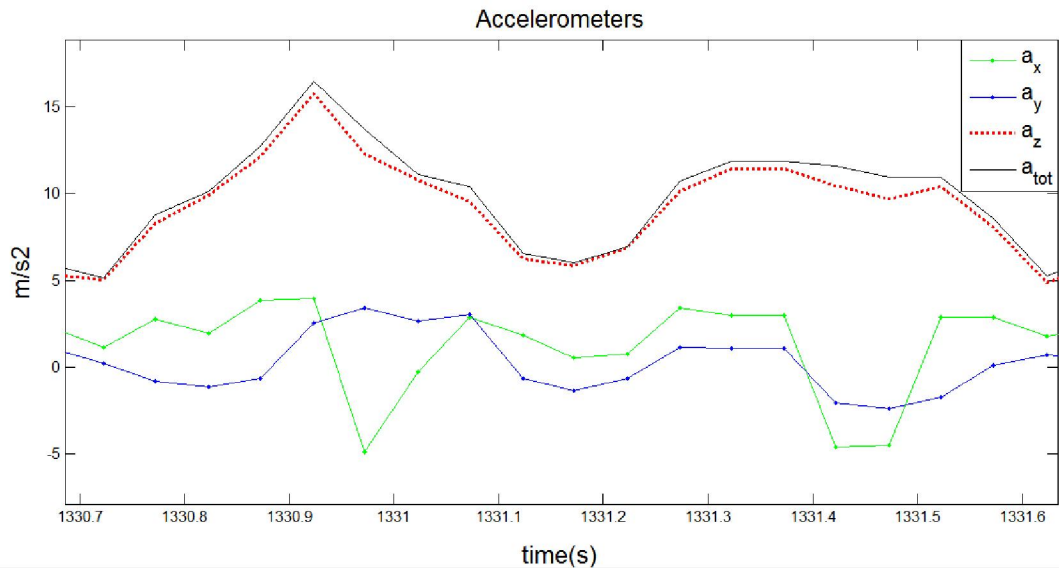


Figure 5-2 Accelerometer signals during a gait cycle

The accelerometer signals of one complete gait cycle were presented accordingly, as illustrated in Figure 5-2. Starting with the right foot lifting, the vertical Z axis experiences a large peak followed by a bottom indicating the heel strike. Then, after a short period of the foot flat on the ground with relatively static accelerometer signals, the left foot cycle begins a similar up and down pattern. The vertical acceleration appears most obvious in variation when the foot goes up and down compared to forward and right side movement. In practical step detection, the total amplitude of three-axis accelerometers, a_{tot} , can be used for step detection. From Figure 5-2 the variation of a_{tot} is close to a_z , and the algorithm has the advantage of being less sensitive to the device orientation.

Step detection algorithms can be developed based on the time or frequency feature of the accelerometer signal using algorithms such as peak detection, zero crossing detection, and fast Fourier transform [Godha 2006]. One robust method applied the moving accelerometer variance over a sliding window of ‘n’ samples, which is then checked periodically against a certain

threshold variance. When the computed variance crosses the threshold value, a step is declared. One advantage to use variance as detection input is to remove the algorithm sensitivity to sensor bias. Usually for the data sampling rate (f_s) of 20-50 Hz, an appropriate window size is chosen to be $n = f_s/2$.

Some improvements can be made by giving some constraints for the detection to increase the robustness of the detection. False peaks can be eliminated by checking if the time between the two consecutive steps is more than a minimum interval threshold in time. For example, any declared step with interval less than 0.3 second is rejected because in normal walking, the step frequency is rarely higher than 3.3 Hz. In addition, the step detection variance and interval threshold can be set adaptively for walking versus running. When people move faster at a running speed, a higher variance threshold can be applied. For example, at normal walking speed, a variance threshold is 1 m/s^2 . In running, it switches to 2 m/s^2 . Figure 5-3 below shows an example of step detection results.

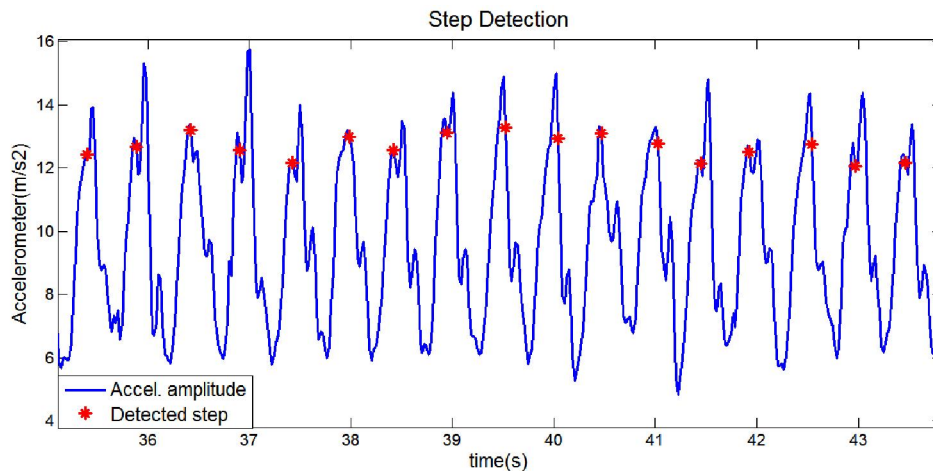


Figure 5-3 Step detection

5.1.2 Stride Length Estimation

Stride length is defined as the distance traveled between two consecutive heel impacts on the ground. Ideally integrating the forward accelerometer signal twice from one footfall to another can deduce the step length. In practice, this approach will be very inaccurate because of random alignment and bias drift of the accelerometers.

Instead, a parametric model of stride length is used to build a simple relationship between stride length and some detected signal features. Two candidate features are investigated: the magnitude of forward acceleration defined as the standard deviation of the accelerometer signal, and the step frequency f_k , which is the walking cadence frequency from time t_{k-1} to t_k for the two consecutive steps detected.

$$f_k = \frac{1}{t_k - t_{k-1}} \quad (5.1)$$

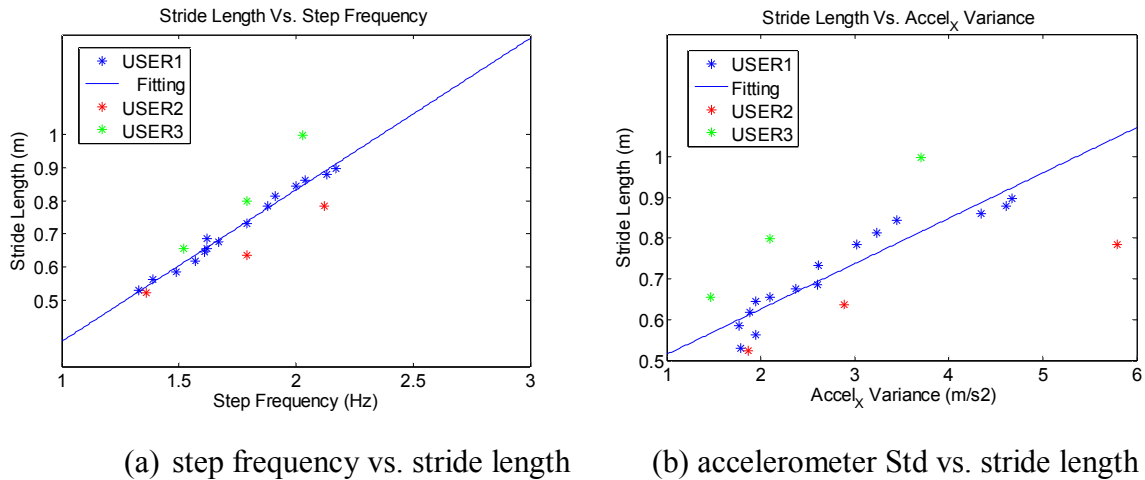


Figure 5-4 Linear regression of stride length estimation

Figure 5-4 (a) shows a plot between step frequency and stride length for three different users walking at different speeds. Figure 5-4 (b), in comparison, shows another approach using the standard deviation of forward-accelerometer to derive stride length. The first approach outperforms the second with better linearity in that the average residue error of the stride length estimation is 0.003 m, as opposed to 0.022 m in the second approach.

A simple linear model is therefore established relating stride length SL_k to the step frequency f_k .

$$SL_k = \begin{cases} 0.5, & f_k < 1.25 \\ 0.46 \times f_k - 0.081, & 1.25 \leq f_k < 3 \\ 0.9, & f_k \geq 3, \end{cases} \quad (5.2)$$

In practice, the human gait changes from person to person, walking terrain, and other various conditions. In order to account for this variation, the stride length can be augmented with a variable component that represents the residual variation in a user's stride. The component can be modeled as a stride length bias error as Gaussian noise or a Gauss Markov process. The correction can be estimated in the navigation Kalman filter.

5.1.3 Pedestrian Dead Reckoning

Dead reckoning (DR) is the determination of a new position from the knowledge of a previous known position utilizing current distance and heading information. As such, DR consists of three important components:

- The prior absolute position of the user at time t-1, (E_{t-1}, N_{t-1})
- The distance traveled by the user since time t-1, $(\hat{s}_{[t-1, t]})$
- The user's heading (ψ) since time t-1

The coordinates (E_t , N_t) of a new position with respect to a previously known position (E_{t-1} , N_{t-1}) can be computed as follows:

$$\begin{aligned} E_t &= E_{t-1} + \hat{s}_{[t-1,t]} \sin \psi_{t-1} \\ N_t &= N_{t-1} + \hat{s}_{[t-1,t]} \cos \psi_{t-1} \end{aligned} \quad (5.3)$$

Eq. (5.3) is the foundation of PDR system, which continuously propagates position based on the detected step at time t , stride length $\hat{s}_{[t-1,t]}$ and heading ψ , as depicted in Figure 5-5.

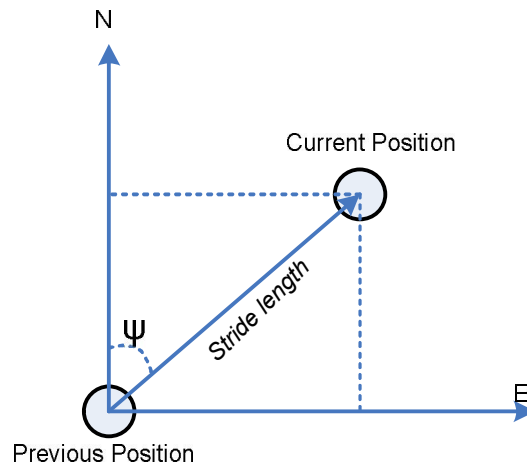


Figure 5-5 Dead reckoning concept

As illustrated above, heading is a key element in PDR; it can be obtained from the 9-DOF sensor fusion of tri-axial accelerometers, gyroscopes and magnetometers, as introduced in Chapter 4.

From above, the processing of PDR includes three essential components:

- Step detection
- Stride length estimation
- Heading determination

GPS or wireless positioning receivers provide an absolute position to start with; then the accelerometer data is utilized for the detection of steps and estimation of stride length; then the fusion of magnetometers, gyroscopes, and accelerometers determines the device's heading, as discussed in Chapter 4.

5.2 Kalman Filter Integration and State Selection

5.2.1 Kalman Filter Integration

Kalman filter is the engine to estimate the state of discrete-time controlled process governed by linear stochastic differential equations [Grewal 2008]. Figure 5-6 illustrates the typical procedure of a KF. The iteration starts with a prediction of the error states and covariance based on initial condition and apriori information of the system, and then the measured inputs, Z_k , are fused with the results from the predicted state as an update stage. During this fusion, the Z_k measurements are given appropriate weight, denoted as Kalman Gain K_k which is determined by the covariance matrix of the system noise, Q , and the covariance matrix of the measurement noise, R . In Kalman filters, state selections, process modeling, and measurement modeling are all crucial to the estimation design, which are reflected by the state transition matrix F , design matrix H , and system noise W , respectively.

The conventional Kalman Filter can estimate the state of discrete-time controlled processes governed by linear stochastic differential equations. Since attitude estimation has nonlinear system equations, an Extended Kalman Filter (EKF) is used to linearize the process about the current state.

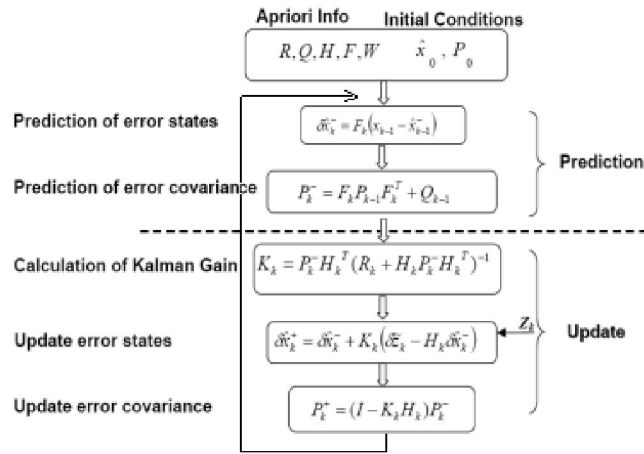


Figure 5-6 Kalman filtering procedure

Optimal integration of the PDR and GPS are essential for a good positioning solution; this section discusses the Kalman Filter design. Several considerations are taken into account for the state selection in the Kalman filter. First of all, the states must be complete enough to describe the kinematics of pedestrian navigation. Next, the states should be able to correct the errors in the sensor measurement. Observability for pedestrian navigation is another important consideration to be introduced in Section 5.3, as the user's walking speed and rotation rate is not high enough to accurately determine heading, in contrast with vehicle navigation scenarios. Finally, the simplicity of computation and economical configurations are preferable in real-time navigation [Syed 2009].

For an effective EKF implementation, careful considerations are taken into account. Chapter 4 presented a complete 3/6/9-axis attitude fusion scheme. This chapter further analyzes a partial sensor solution for pedestrian navigation in a horizontal plane, where three configurations are selected for the heading estimation:

- Heading computation from magnetometers with less drift error under regular magnetic fields.
- Heading computation by integration of single heading gyroscope signals in the presence of local magnetic anomalies.
- Heading computation by integration of three-axis gyroscope signals in the presence of local magnetic anomalies.

The next section will introduce how to apply the above three heading methods in the system error models for GPS/PDR integration.

5.2.2 Pedestrian Navigation System Error Models

The system error models describe the behavior of the sensor error propagation. They also include the solution of the navigation equations for estimating the user's position. The system mechanization based on PDR is introduced in Section 5.1. In pedestrian navigation, the six-axis sensors configuration, either tri-axial accelerometers plus magnetometer, or tri-axial accelerometers plus gyro, is compulsory for navigation scenarios with significant roll, pitch, and azimuth changes. However, for most pedestrian navigation, the operation is mainly constrained to two dimensions and low dynamics. So the easting and northing of the positioning solution can be derived from PDR, independent of height information coming from the barometer or GPS data. In vertical dimension, as the barometer provides a direct measurement of the height, it has direct observability for error correction. Consequently, the Kalman filter system analysis can be simplified considering horizontal positioning errors, heading error, and sensor errors only. This section first develops system models by estimating errors with only heading gyro,

magnetometers, and a GPS receiver measurement. The EKF implementations for pedestrian navigation are summarized as configurations in Table 5-1 below.

Table 5-1 Three EKF configurations for PDR/GPS integration

<i>Cfg.</i>	<i>EKF</i>	<i>State Selection</i>	<i>Measurement</i>
1	6-state Mag	E, N, ψ_m , SL_b , Mx_b , My_b	GPS lat, lon, heading from mag.
2	6-state Gyro	E, N, ψ_g , g_b , g_{sf} , SL_b	GPS lat, lon, heading from heading gyro
3	9-state Gyro	E, N, Δp , Δr , $\Delta \theta$, g_{bx} , g_{by} , g_{bz} , SL_b	GPS lat, lon, heading from 3D- gyros

Three heading methodologies are available to determine the heading angle ψ in PDR Eq.(5.3). In the first configuration, heading is derived from magnetometers, as it has less drift error for regular magnetic fields such as outdoor areas, as shown in Equation (5.4).

$$\psi_m = \arctan\left(\frac{\overline{My} - My_b}{\overline{Mx} - Mx_b}\right) \quad (5.4)$$

Where $\overline{M_x}$ and $\overline{M_y}$ are the average magnetometer readings during one step and Mx_{bias} and My_{bias} are correction for the magnetometers biases. In Table 5-2, six states are selected for magnetometer PDR/GPS integration, where E and N are the Easting and Northing positions of the user, θ_{bias} is the correction for the heading, SL_{bias} is the stride length correction from the linear model in Equation(5.2), and Mx_{bias} and My_{bias} for magnetometers error correction. As this configuration uses a magnetometer, it is applicable for open outdoor environments with minimum magnetic anomalies. Another assumption for this configuration is that the PNS unit is well mounted and the user is walking on level ground with negligible pitch and roll angles. For

this configuration, GPS provides correction updates in terms of latitude and longitude while the magnetometer provides heading.

Table 5-2 EKF based magnetometer DR/GPS integration (6-state)

Application Scenarios	<ul style="list-style-type: none"> ▪ Outdoor open environment ▪ Assumption: level ground
State Selection	$E, N, \theta, SL_{bias}, M_{bx}, M_{by}$
Process Model	$SL(k+1) = f(\Delta t_k) + SL_{bias}(k)$ $E(k+1) = E(k) + SL(k) \times \sin(\theta(k)) + W_E$ $N(k+1) = N(k) + SL(k) \times \cos(\theta(k)) + W_N$
Measurement	<p>GPS Lat, Lon. Heading derived from Magnetometers</p> $\theta = \arctan\left(\frac{M_y}{M_x}\right)$
Sensors Model	$M_{bx}(k+1) = e^{-\beta\Delta t_k} \times M_{bx}(k) + W_{Mbx}$ $M_{by}(k+1) = e^{-\beta\Delta t_k} \times M_{by}(k) + W_{Mby}$ $M_x(k+1) = \overline{M_x} + M_{bx}(k)$ $M_y(k+1) = \overline{M_y} + M_{by}(k)$

The EKF estimates both navigation error states and sensor error states. To include the sensor error states in the state vector, the sensor errors must be modeled. Stochastic models are used to represent the error characteristic of these sensors, as discussed in Chapter 3. The selection of an appropriate error model in the EKF guarantees a better solution by computing the navigation states that are closer to the true values in the prediction stage.

The EKF requires the error states to follow normal distribution and therefore, in the EKF design, it was assumed that all the error states are random and follow a normal distribution $N(0, \sigma_n^2)$.

The EKF results will not be optimal if this assumption is not valid. The choice of the error model

is dependent on the operation time, sensor performance, and working environment (Shin 2005).

The sensor bias is modeled as a first-order Gauss-Markov process with time constant β . β was obtained from static lab autocorrelation tests for this study but it can also be chosen empirically.

Finally, system noises, W , are added with a Gaussian distribution.

Now, consider the case where magnetometer data is corrupted with magnetic anomalies. Thus an alternative system model can be expanded to complete 3D sensors' configurations. The second configuration includes 9-state filter utilizing tri-axial gyroscopes to determine the change of heading, pitch, and roll along with GPS derived positions. From Table 5-1, the 9 states in EKF are the correction for the pitch (Δp), roll (Δr) and heading ($\Delta \psi$), the correction for the tri-axial gyro biases (g_{bx} , g_{by} , g_{bz}), and the stride length correction (SL_b). For the attitude error differential equation, it can be simplified as:

$$\dot{\hat{\epsilon}}^n = -C_b^n \delta \omega_{ib}^b \quad (5.5)$$

Where C_b^n is the DCM from body frame to navigation frame and $\delta \omega_{ib}^b$ is the angular-rate error vector in body frame, which is dominated by the bias vector $[g_{bx} \ g_{by} \ g_{bz}]^T$.

In this case, the heading computation from tri-axial gyroscopes is summarized in Table 5-3. Here tri-axial gyroscopes are utilized to determine the change of heading, pitch, and roll. To avoid singularities in the attitude mechanizations, quaternions are used [Sabatini 2006]. For this EKF implementation, the measurements are from GPS positions and three orthogonal gyros. $\overline{\omega(k)}$ is the average gyro output during the detected step k . Gyroscope biases were modeled as a first-order Gaussian Markov process in the EKF. In addition, the angular random walk and bias instability noises are added to the process models. These parameters were calculated from the static dataset given in Section 3.4.

Table 5-3 EKF based gyro DR/GPS integration (9-state)

Application Scenarios	Indoor/outdoor No zero pitch roll assumption
State Selection	$E, N, \Delta P, \Delta r, \Delta \theta, \mathbf{g}_{bx}, \mathbf{g}_{by}, \mathbf{g}_{bz}, \text{SL}_{\text{bias}}$
Process Model	$E(k+1) = E(k) + SL(k) \times \sin(\theta(k)) + W_E$ $N(k+1) = N(k) + SL(k) \times \cos(\theta(k)) + W_N$ $\dot{q}_b^n = \frac{1}{2} q_b^n \otimes [\omega_{ib}^b]_q$
Measurement	GPS Lat, Lon. Heading from gyroscope
Sensors Model	$\omega_{ib}^b(k+1) = \bar{\omega}(k) + [\mathbf{g}_{bx}(k), \mathbf{g}_{by}(k), \mathbf{g}_{bz}(k)]^T + W_\omega$ $\mathbf{g}_b(k+1) = e^{-\beta \Delta t_k} \times \mathbf{g}_b(k) + W_{\text{Mbias}}$

Observability of the Kalman filter states may limit the accuracy to estimate the pedestrian heading [Cho 2006]. As a result, magnetometer heading is used, which is not always reliable enough to assist the gyro-based attitude. Proper detection of zero velocity periods ensures reliable roll and pitch estimation from accelerometer readings. However, in this belt-mounted configuration, detection of zero velocity periods is quite challenging and cannot be fully trusted. As a result, it is beneficial to remove weak observable states. Therefore, the above 9-states Gyro DR/GPS integration can be reduced to 6-states as shown in Table 5-4.

In this configuration, the heading is derived by the integration of heading gyro, as shown in Equation (5.6).

$$\psi_g = \int_{t_0}^{t_1} \mathbf{g}_{sf} \times (\omega(t) - \mathbf{g}_b) dt \quad (5.6)$$

Where $\omega(t)$ is the heading gyro measurement.

Among all the gyro sensor errors such as bias, scale factor errors, and alignment error, bias g_b is most unpredictable and dominant in low-grade sensors and is thus included as a state to estimate. The gyro sensors errors include the contribution of bias error, g_b , and scale factor error, g_{sf} . Both of these errors are modeled as first-order Gaussian Markov processes in the EKF as given in Equation (5.7), where β_1 and β_2 are the time constant of the gyro bias and scale factor drift and Δt_k is the interval between detected steps.

$$\begin{aligned} g_b(k+1) &= e^{-\beta_1 \Delta t_k} \times g_b(k) + W_{g_b} \\ g_{sf}(k+1) &= e^{-\beta_2 \Delta t_k} \times g_{sf}(k) + W_{g_{sf}} \end{aligned} \quad (5.7)$$

Table 5-4 EKF based gyro DR/GPS integration (6-state)

Application Scenarios	<ul style="list-style-type: none"> ▪ Outdoor open environment ▪ Assumption: level ground
State Selection	$E, N, \theta, g_b, g_{sf}, SL_{bias}$
Process Model	$SL(k+1) = f(\Delta t_k) + SL_{bias}(k)$ $E(k+1) = E(k) + SL(k) \times \sin(\theta(k)) + W_E$ $N(k+1) = N(k) + SL(k) \times \cos(\theta(k)) + W_N$
Measurement	GPS Lat, Lon. Heading derived from Gyroscope $\psi_G = \int_{t_0}^{t_1} \omega(t) dt$
Sensors Model	$g_b(k+1) = e^{-\beta_1 \Delta t_k} \times g_b(k) + W_{g_{bias}}$ $g_{sf}(k+1) = e^{-\beta_2 \Delta t_k} \times g_{sf}(k) + W_{g_{sf}}$ $\omega_{ib}^b(k+1) = \bar{\omega}(k)(1 + g_{sf}(k)) + g_b(k) + W_\omega$

Table 5-4 shows the configuration where the attitude is simplified to heading only representation; it applies to most 2D navigation cases. Furthermore, to account for the nonlinearity of the gyro, another parameter, the scale factor g_{sf} is included in the estimation. The

scale factor is also modeled as a first-order Gauss-Markov process. The above simplification of estimated states enables a reduced multi-sensor configuration for 2D pedestrian navigation.

Furthermore, the resulting simplified computation for position which is an additional advantage for application in real-time navigation scenarios.

From Equations (5.4)-(5.7), the dynamic matrix F can be constructed for each Kalman filter configuration accordingly. The measurement matrix H is

$$H = [I_2 \ 0_{2 \times n-2}] \quad (5.8)$$

Where n is the number of states in each configuration.

5.2.3 Integrity Monitoring

In a multi-sensor integrated system, some inputs can occasionally produce output errors much larger than standard uncertainty bounds, due to hardware or software failures. Integrity monitoring detects these faults and protects the accuracy of the overall navigation solution [Groves 2008]. On the sensor input level, Fault Detection and Isolation (FDI) can identify the faults or extreme errors that fall outside of standard measurement ranges, and isolate them from the quality data. As a result, the bad data doesn't affect accuracy.

Two types of techniques are applied for fault detection in this thesis. First, a range sanity check can be used to reject outliers and smooth out the measurement. This method is straightforward and simple to use to reject erroneous data. For example, while walking a user's speed cannot be too fast, so whenever a position is recorded that implies an unrealistically fast rate of movement, it can be thrown out.

The second method is measurement innovations testing, which is widely used in Kalman filters as reliability testing to remove bad data. This is helpful especially when GPS or Wi-Fi solutions

have multipath near buildings but have standard deviations that are still relatively small, thus compromising the measurement noise matrix R 's ability to reflect the true accuracy. In Kalman filters, when we assume the process and measurement models are zero-mean, Gaussian white noise, the innovation sequence defined in Equation (5.9) will also be zero-mean with a white Gaussian distribution. Thus we can do single blunder detection from an innovation sequence on an observation-by-observation basis [Groves, 2008]. The innovation sequence is obtained as:

$$\delta z = z_k - h(\hat{x}_k^-) \quad (5.9)$$

Where δz is the innovation sequence,

z_k is the Wi-Fi position measurement,

$h(\hat{x}_k^-)$ is the position prediction.

The covariance of the innovations C_k^- comprises the sum of the measurement noise covariance and the error covariance of the state estimates transformed into the measurement space as Equation (5.10).

$$C_k^- = H_k P_k^- H_k^T + R_k \quad (5.10)$$

Where H_k is measurement design matrix

P_k is the covariance matrix for the estimated states

R_k is the covariance matrix for the measurement noise

Innovations of the above covariance matrix are normalized in Equation (6.3), where y has a zero-mean, unit-variance Normal distribution, and consequently is used as the statistical test variable. When it exceeds the statistical confidence level threshold, the result is determined to be the result of faulty measurements and is rejected.

$$y_{k,j}^- = \frac{\delta z_{k,j}^-}{\sqrt{C_k^-(j,j)}} \quad (5.11)$$

5.3 Observability Analysis and State Selection for PNS

Observability is the ability to determine the value of the states given a set of measurements [Zhang 2004]. In this section, observability analysis is performed using the above Kalman filter configurations for pedestrian navigation. We define the observability matrix as O . If $\text{Rank}(O) = n$, where n is number of the estimated states, then the system is observable. However, this observability analysis suffers two limitations: assuming time is invariant and failing to provide complete system information. Firstly, it assumes the system is time-invariant. Yet in many cases when the system has dynamics this assumption is no longer valid. Moreover, such analysis can only qualitatively judge the observability and fail to provide complete system information such as the degree of observability and which state in the estimation is not observable.

To overcome the first limitation, A Piece-Wise Constant Systems (PWCS) approximation [G-M 1992-1] is introduced. It assumes the state transition matrix F and the measurement matrix H are constant within each piece or segment; but F and H matrices can vary from segment to segment. In this way, a Total Observability Matrix (TOM) can be formed. To further quantify the degree of observability, a Singular Value Decomposition (SVD) approach can be applied. A large singular value will lead to higher observable degree [Wan 1998]. The maximum in the right singular vector shows the state with the corresponding singular value; and similarly, the minimum vector corresponds to the weakest observable state in the system.

The goal of the observability study here is to determine the most efficient EKF design for personal navigation systems so that weakly observable or unobservable states in the estimation

can be eliminated. As mentioned above, the objective is to find a method to provide details about the degree of observability of different system configurations. Furthermore, the objective also aims to provide information to the system designer regarding the required maneuver to augment state estimation.

5.3.1 Analysis of Observability and Observable Degree

Observability is the ability to determine the value of the states x_k given a set of measurements z_k as shown below.

$$\begin{aligned} x_{k+1} &= F_j x_k \\ z_k &= H_j x_k \end{aligned} \quad (5.12)$$

Where F_j and H_j are the transition matrix and measurement matrix of the homogeneous system in Equation (5.12), respectively. Thus we can define the Observability Matrix O as [Grewal 2008]:

$$O = [H^T \quad F^T H^T \quad \dots \quad (F^T)^{n-1} H^T] \quad (5.13)$$

If $\text{Rank}(O) = n$ then the system is observable. This observability analysis suffers two limitations: First, it assumes the system is time-invariant. However, in many cases when the system has dynamics, it is no longer valid. Moreover, such analysis can only qualitatively judge the observability and fail to provide complete system information, like the degree of observability and which state in the estimation is not observable.

As illustrated in Figure 5-6[G-M 1992-1], we assume within each segment j , the state transition F_j and measurement matrix H_j are constant; but they change from segment to segment.

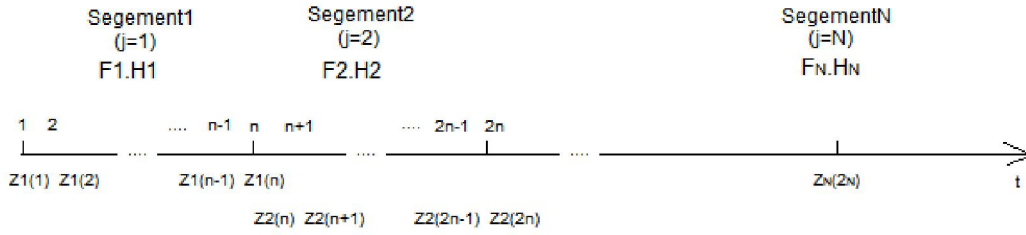


Figure 5-6 Measurement sequence in PWCS approximation

In this way, a Total Observability Matrix (TOM) $Q_T(r)$ can be formed as

$$Q_T(r) = \begin{bmatrix} Q_1 \\ Q_2 F_1^{n-1} \\ \dots \\ Q_r F_{r-1}^{n-1} F_{r-2}^{n-1} \dots F_1^{n-1} \end{bmatrix} \quad (5.14)$$

Where:

r is the number of segments

n is the number of states

The observability matrix of each segment j , Q_j , is defined as:

$$Q_j = [H_j^T \mid (H_j F_j)^T \mid \dots \mid (H_j F_j^{n-1})^T]^T \quad (5.15)$$

According to the PWCS theory, when the following null-space relationship in (5.16) holds, then the total observability matrix can be simplified by stripped observability matrix (SOM) Q_S .

$$\text{null}(Q_i) \subset \text{null}(F_i) \quad (1 \leq i \leq r) \quad (5.16)$$

Then Q_T and Q_S have the same rank as:

$$\text{rank}(Q_T(r)) = \text{rank}(Q_S(r)) \quad (5.17)$$

The proof was given in [G-M 1992-2] where the SOM is constructed in Equation (5.18).

Therefore, we can replace the time-varying system by the PWCS without losing the system characteristic behavior.

$$Q_s(r) = \begin{bmatrix} Q_1 \\ Q_2 \\ \dots \\ Q_r \end{bmatrix} \quad (5.18)$$

To further quantify the degree of observability, another approach was introduced in [Ham1983]. The idea is to study the covariance matrix P of the states, if P experiences a large decrease from its initial value P_0 , then the corresponding observability is large. With appropriate normalization of P by congruent transformation using P_0 , it provides some insight into the observability of linear combinations of the states that might otherwise be overlooked with a casual examination of the major-diagonal terms of the P matrix.

The Eigen values and Eigen vectors of the error covariance matrix P give useful information about system observability as follows.

$$Px = \lambda x \quad (5.19)$$

Large Eigen values indicate the poorly observable states. While the best observability is indicated by the smallest Eigen value of P and the corresponding eigenvector gives the "direction" of this highest degree of observability. The merit of the Eigen value approach is that one only has to look at n rather than $n(n+1)/2$ items to gain judgment into the degree of observability, instead of analyzing the whole observability matrix. However, the limitation of this method is observability can only be measured after the Kalman filtering has been applied. Finally, a method based on Singular Value Decomposition (SVD) of the stripped observation matrix P is proposed. The analysis is based upon a null space test of the observability matrices. Each singular value of P is the observability measure for the subspace spanned by the corresponding singular vector [Klema 1980]. Let P be an m -by- n observability matrix with rank r . Then it can be decomposed into two orthogonal matrices U and V such that

$$P = U\Sigma V^T = \sum_{i=1}^r u_i \sigma_i v_i^T \quad (5.20)$$

$$\sigma_1 \geq \sigma_2 \geq \dots \geq \sigma_r \geq 0, \quad P, U, V, \Sigma \in R^{m \times n}$$

Where:

$\Sigma = \text{diag}(\sigma_1, \sigma_2, \dots, \sigma_r, 0, \dots, 0)$ and σ_i are the singular values of P

Columns u_i in U are called left singular vectors of P

Columns v_i in V are called left singular vectors of P

Hence, $U = (u_1, u_2, \dots, u_n)$ and $V = (v_1, v_2, \dots, v_n)$. If P is symmetric and non-negative, then $U = V$, so the left and right singular vectors are the same and they can be simply called singular vectors. Suppose Z is the measurement vector of the dynamic system, X_0 is the vector of initial states of system Equation (5.12), and P is the observable matrix as defined in (5.20). Then:

$$Z = P X_0 = \sum_{i=1}^r (\sigma_i v_i^T X_0 u_i) = \sum_{i=1}^r \sigma_i (v_i^T X_0) u_i \quad (5.21)$$

So we can determine X_0 from the measurement Z as

$$X_0 = P^{-1} Z = (U \Sigma V^T)^{-1} Z = \sum_{i=1}^r \left(\frac{u_i^T y}{\sigma_i} \right) v_i \quad (5.22)$$

If the singular values of P contains r nonzero elements and $m-r$ zeros, then V can be decomposed as $V = [V_1, V_2]$ where $V_1 = [v_1, v_2, \dots, v_r]$, $V_2 = [v_{r+1}, v_{r+2}, \dots, v_m]$. Therefore, the columns of V_1 serve as a basis for the observable subspace. The columns of V_2 are orthogonal to each other and to the columns of V_1 , and serve as a basis for the unobservable subspace. From practical numerical SVD calculation, we can consider those very small singular values as zero, e.g. when they are less than 10^{-6} .

If this measurement vector Z has a constant norm, then the initial state vector X_0 is bounded by an error ellipsoid [Wan 1998].

$$\sum_{i=1}^r (\sigma_i v_i^T X_0 u_i)^2 = |Z|^2 \quad (5.23)$$

Where σ_i^{-1} is equivalent to the axial length of the error ellipsoid.

The smaller the singular value of σ_i , the larger the initial value of X_0 . So the upper bound of X_0 is:

$$|X_0| \leq \frac{|Z|}{\sigma_r}, \sigma_r = \min(\sigma_i) \quad (5.24)$$

Moreover, in order to judge which state corresponds to the each singular value σ_i in SVD, from the right most part in Equation (5.22), the part in the bracket is a scalar, so the maximum of X_0 is determined solely by the maximum element of the right singular vector v_i . Therefore, the k-th largest element of v_i corresponds to the related state in the system.

Table 5-5 summarizes different observability study approaches for the time-variant system as mentioned above. Since the system models in PDR satisfy the PWCS assumption, SOM can be used to substitute TOM to simplify the analysis. As a result, the SVD of the stripped observability matrix is the most effective approach indicating the degree of observability of each state in GPS and multi-sensors integration Kalman filter. Such PWCS approximation only loses negligible accuracy for moderate motions such as human walking. Each singular value of the observability matrix is the observability measure for the subspace spanned by the corresponding singular vector. This method is less sensitive to perturbation due to system modeling errors and numerical computation. Therefore it is adopted in this research.

Table 5-5 Comparison of observability methods for time-variant system

	Rank (Q_{TOM})	Rank (Q_{SOM})	Covariance Eigenvalue	SVD of Q_{SOM}
Pros	- Most precise method	-Simplify TOM	- Direct physical meaning	- provide degree of obs. - Simple to implement
Cons	- No info. On degree of obs. - Hard to analyze	- No info. On degree of obs. - Lose a little accuracy	- Post processing after KF - Sensitive to P0	- Lose a little accuracy
Ref	[Grewal 2008]	[G-M 1992]	[Ham 1983] [Zhang 2004]	[Wan 1998] [Hong 2008]

5.3.2 Observability Analysis Procedure for Pedestrian Navigation System

Applying the observability method above with the three EKF implementations of the PDR as provided in Table 5-2, the implementation details and prototype is introduced in Section 6.1. The procedure of the observability analysis is summarized as follows[Zhao 2011]:

1. Decide on the Kalman filter configurations using different system models
2. Divide the time into segments with different maneuvers
3. Derive the transition matrix F_j and measurement matrix H_j in time segment j
4. Form the stripped observability matrix Q_s
5. Perform rank test, i.e., rank (Q_s)
6. Inspect singular vector of the unobservable state SVD (Q_s)

In the second step, different segment represents various user motions, or maneuver experienced in the system, as state errors can be made observable by maneuvering. A variety of dynamics are obtained by introducing changes in acceleration and angular velocity.

Table 5-6 Observation matrix rank for three EKFs

	Time Segment	Rank(Q_{SOM})
6-state Mag	Heading=const1	6
6-state Gyro	Heading=const1	5
	Heading=const2	5
	Change ω	6
9-state Gyro	Heading=const1	5
	Heading=const2	6
	Change ω_1	7
	Change ω_2	7

Table 5-6 shows the ranks of observation matrix for three different EKF's introduced above. For the 6-state magnetometer model, as can be seen from the table, the heading is fully observable when the user moves only along a straight line with constant heading.

For 6-state gyro EKF, in the first segment, the user moves with a constant heading (const1) which resulted in a rank of 5. As seen in the second row that changing to another constant heading (const2) and this doesn't increase the observability. The system became fully observable with varying rotation rate ω . This can be explained on the basis of the gyro scale factor estimation which is only possible with different rotations.

For the 9-state gyro model, in the first segment, the user moves with a constant heading (const1) which resulted in a rank of 5. As seen in the second row that changing to another constant heading (const2) causes the observable states increase to 6. When the rotation was introduced by setting turning rate to ω_1 , as shown in the third row, the rank becomes 7. However, as seen in the fourth row, further varying the rotation rate to ω_2 cannot lead to a more observable state.

As introduced previously, SVD analysis can further quantify the degree of observability for each estimated state. Figure 5-7 illustrates the right singular vector for each singular value for 6-state

magnetometer Kalman filter. As discussed above, the largest absolute value of each singular vector indicates the corresponding state. The SVD singular values for each state are summarized in Table 5-7; all the states are fully observable with constant heading only. Also, the singular values corresponding to each state are quite large suggesting strong degree of observability. So we can predict if magnetometer data is available, this integration will result in best performances because of the strong observability.

Table 5-7 6-state magnetometer observability matrix SVD

Singular Value	Segment I (constant heading)
Easting	1.6
Northing	0.68
Heading Bias	0.52
Stride Length Bias	3.2
Mx Sensor Bias	0.25
My Sensor Bias	179

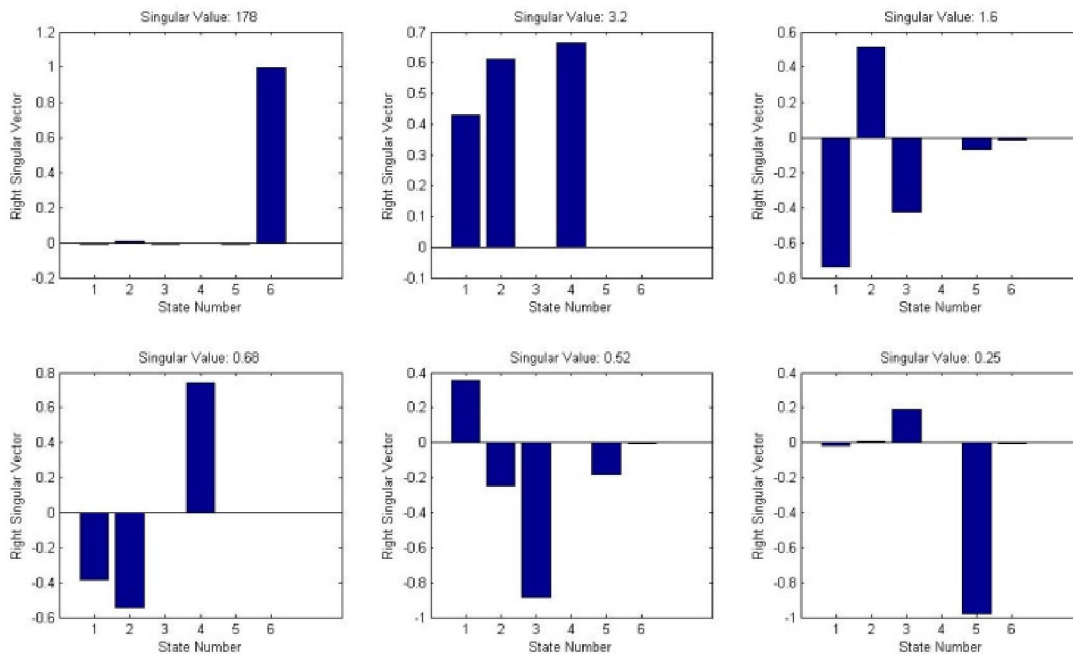


Figure 5-7 SVD for 6-state magnetometer (constant heading)

The singular values of the right singular vector for 6-state gyro Segment I (Straight-line Motion/Constant Rate Rotation) and Segment II (Change Rotation Rate) are plotted in Figure 5-8 and Figure 5-9, respectively. When the singular value is small enough (for example, $<1E-6$), we consider the related state is unobservable. From Table 5-8, we can have a direct quantization of observable degree for each state. When the user is moving with a constant heading, the singular value of gyro scale factor equals $4.6E-18$ thus the state is unobservable. Changing the rotation rate in Segment II can greatly increase this observability to $5.6E-3$. Yet the scale factor state is still relatively weakly observable, compared to other states.

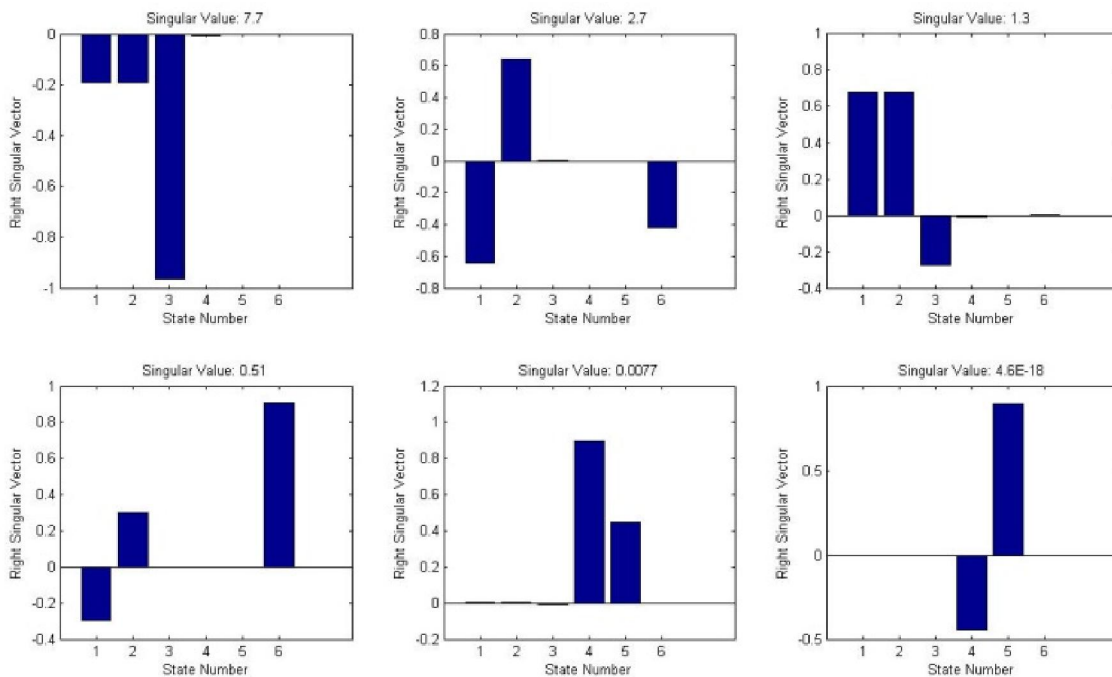


Figure 5-8 SVD for 6-state gyro (constant heading)

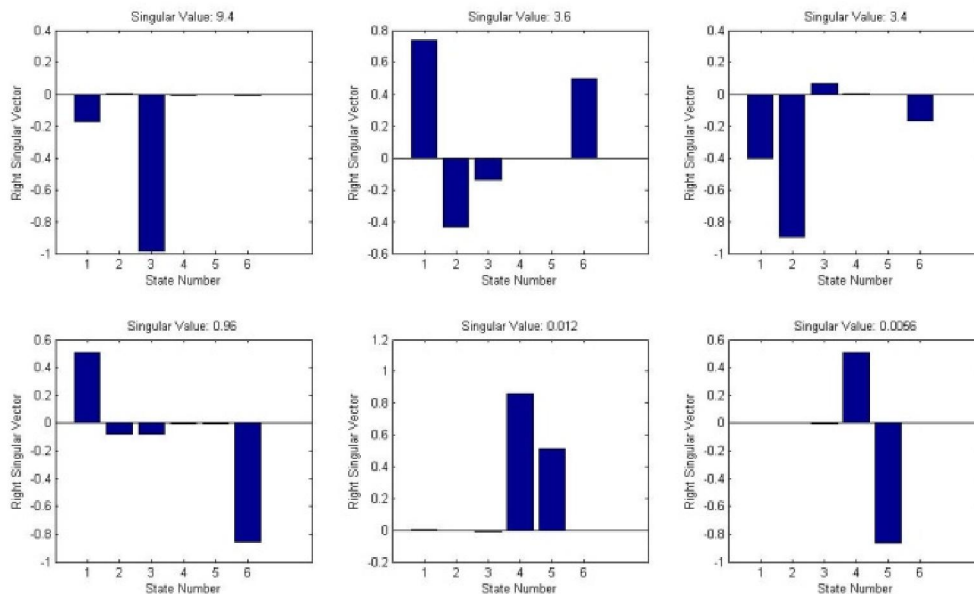


Figure 5-9 SVD for 6-state gyro (change ω)

Table 5-8 6-state gyro observability matrix SVD

Singular Value	Segment I (constant heading)	Segment II (change ω)
Easting	2.7	3.6
Northing	1.3	3.4
Heading	7.7	9.4
Gyro Bias	7.7E-3	1.2E-2
Gyro Scale Factor	4.6E-18	5.6E-3
Stride Length Bias	0.57	0.96

Finally, the SVD result for the 9-state gyroscope is shown in Table 5-9. The corresponding singular vectors for each segment are given. As shown in Figure 5-10, in the first segment with constant heading, the unobservable states for constant heading are pitch, roll, Gyro X Bias, and Gyro Y Bias, as can be seen from the small singular values in red in the table. The second segment added another maneuver by changing heading and rotation rate. This maneuvering made Gyro X bias observable, as shown in Figure 5-11. The third segment added more maneuver in

rotation rate, which improves the observability in Gyro Y bias, but pitch and roll still remained unobservable, as shown in Figure 5-12. In this example the addition of more segments by introducing other motions didn't improve the observability. It is due to the 2D nature of the pedestrian position change, which did not make the 3D attitude fully observable.

Table 5-9 9-state gyro observability matrix SVD

Singular Value	Segment I (constant heading)	Segment II (heading rate= ω_1)	Segment III (heading rate= ω_2)
Easting	4.1	5.5	6.6
Northing	3.5	5.0	6.1
Pitch	7.9E-17	8.9E-17	1.5E-16
Roll	1.3E-20	5.4E-17	7.7E-17
Heading	0.45	0.59	0.98
Stride Length Bias	0.64	0.9	1.1
Gyro X Bias	2.6E-18	1.7	0.51
Gyro Y Bias	1.8E-17	1.9E-16	2.1
Gyro Z Bias	0.82	1.0	1.3

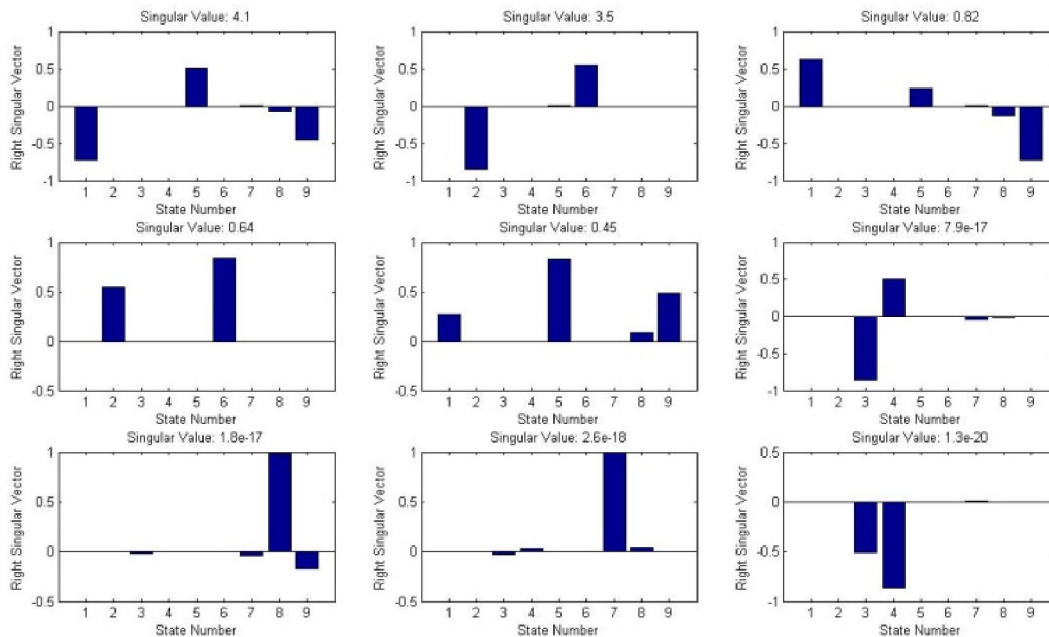


Figure 5-10 SVD for 9-state gyro (constant heading)

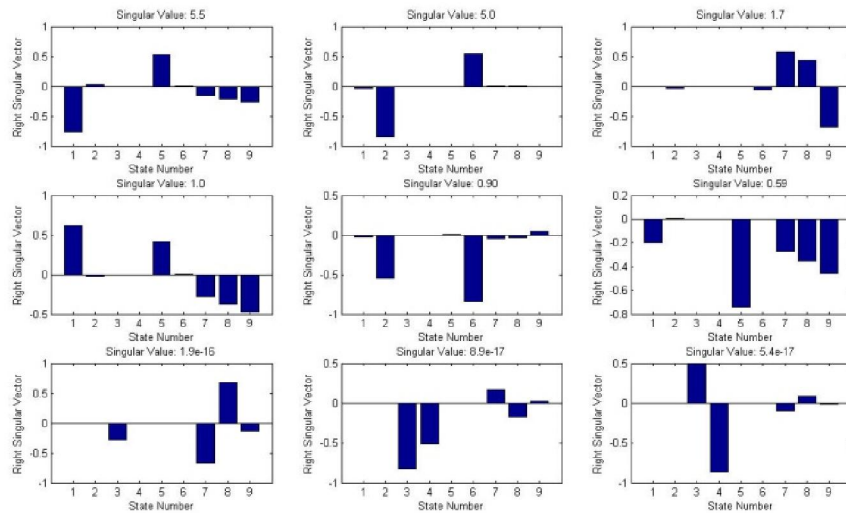


Figure 5-11 SVD for 9-state gyro (change heading/ ω_1)

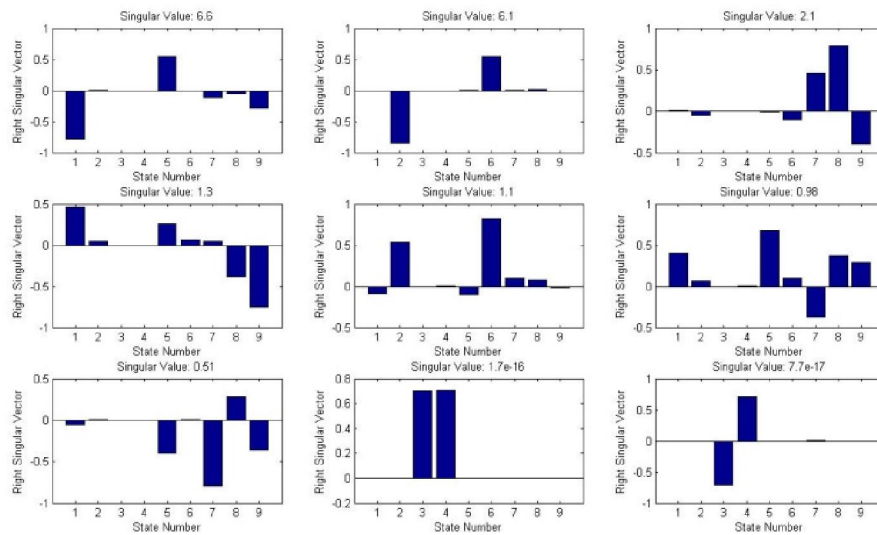


Figure 5-12 SVD for 9-state gyro (change heading/ ω_2)

From the above analysis, magnetometer heading integrated with GPS configuration showed the strongest observability. Thus, it is recommended to adopt this integration when there is no obvious magnetic disturbance. Due to the unobservable or weakly observable states in the 9-

states Gyro DR/GPS integration, it is beneficial to use 6-states Gyro DR/GPS integration for a robust INS solution. As indicated from the SVD analysis, a change in angular acceleration improves the observability of the gyro sensor errors. The scale factor error of the gyro, though observable, is still weakly observable compared to bias, therefore if the gyro's nonlinearity is not severe within short GPS outages, it can be neglected.

Some field test results in Chapter6 further indicate that a reduced multi-sensor configuration with heading gyro or magnetometer for personal navigation will be a feasible choice. Furthermore, the simplified computation is always a merit in real-time navigation applications. The results from the field tests in Chapter6 will demonstrate the usage of different configurations in real applications.

5.4 Altitude Integration

Pedestrian dead reckoning introduced so far is mainly used to solve two dimensional navigation problems. However, some applications need an altitude solution as well for use cases such as being able to tell which floor a user is on in an indoor shopping mall. GPS height is available only when satellite signals are strong enough. A barometer is good at measuring relative height changes, but its absolute height calculation is prone to drift from varying changes in ambient environment variables, including temperature, humidity, ventilation etc. Based on the barometer sensor introduced in Chapter 2.4, this section presents a simple Kalman filter fusion to integrate GPS height data with barometer measurements.

5.4.1 GPS/Barometer Height Fusion

The basic idea for the height fusion is to use GPS height to calibrate barometer height offset when the satellite signals are strong enough. From the previous height definition, the heights from the two systems are inherently off by the geoid height, which varies at different locations. Also random turn-on bias and environment dependent noise are imposed upon barometer output. So totally, all these factors are lumped as an additive bias state, h_{bias} , to be estimated. Another state included in the Kalman filter is the height derived from barometer measurement using Equation (2.11) in Chapter 2.

$$X = [h_{baro} \quad h_{bias}]^T \quad (5.25)$$

For the simplicity of the fusion, both states are modeled by a random walk process as no more sensors knowledge was given. Hence,

$$\begin{aligned} \dot{h}_{baro} &= \omega_{baro} \\ \dot{h}_{bias} &= \omega_{bias} \end{aligned} \quad (5.26)$$

Then the state transition matrix is:

$$\Phi = \begin{bmatrix} 1 & 0 \\ 0 & 1 \end{bmatrix} \quad (5.27)$$

The measurement from GPS height can be related to the estimated states as:

$$Z_k = h_{GNSS} = h_{baro} + h_{bias} \quad (5.28)$$

Then the measurement matrix H is as follows:

$$H = [1 \quad 1] \quad (5.29)$$

The system noise matrix Q_k is selected empirically. The error variance of h_{baro} can be estimated by calculating the variance of the actual height measurement online in a moving windows. The error variance of h_{bias} can be chosen based on the barometer relative pressure accuracy, or is sometimes given as resolution in the datasheet.

$$Q_k = \begin{bmatrix} baro_var_k & 0 \\ 0 & baro_res^2 \end{bmatrix} \quad (5.30)$$

The Measurement noise R_k is from GPS height variance. A justification of GPS weight is needed according to different GPS receivers' performance. R_k is set smaller at the initial 30 seconds of the fusion to accelerate Kalman filter converging at the beginning. Once all the parameters are set, height fusion can be conducted following standard prediction and update procedures in the Kalman Filter. The final corrected height solution is:

$$Baro_corrected_height = X_k[0] + X_k[1] \quad (5.31)$$

5.4.2 Height Fusion Test Result

Below is an example of testing results, using a uBlox-5T GPS receiver and a MS5803 barometer, around an office building. The test starts from outdoors; then the tester enters an office building and walk upstairs to the second floor; then the tester takes an elevator to go upstairs to the fourth floor and walks a while; after that it goes downstairs from the fourth to main floor and finally exits the building. As can be seen in the second half of Figure 5-13(a) and (b), the barometer height quickly converges to the GPS height with the Kalman filter correction when it is outdoors. The indoor region is marked between two dash lines in Figure 5-13(b), where the GPS height is

greatly biased or unavailable indoors; the corrected barometer height can still maintain the height change properly.

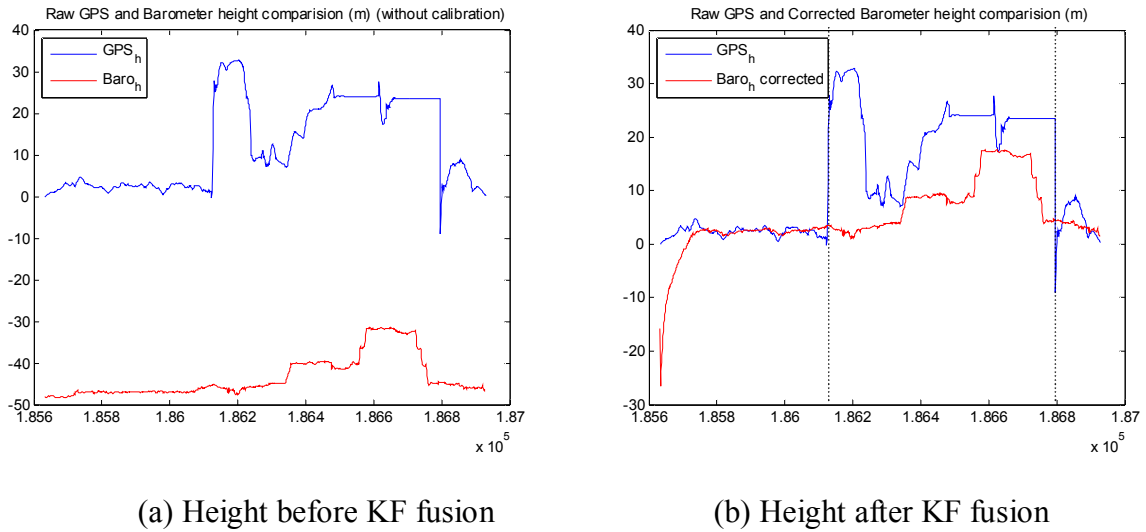


Figure 5-13 Barometer/GPS height fusion comparison

5.5 Wi-Fi Positioning for Indoor Environment

5.5.1 Indoor Wi-Fi Signal Propagation Modeling

Chapter 2.3 introduced Wi-Fi based positioning methods and wireless signal propagation modeling for the indoor environment. Consequently, this sector applies the method for Wi-Fi indoor positioning. In chapter 2, to a curve fitting between path loss and distance given in Equation (5.32) as shown below:

$$PL(d) = A + B \log(d) \quad (5.32)$$

Several indoor field tests were performed to determine the channel model. The survey sites were carefully chosen to represent the most typical scenarios for indoor environments. Figure 5-14 shows four places that were intensively studied with varying locations of the access points provided in red circles. In (a) and (d), the access point are placed above the ceiling and

embedded in the wall so there is no direct line-of-sight of the signals; on the contrary, in (b) and (c), the access points are hanging on the wall of the spacious lecture room and hallway, corresponding to line-of-sight signal propagation environment. The data for each distance were recorded for around 3 minutes and the path loss value was obtained from its expectation.



(a) Above ceiling



(b) Lecture room



(c) Wide hallway



(d) Narrow corridor

Figure 5-14 Access point radio propagation modeling in different scenarios

The models for the above cases are summarized in Table 5-10 below.

Table 5-10 Radio propagation models for different scenarios

Scenario	(a)	(b)	(c)	(d)
Place	ENE228	ENE239	ENE238	ENF212
Type	NLOS	LOS	LOS	NLOS
Path Loss Model (dB)	$2.7*10\log d + 37$	$2.6*10\log d + 41$	$2.3*10\log d + 34$	$2.6*10\log d + 40$

Although signal strength varies from reflections, diffraction, and scattering of radio waves caused by structures within the building, the path loss in the propagation models are similar for different scenarios. Therefore, a compromised model can be obtained to accommodate all the indoor environments as given below:

$$PL(d) = 40 + 2.6\log(d) \quad (5.33)$$

The complete Wi-Fi positioning algorithm used in this work is summarized as follows:

1. Define a reliable received signal strength threshold for received AP. (SNR 49dB~ 10m)
2. Estimate the user position based on weighted centroid location algorithm (when the number of APs ≤ 2).
3. Estimate the user position based on least squares estimation (when the numbers of APs > 2).
4. Assign proper standard deviation of the estimated position errors from receiver's SNR.

5.5.2 Wi-Fi Positioning Field Test

To verify the developed Wi-Fi positioning algorithm, NetStumbler software [Netstumber 2010] installed on a laptop with a WLAN card was used for the data collection of all the Wi-Fi access points during the field tests. An access point broadcasts its service set identifier (SSID) and other networks information in the Wi-Fi beacon data package every 100 ms. During the test, each detected access point is recorded including its signal strength, noise level, and the MAC address. The set-up formed by the access point and the stations located within the coverage area are called the basic service set, or BSS for short. They form one cell. Each BSS is identified by a unique identifier assigned to each network device, known as a BSSID, which is a 6-byte (48-bits) identifier.

There are several network providers for Wi-Fi access at the University of Calgary. For this study, only AirUC is identified and surveyed, since it offers the best coverage on campus. Compliant with the IEEE 802.11 a/b/g standard, AirUC wireless networks operate in the unlicensed frequency bands of 2.40-2.48 GHz. The 2.4 GHz band is further divided into 14 channels supporting maximum data rate of 54 Mbps [O'Keefe 2008]. During the test, most of the AirUC hotspots on campus are Aruba AP-70 dual-radio Wi-Fi transceiver. Most devices are set at maximum transmission power of +17.0 dbm while the receiver sensitivity is about -73.0 dbm. A dataset was collected using the prototype introduced in Section 6.2 in January 2010 around the engineering building on the University of Calgary campus. It is a 10-minute walk from outdoors to indoors. The reference trajectory is depicted in Figure 5-15, it was generated using Aided Inertial Navigation System Toolbox from Mobile Multi-Sensor Systems (MMSS) Group, the University of Calgary, backward smoothing filter is used in the post processing, and it is within 5 meters of accuracy compared to the truth trajectory recorded by the tester [Zhao 2010]. The test

started at the east door entrance of the Block A building; the user then walked two loops outdoors and entered the Block C building; then the user walked indoors, made turn and went upstairs to the second floor, after making several turns at Block D and walking along the hallway of Block E , the user finally stopped at the southwest side of the Block F building.

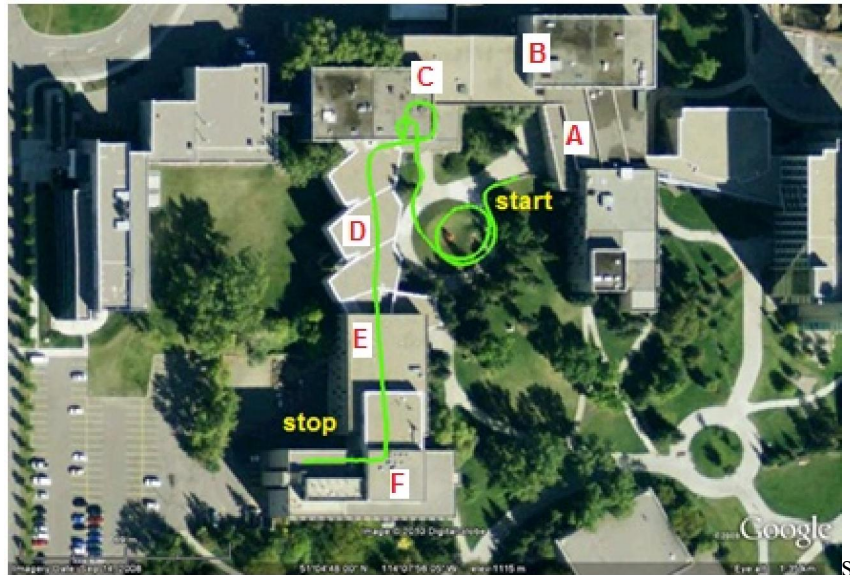


Figure 5-15 Field test reference trajectory

This exemplifies the importance of Wi-Fi updates for deep indoor environments. Along the whole trajectory, the receiver had access to more than 250 access points altogether. In the data processing, however, only 12 APs (5 Line-of-Sight) were used for two reasons. First, not all the APs had strong signals to rely on, so a SNR threshold of 49 dB was selected to reject weak Wi-Fi signals. Second, common indoor environments will usually have a less dense distribution of APs available than on campus and we need to test this concept under more standard conditions, as our goal is wide adoption by the general public.

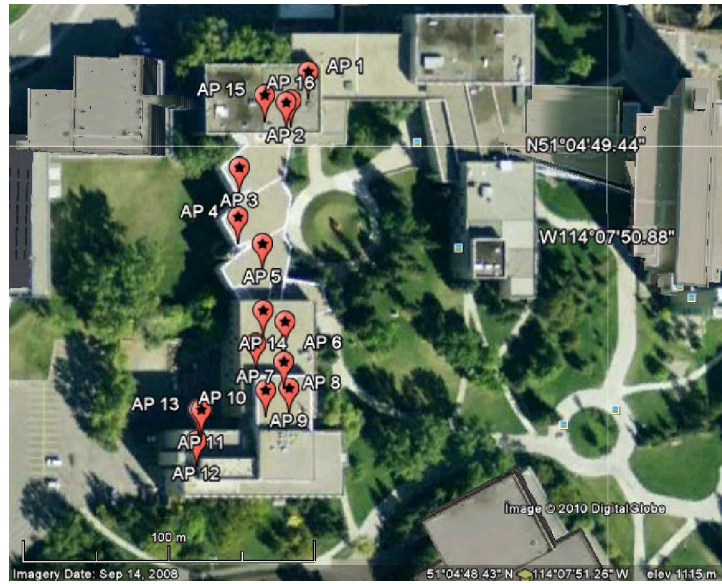


Figure 5-16 Selected Wi-Fi access points

The selected APs are shown in Figure 5-16. Because of the practical installation limitation in the building, the geometry distribution of the APs is poor for positioning. The surveyed APs are summarized in Table 5-11 where E, N and Z are the known local coordinates for each AP. As can be seen from the table, the maximum SNR for each AP is above threshold suggesting the trajectory was very close to the APs at certain point.

Due to the severe obstruction of the adjacent buildings and challenging indoor environment of the concrete building, the GPS-only solution for outdoors and indoors delivered very poor results for whole test. As shown in Figure 5-17, the GPS was only available at the beginning of the test when the user was outside the building and at the end of the indoor part of the trajectory, which was when the tester was close to the building windows. From Figure 5-17, approximately 50% of Wi-Fi positions are available along the trajectory and the GPS positions are only accepted at the beginning of the trajectory when the user was outdoors. Based on the given AP coverage, Wi-Fi only positioning can provide accuracy within 20 meters. The complete Wi-Fi and GPS positions integrated with MEMS-based PDR testing will be covered in Chapter 6.

Table 5-11 Selected access point for positioning

AP	Mac Addr.	Room/AP Type	E(m)	N(m)	Z(m)	Max SNR (dB)
1	00:0B:86:C8:8E:60	ENC201/NLOS	-2.5	16.5	7.6	69
2	00:0B:86:CA:B0:60	ENC210Y/LOS	-9.6	5.8	4.4	64
3	00:0B:86:CA:DF:20	ENE239/NLOS	-25	-16.8	8.0	49
4	00:0B:86:CA:D8:60	ENE241/NLOS	-24.8	-33.6	8.0	52
5	00:0B:86:CE:A5:E0	ENE238Z/LOS	-16.1	-42.4	7.9	59
6	00:0B:86:CB:C5:C0	ENE229Z/NLOS	-7.4	-68.5	7.5	64
7	00:0B:86:CF:9C:E0	ENE228/NLOS	-17.1	-76.4	7.5	62
8	00:0B:86:D6:D4:80	ENE227Z/NLOS	-7.4	-82.2	7.5	61
9	00:0B:86:D0:A5:41	ENE228S/NLOS	-5.4	-91.2	8.1	64
10	00:0B:86:D6:90:21	ENE221Z/LOS	-13.4	-92.2	7.8	56
11	00:0B:86:CE:62:62	ENF212/NLOS	-35.1	-99.7	7	54
12	00:0B:86:D0:B4:C2	ENF275/NLOS	-36.3	-110	7	52

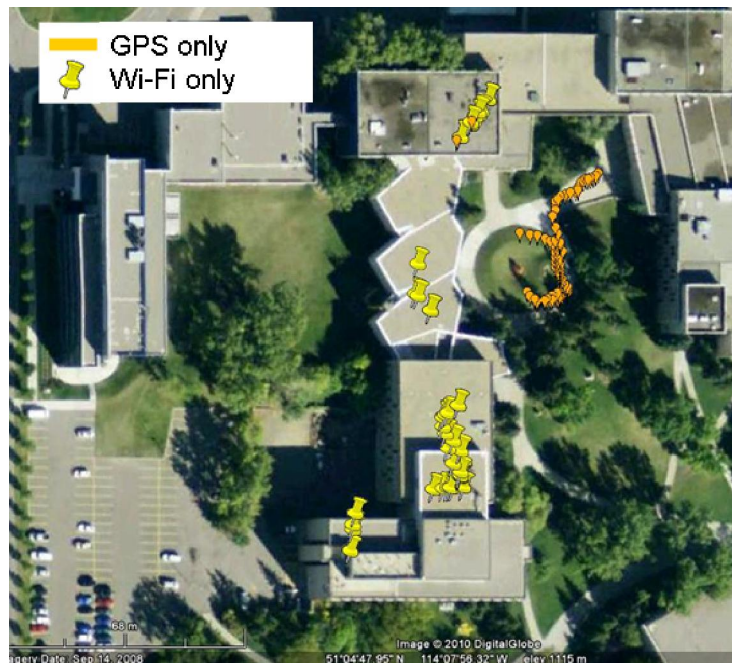


Figure 5-17 GPS + Wi-Fi solution after innovation testing

Chapter Six: **MULTI-SYSTEM INTEGRATION AND PROTOTYPING**

This chapter will present prototypes and test results to integrate multiple positioning subsystems together. The following sections show three positioning system integration prototypes built at various development stages: the first prototype integrates multiple MEMS sensors with GPS; the second one is a combination of Wi-Fi, GPS and IMU. The third one is a small form size design with all the subsystems leading towards an embedded solution that can be integrated into consumer products like a smartphone and wearable device.

Figure 6-1 illustrates the Personal Navigation System (PNS) architecture for the system integration. Raw measurements from multiple sensors are first calibrated and validated then sent to the sensor fusion modules. Pedestrian Dead Reckoning (PDR) is the main engine for pedestrian navigation. It includes step detection, stride length estimation, and heading determination, as studied in Section 5.1. A user's heading in PDR is derived from the nine-axis orientation fusion introduced in Chapter 4, along with pitch and roll output. To properly apply the heading information, misalignment correction between the device frame and navigation frame is included. Altitude can be derived by the GPS height and barometer fusion solution as introduced in Section 5.4. The GPS receiver gives measurement corrections in most outdoor environments and Wi-Fi positioning can provide the Kalman filter update in most indoor environments, as presented in Section 5.5. Finally, an extended Kalman filter discussed in Section 5.2 integrates the PDR estimates of positions with GPS and Wi-Fi position updates through a loosely-coupled scheme.

Note that because of constraints in system cost, power consumption, and size, a practical navigation system may only have a partial set of positioning subsystems covered in this chapter, yet the goal is to demonstrate that the system and algorithm design are scalable and reliable to meet system requirement under different use cases.

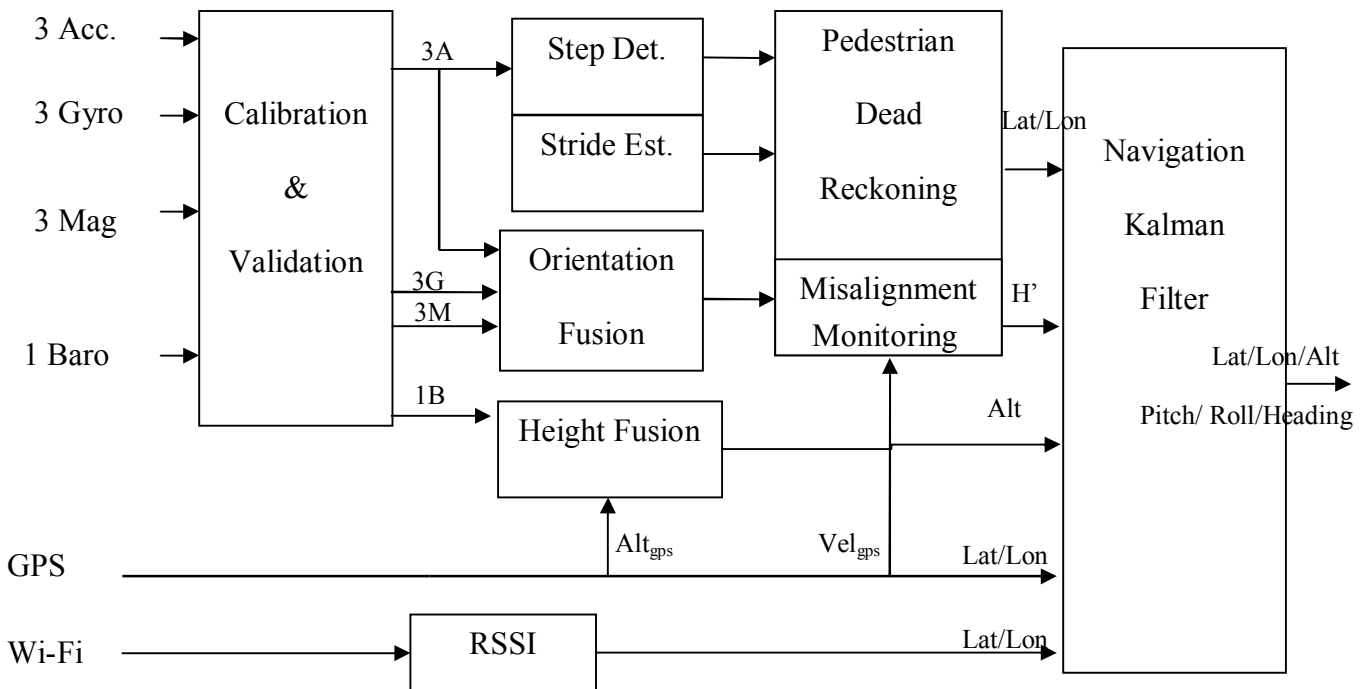


Figure 6-1 PNS system architecture

6.1 First Prototype: GPS-Sensor Integration

6.1.1 System Introduction

The first prototype unit was developed at the Mobile Multi-Sensor Systems (MMSS) Group, the University of Calgary, in 2008. Figure 6-2 below shows the hardware architecture of the prototype unit. Multiple MEMS sensors are integrated on board including tri-axial accelerometers (STM - LIS3L03AS4), three low-cost orthogonal gyroscopes (Epson - XV-8100),

three orthogonal magnetometers (Honeywell - HMC1052/HMC1051Z), a barometer (Measurement Specialties - Model1541), a temperature sensor (Microchip- MCP9700), and a GPS receiver module (uBlox - LEA-4T). The sensors output analog signals and are integrated in sub-modular circuit boards independently with the universal interface to 16-bit high resolution analog-to-digital converters. This platform enables a flexible and reconfigurable deployment of sensor combination to verify the performance of different configurations. The data collection is controlled by a low-power microcontroller, at a variable sampling rate ranging from 50 to 150 samples per second. The data is stored on an SD memory card for post processing. In navigation mode with a 3V battery, the whole unit consumes about 200mA.

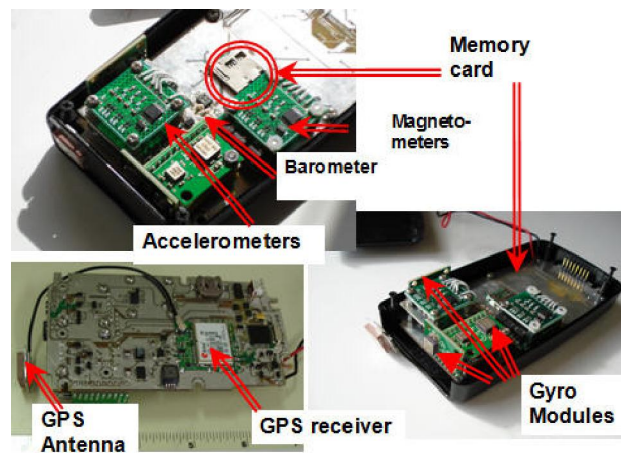


Figure 6-2 First prototype of portable navigation system

6.1.2 Results

The results from the field tests demonstrate the usage of different configurations under different scenarios. To verify the performances of different Kalman filter integration schemes, pedestrian field tests were performed and processed. The dataset consists of a 10 minute outdoor walk with straight-line walking as well as several L-turns and a U-turn on the University of Calgary

campus. As shown in Figure 6-3, the tests conducted are based on waist belt placement of the unit.



Figure 6-3 Illustration of the belt-mounted prototype unit

GPS signals are intentionally removed for 45 seconds during the second half of the U-turn to verify the EKF performance during GPS signal outages (GPS positions are given as white arrows in Figure 6-4). In this test, the magnetometer heading was free from magnetic anomalies as the testing path was contained in an area free of magnetic disturbances.

The different EKF solutions are provided in Figure 6-4 for comparison. The trajectory from the 6-state magnetometer DR/GPS EKF is plotted in blue while the red and yellow lines represent the 9-state gyro EKF and 6-state gyro EKF solutions, respectively. As can be seen in Table 6-1, the magnetometer integration renders the best performance while the 9-state gyro EKF has the largest error. This is consistent with the different observability results discussed in Section 5.2.

Table 6-1 Maximum position drifts during GPS signal outage of 45 seconds

EKF Configuration	Maximum Position Error (m)
Mag. EKF - (6-state)	5.5
Gyro EKF - (6-state)	8.2
Gyro EKF - (9-state)	9.1

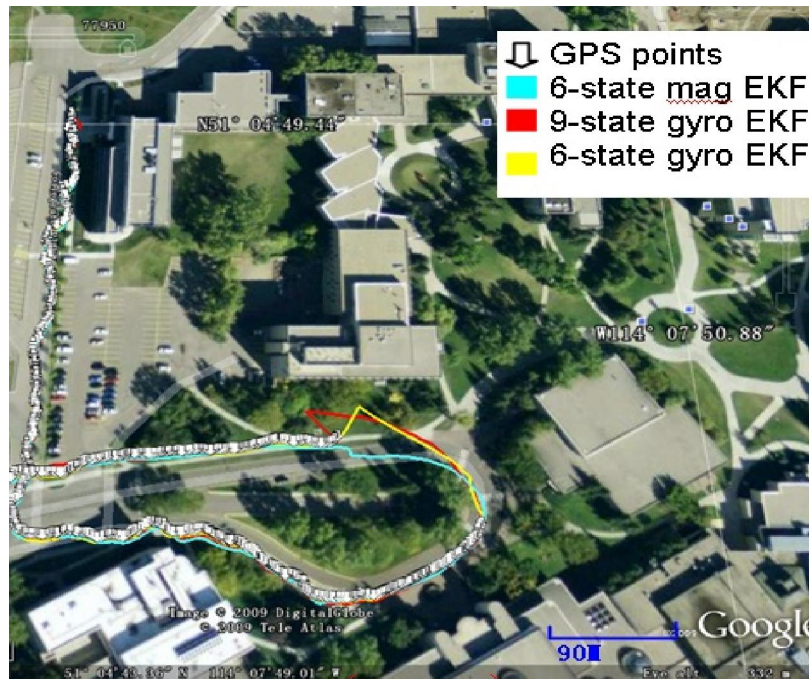


Figure 6-4 Field test solutions for outdoor navigation

6.2 Second Prototype: Wi-Fi-GPS-Sensor Integration

6.2.1 System Introduction

The second prototyping system is focused on Wi-Fi assistance when GPS signals are not available in deep indoor environments. To verify the Wi-Fi positioning algorithms introduced in Section 5.4, a test system was set up using off-the-shelf subsystems consisting of a laptop with a WLAN Mini-card, Garmin CS60X GPS receiver, and ADI ADIS16405 IMU, as shown in Figure 6-5. The IMU is an automotive grade MEMS unit that contains a tri-axial digital gyro, accelerometer, and magnetometer. All the sensors and GPS data are collected by computer via USB connections so that all the data is time synchronized.



Figure 6-5 Wi-Fi+GPS+IMU prototype system

Similar to the previous prototype, the EKF algorithm is the system integration kernel. It processes all the sensor data and GPS/ Wi-Fi updates. The EKF propagates the state parameters of discrete-time controlled processes governed by pedestrian sensor equations, and then updates the parameters when GPS/Wi-Fi position fix updates are available for correction. The key difference from the first prototype is that dual measurements from both GPS and Wi-Fi are leveraged. Since the fusion result is weighted accordingly from the covariance matrices of the system noise Q and measurement noise R , proper estimation of Q and R matrices are important for optimal integration. More specifically, the measurement noise should be adaptable based on the SNR of the Wi-Fi signal and the positioning uncertainty of the GPS receiver. The Wi-Fi SNR selection and empirical relationship with positioning error was given Section 5.4. To reduce the GPS receiver's negative impact in weak signal case, we set the cutoff threshold of carrier-to-noise ratio of 30dB-Hz, so that the integration only uses GPS update in good signal conditions.

6.2.2 Results

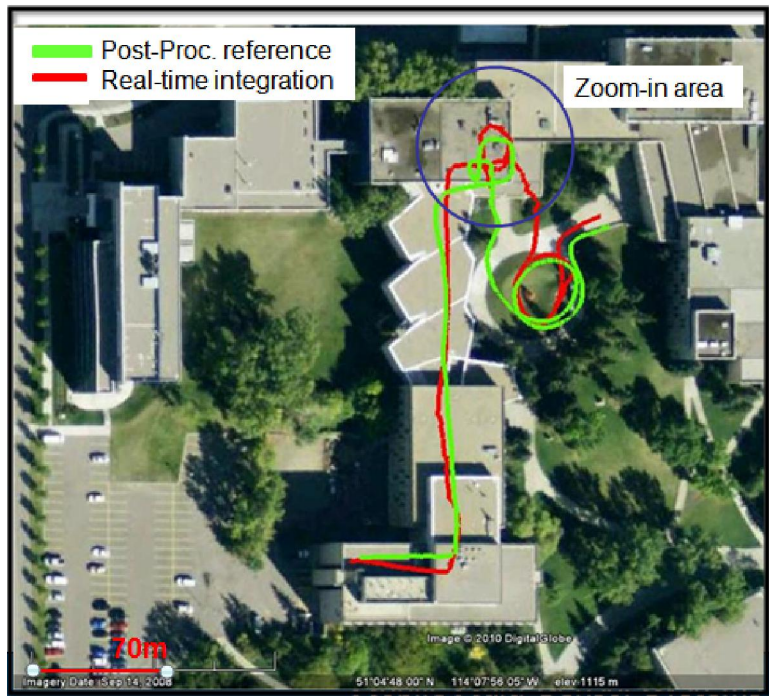
Refer to testSection5.4 Explain the test or refer to other section where the test was described

Figure 6-6 presents the positioning solutions using GPS, Wi-Fi, and PDR independently. The GPS was available for 25% of the whole trajectory while the Wi-Fi positions were available approximately 50% of the indoor trajectory. From this figure, we can see that without proper multi-sensor integration with GPS and Wi-Fi, the trajectory is off and cannot be used to accurately locate rooms, turns, or floors inside the building.

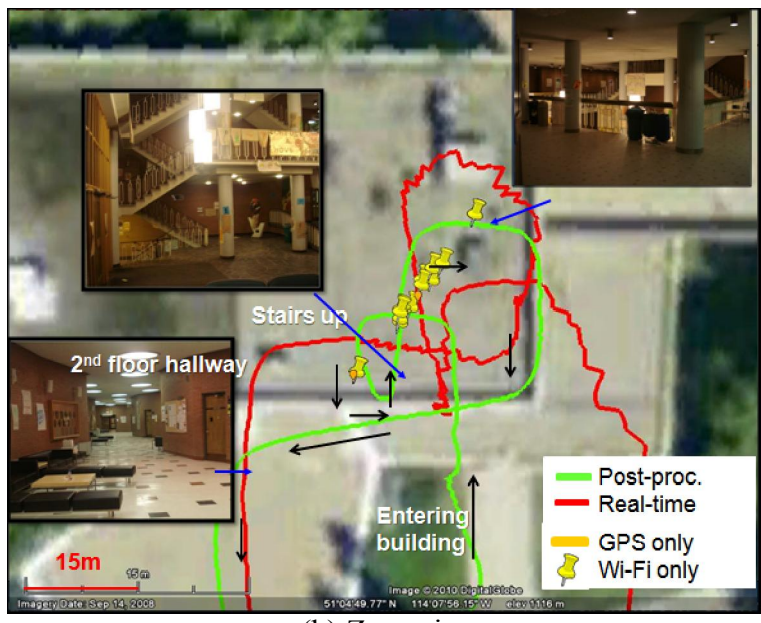


Figure 6-6 Comparison of GPS/Wi-Fi/PDR stand-alone solutions

Using the EKF integration with GPS and Wi-Fi to provide correction updates, as introduced in the previous section, bridges all the outages, as shown in Figure 6-7. In addition, bad data calculated from faulty measurements can be rejected based on the innovation testing method introduced above. The real-time positioning errors are summarized in Table 6-2. The 3D error are within 15 meters with a mean of 7.5 meters. The heading errors are within 20 degrees with a mean of about 10 degrees. As can be seen, all eight turns along the trajectory are correctly captured by the real-time EKF solution.



(a)



(b) Zoom-in area

Figure 6-7 Real-time GPS/Wi-Fi/PDR EKF integrated solution

Table 6-2 Performance metrics for real-time EKF solution

Criteria	Accuracy
Mean position error (3D)	5.0 m
Max position error (3D)	13.2 m
Mean heading error	9.9 deg
Maximum heading error	15.8 deg

6.3 Third Prototype: Consumer Grade Multi-Sensors System

6.3.1 System Introduction

The third prototype is a more compact design in a USB dongle form factor, as shown in Figure 6-8. It was designed by Marvell using more recent MEMS sensors. The IMU is a six-axis accelerometer and gyro combo. Also included are the chipsets as follows: accelerometer and gyro combo (STM -LSM330DLC), the three-axis magnetometer (AKM-AK8963C), and the barometer with temperature sensor (STM- LPS331AP). Marvell's GPS Location Processor, 88L1000, is shielded in a metal box soldered on the same board. The device can be directly plugged into a USB port on a portable device where the positioning algorithms are running on a host processor in a real-time. As many portable devices have Wi-Fi connectivity, such as a laptop or netbook computer, Wi-Fi positioning updates introduced in this thesis can be applied as well, thus completing the hybrid positioning solution.



Figure 6-8 Third prototype

6.3.2 Orientation Alignment

The attitude sensor fusion introduced in Chapter 4 provides a mechanism for isolating the navigation system from the body's motion, as well as optimally aligns orientation to a particular frame of navigation. However, in practical deployment of the PNS unit, the system may be required to work with many different placements. There is no way to guarantee that the sensors will be placed such that they are perfectly aligned with the direction of travel. So there is a misalignment angle between the azimuth computed in phone's body frame and the true azimuth of the person's displacement in the navigation frame that needs to be accounted for [Ali 2013]. Following the Right-Forward-Up (RFU) definition for body frame and East-North-Up (ENU) definition for navigation frame as introduced previously, the misalignment angle, H' , is illustrated in Figure 6-9.

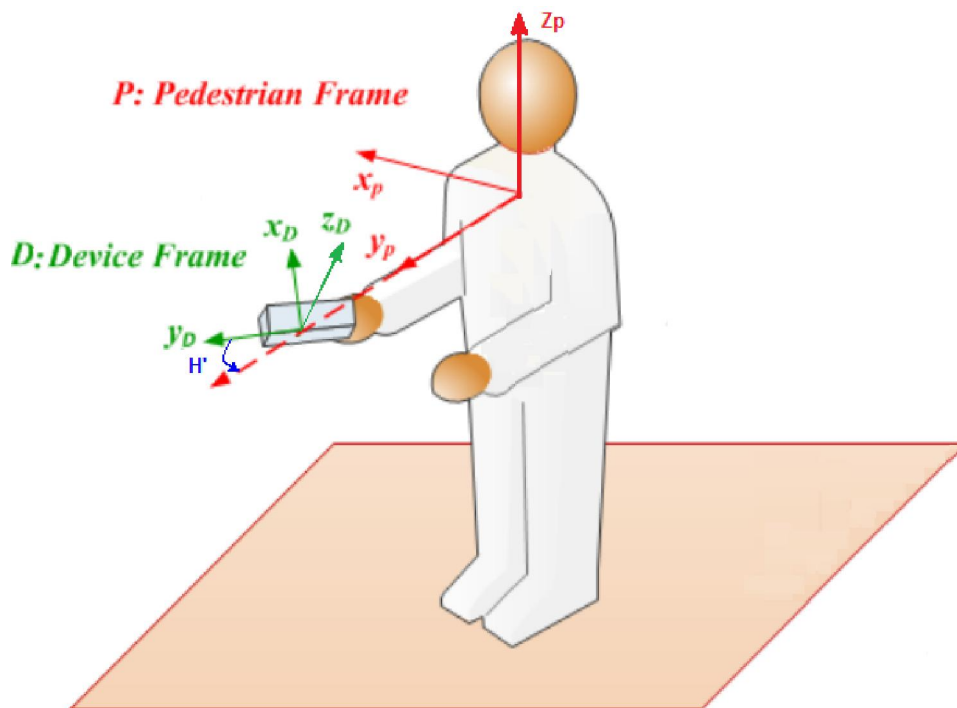


Figure 6-3 Illustration of misalignment angle

Using the method from Section 4.2.2, the initial attitude of the device can be obtained with heading angle H_0 . Then the heading angle H corresponding to the user's walking direction is calculated as:

$$H = H_0 + H' \quad (6.1)$$

Some literature discusses how to do in-motion alignment estimation to get heading correctly. Rogers [Rogers1997] considers the heading error as an initial wander azimuth error to separate the large heading error and small leveling errors. This initial wander error can be estimated by position measurements in the Kalman filter. However, because the coupling coefficients between the trigonometric azimuth angle errors and the position errors as well as the velocity errors are small, the observability is weak, especially for personal navigations where the magnitude of position and velocity change are limited. [Scherzinger1996] and [Hong2004] modeled the sine and cosine of the platform heading misalignment into the INS error equations, which has larger coupling with the measurements. In addition, in most systems, the heading error is generally much larger than leveling errors. So if leveling errors can be constrained to small values, separation of heading error and leveling is possible by introducing a new horizontal frame and consequently simplifying the cosine direction matrix derivation.

Most large heading uncertainty models were applied for airplane and vehicle navigation, and have seldom been applied for personal navigation. For multi-sensor systems mounted on the human body, more challenges arise for a couple of reasons. First of all, the mounting platform is less rigid on a person, so more vibration and flexure will occur during movement. Secondly, humans can only move with low dynamics, so the observability is generally worse than vehicles. Finally, most personal navigation devices for the consumer market use low-cost sensors and GPS

solutions, which are more susceptible to device errors. Therefore, a more realistic method is to have a misalignment monitoring module. Referring to Figure 6.1, where it compares heading calculation differences between a MEMS sensor fusion solution and GPS solution, assuming they are constant for a particular device placement without significant shifting or deviation from the original placement and orientation on the moving body. When the heading difference is larger than a preset threshold, for example, 30 degree, then the misalignment correction H' will be applied to sensor-based heading in Equation (6.4).

6.3.3 Results

Using the third prototyping device, some real-life indoor positioning tests were done at Valley Fair Mall in Santa Clara. It contains a 15 minute walk starting outside of the mall entrance, and then walks along a figure eight trajectory through the mall and finally exits at the entrance point. The testing unit was held in hand with small initial misalignment. As the coordinates of the Wi-Fi access points were not surveyed ahead of time, so GPS was the only absolute positioning source for this test. The indoor area of the mall has thick concrete walls, so GPS signals were greatly attenuated for the majority of the time; only a few areas in the mall have windows to enable for temporary GPS fixes. Overall, it was challenging to get accurate location data with weak GPS signals for the Kalman filter integration. The horizontal and vertical positioning standard deviation are generated from the covariance matrix of GPS position Kalman filter and are shown in Figure 6-10, sometimes the GPS signals were lost, so the positions and uncertainty are kept to the last known value.

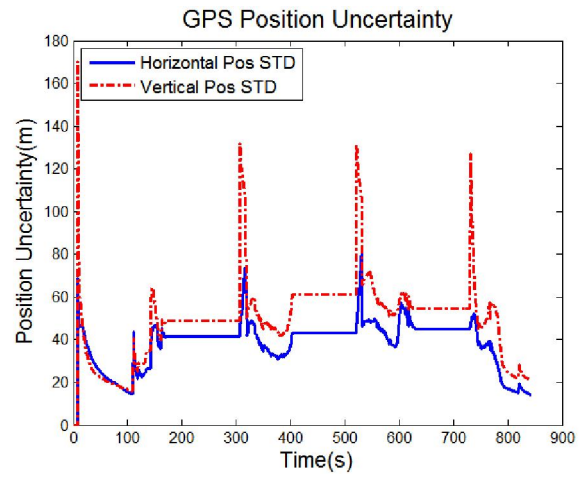


Figure 6-4 Testing environment and GPS position uncertainty

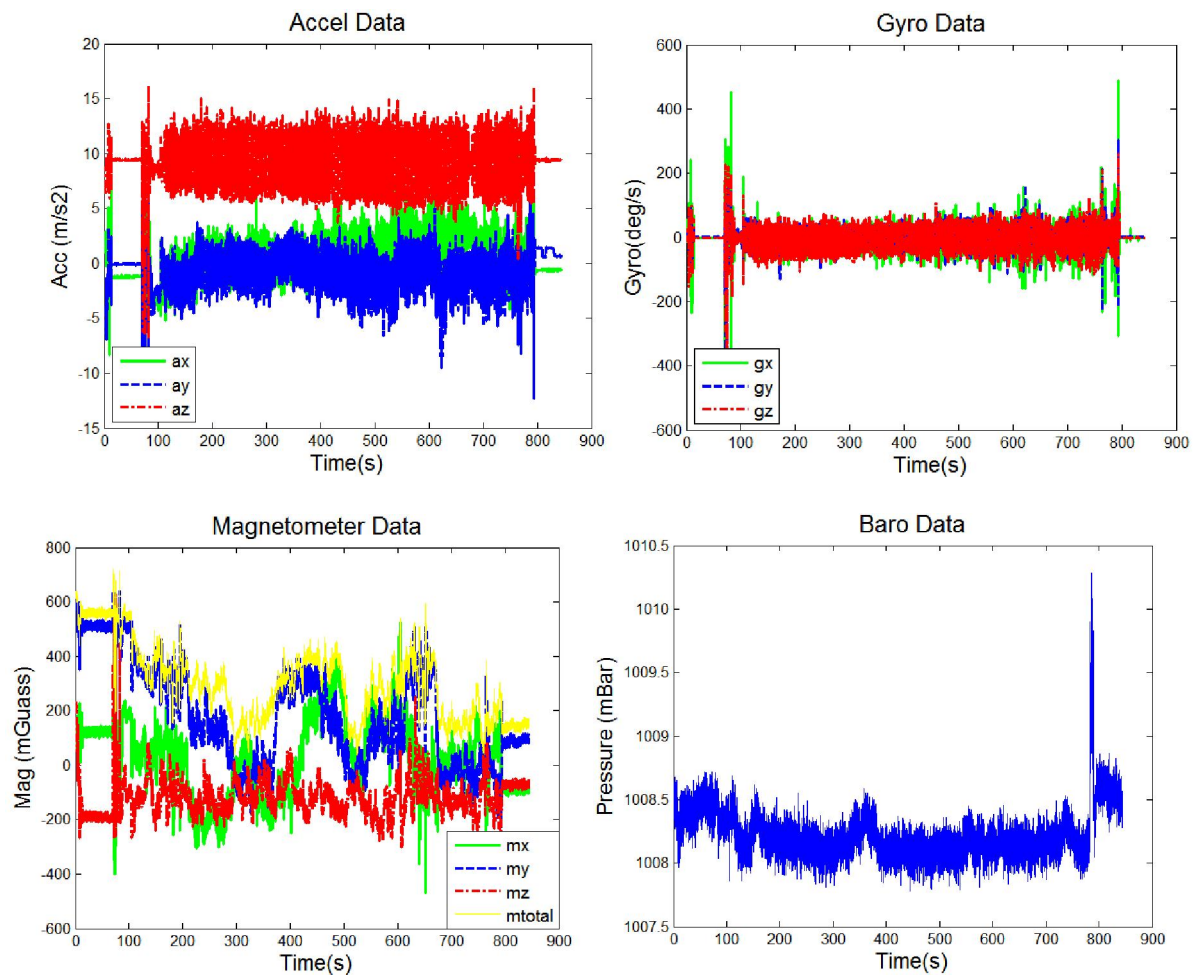


Figure 6-11 10-Axis MEMS sensors signals

The 10-axis MEMS sensors inputs are shown in Figure 6-11. From which, we can derive the device's attitude then apply the PDR algorithms. Note the magnetometers experience large disturbances from the time-variant indoor magnetic interference at different locations, as can be seen from the big fluctuations of the total magnetic strength plotted by the yellow curve.

Step detection and stride length results are given in Figure 6-12 based on the methods introduced in Section 5.1. There are a few stops during the walking so the stride length returns to zero at these times.

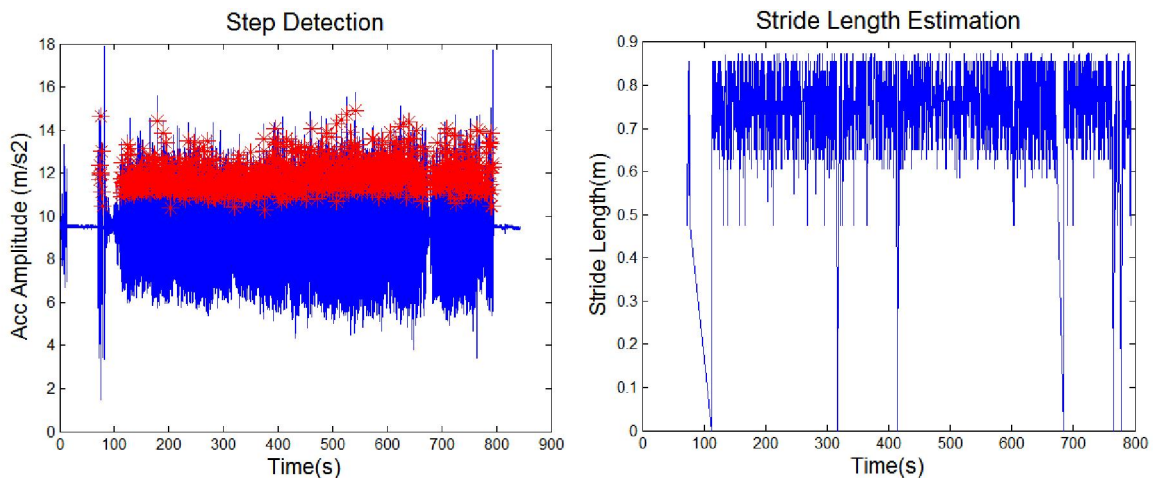


Figure 6-12 Step detection and stride length estimation

The heading results comparison of gyro-only, magnetometer-only, and 9-axis sensor fusion is given in Figure 6-13. There was not high accuracy reference for the heading, but the starting lane after the main building entrance is roughly northbound (0 degree heading around 100s-200s) and exiting lanes a roughly southbound route (180 degree heading around 680s-800s, because of the roll over between -180 and 180, it appears more fluctuations but actual error of EKF is within 20 degree). We can see the gyro's heading is smoother than the magnetometer's but slowly drifts away, heading fusion based on the 9-axis attitude EKF renders the best solution.

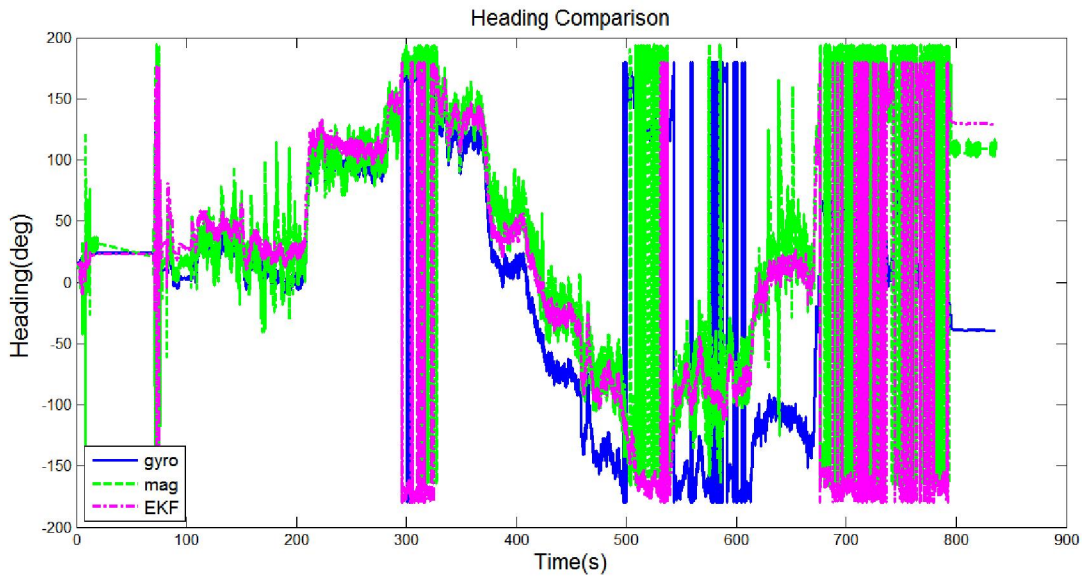


Figure 6-5 Heading results comparison

Height results from GPS, the barometer, and their fusion are compared in Figure 6-14, since GPS is largely unavailable indoors; it jumps to very inaccurate values. The barometer can generate a smooth height output, yet it has a large offset. Height Fusion between the two gives the best solution by correcting the biases using the GPS solution's results from the beginning.

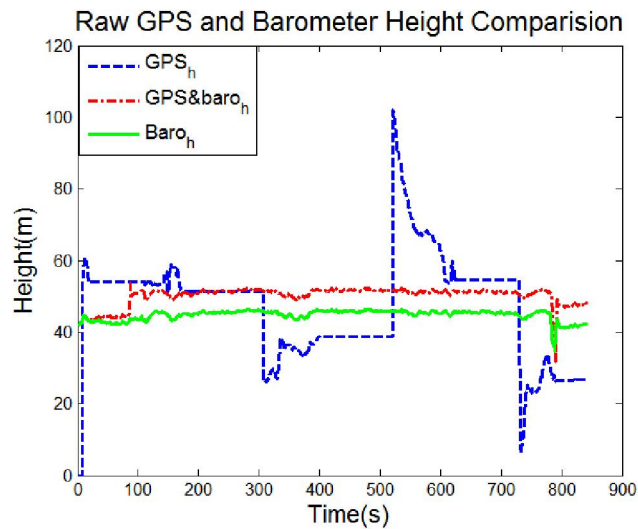


Figure 6-6 Height results comparison

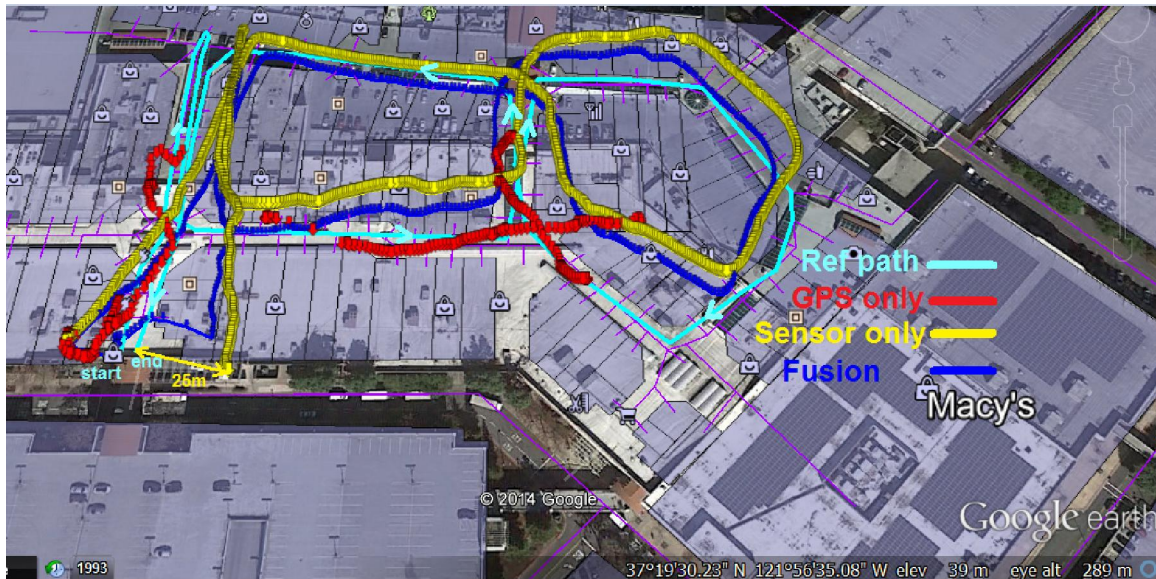


Figure 6-7 Positioning results comparison

Finally the positioning trajectory from GPS only, sensors only, and Kalman filter fusion are compared in Figure 6-15. Because of the signal obstruction, GPS-only solution provides positions at the beginning/ending areas and a few areas throughout the test where happened to be near windows that offered enough signal penetration to get a fix. In this test, the sensor-only solution behaves well, being able to track all the users' turns correctly. However, it drifts gradually over the time. Since GPS signals are weak and walking speed is slow, GPS heading cannot correct the initial misalignment angle very well, thus 30 degrees threshold for misalignment detection was not triggered. From Figure 6-15, heading errors of 10-30 degree exist for the trajectory compared to the reference data. The ending position from the sensors-only solution drifts about 25 meters, which gives worse case accumulated positioning error bound. After the tester exited the building, the fusion solution is able to correct quickly when GPS positions recover at the end. The test proves the positioning algorithms discussed in this thesis are feasible and effective to meet FCC's indoor positioning specification in practical personal navigation applications.

Chapter Seven: **CONCLUSIONS AND RECOMMENDATIONS**

The main objective of this thesis was the analysis and development of a low-cost, personal navigation system and the estimation algorithms required to combine input data from multiple MEMS sensors. To this end, the integration of MEMS sensors, Wi-Fi, and GPS offers the best configuration for a solution that works in a multitude of environments and seamlessly estimates location data when shifting from one environment to another. This chapter summarizes thesis contribution, concludes the thesis work and gives recommendations for future work.

7.1 Conclusions

Details of the major conclusions of this thesis are summarized below based on the objectives set out in Chapter one.

Analysis, Error Modeling and Calibration of Low-cost MEMS Sensors (Chapter 3)

This thesis gives a comprehensive overview of modern MEMS sensors for navigation. The fabrication and design technologies are introduced; details of the integrated circuitry design are beyond the scope of the thesis, yet this thesis derives the key MEMS-based inertial sensor design parameters and presents their key performance relationship to navigation. From there, stochastic and deterministic error models are formed for navigation estimation. Gyro and magnetometer sensors are particularly pertinent to attitude accuracy, thus are given more attention to their error characteristics and online calibration methods.

Nine-axis Attitude Sensor Fusion (Chapter 4)

Inspired by space scientists using inertial and magnetic sensors for spacecraft navigation, this thesis investigates similar mathematical calculations but targets embedded consumer products using low-cost MEMS sensors. The nine-axis fusion of accelerometers, gyroscopes, and

magnetometers is elaborated into an attitude Kalman filter such that the gyroscopes data are used to maintain quaternion predictions while accelerometers and magnetometers give measurements that periodically estimate corrections.

Key Algorithms for Indoor Positioning (Chapter 5)

Indoor positioning required alternative positioning systems when GPS signals are degraded. The following hybrid positioning algorithms are explored in detail:

- A **pedestrian dead reckoning algorithm** is developed based on the accelerometer's step detection and stride length estimation with the heading determined from the attitude sensor fusion.
- **Observability analysis for pedestrian navigation** is introduced so that proper states are selected for Kalman filter estimation under different motions. Three pedestrian navigation filters are constructed and the degrees of observability of each estimated state are compared.
- **Wi-Fi positioning** is investigated for indoor environments. Wireless signal propagation characteristics are modeled to derive the pseudoranges and then trilateration is done based on received signal strength.
- **Altitude integration** of the barometer and GPS height measurements is introduced. Height calculation from air pressure measurements in the barometer can be calibrated automatically when GPS has a good position fix outdoors. After calibration, it can be used to estimate vertical position.

Hybrid Positioning Fusion (Chapter 6)

An Extended Kalman Filter (EKF) is selected in this thesis as the core engine to perform the data fusion from multiple nonlinear positioning systems including PDR, GPS, barometer, and Wi-Fi

measurements. Field tests results under three different application scenarios and prototyping units are presented.

With the concentration on the above studies, this thesis can be concluded as follows:

1. Firstly, based on the study of MEMS technologies and their deployment in navigation applications, gyroscopes are the most critical sensors for overall performance. There is an inherent trade-off for the Coriolis vibrating gyro design: the measurement bandwidth selection requires a compromise between the sensors' sensitivity and its noise performance. Hence the noise analysis of the gyro is of particular importance. The noise transfer functions are derived from the device design point of view. The error sources are mainly from the mechanical Brownian motion of the MEMS mass and electronics noise in the readout circuitry. Furthermore, this thesis presents a way of decomposing the error terms from static lab testing. Applying time-correlation and Allan variance analysis, the main modeling parameters can be quantified including bias, time-correlated Gaussian Markov noise, and angular random walk noise.
2. Secondly, the pedestrian dead reckoning algorithm is successfully implemented. Step detection and stride length estimation are derived based on accelerometers signals; the results show robust performance insensitive to the device placement. The step detection accuracy is usually greater than 97%. Heading information is determined from the nine-axis attitude fusion of accelerometers, gyroscopes, and magnetometers introduced in Chapter 4. With proper initial calibration, the accuracy of pitch, roll, and heading errors are within 10 degrees using 9-axis fusion algorithms in several three dimensional rotation tests.
3. Thirdly, two alternative positioning algorithms are developed for indoor positioning. Wi-Fi positioning can provide good horizontal location updates during GPS outages. By modeling the radio propagation behaviors in different indoor scenarios, a universal path loss model for indoor

ranging estimation was developed to fit both LOS and NLOS cases. This approach can circumvent the conventional fingerprint approach where intensive site survey is required. According to the second prototyping test results in Chapter 6, by using 12 surveyed access point locations, Wi-Fi indoor positioning can provide position updates for approximately 50% of the indoor trajectory in the campus walking test, within 20 meters of error. Vertically, the barometer is a good source to derive relative height changes. Once the barometer bias is calibrated from GPS height, the fusion algorithm for calculating vertical position can be used to determine absolute height. From the field test, the height accuracy can be within three meters in multi-floor buildings, which is enough to determine which floor of a building someone is on.

4. Finally, an Extended Kalman Filter (EKF) is built to integrate MEMS-sensors-based Pedestrian Dead Reckoning (PDR) with GPS and Wi-Fi. The Singular Value Decomposition (SVD) of a stripped observability matrix is the most effective approach to determine the estimation states in the Kalman filter. It not only judges the system observability but also provides a detailed degree of observability for each state. From the theoretical analysis and field tests, a 9-axis sensor fusion is the best configuration to keep track of a user's orientation changes. In addition, portable navigation systems can be simplified to 6-state magnetometer dead reckoning with GPS integration for outdoor environments and a 6-state gyro EKF for magnetically disturbed indoor places. Three independent field tests are given using three prototypes developed at different research stages. From the test results, for a 10-15 minute pedestrian test in GPS-denied areas, the system can provide a continuous navigation solution while maintaining positioning accuracy no worse than 25 meters rms. The accuracy per se is not the most outstanding result, compared to the best results listed in the literature review; however, the field tests represent practical use cases because with more variable routes that include indoor

turns, walking up/down stairs, and more. This thesis work has been performed as a practical exercise for today's cost-effective implementations. The system fits well for a variety of positioning applications in the mass market, such as E-911, personnel monitoring, asset tracking, and many other location-based services.

7.2 Contributions

The above section summarizes the main thesis work and results. Now, revisiting the thesis contribution and hypothesis set in Table 1-2 of the Chapter one, and then synthesize the thesis development from each chapter, the main thesis contribution and uniqueness are summarized in Table 7-1 below.

Table 7-1 Thesis contribution and uniqueness

Contribution	Uniqueness
1. Analyze low-cost MEMS sensors error sources; then apply error modeling and calibration methods for estimation.	<ul style="list-style-type: none"> - Based on the MEMS gyro circuitry design and analysis, build error models suitable for Kalman filter. - Design efficient on-line gyro and magnetometer calibration methods to reduce the major sensor errors.
2. Develop algorithms for 3/6/9-axis motion sensors fusion for attitude determination.	- A unified sensors fusion framework to switch between 3-axis gyro only, 6-axis acc+mag or 6-axis acc+gyro and 9-axis acc+mag+gyro based on input signal quality to maintain performance and minimize power consumption.
3. Apply observability analysis for pedestrian dead reckoning integration with GPS/WiFi measurement.	<ul style="list-style-type: none"> - Given pedestrian dynamic for low-lost navigation sensors fusion, explore the most effective Kalman filter state selection based on observability analysis. - Show quantitative results of degree-of-observability for each state and its impact to personal navigation.
4. Build a solution framework with 10-axis MEMS sensors, GPS and Wi-Fi, the system will adapt different subsystem according to application scenarios.	<ul style="list-style-type: none"> - The hybrid positioning framework can perform MEMS/GPS/WiFi fusion with full or partial sensors, at different sensor grade. - Three prototypes were demonstrated under different field application scenarios using the same framework.

7.3 Recommendations for Future Work

Based on the results and conclusions of this thesis research, the following are recommendations to extend the research for further development:

1. There is something unique about human movement that makes personal navigation different and more challenging than other types of navigation: personal navigation implies frequent changes of speed and orientation. Also, position cannot be constrained to predefined tracks (e.g. roads) like it can with automobile navigation. Mobile devices, by definition, can often be placed in positions that are difficult to predict. Mobile devices also have different application modes that can alter frequently depending on what the user is doing, like walking, running, driving, cycling, etc. Consequently, user mode detection and context awareness are very helpful information to have for navigation. This thesis recommends improved mode pattern recognition algorithms be developed to better identify the users current activity context.
2. Currently, navigation solutions are mainly used to find the fixed placement of the navigation device with a typical alignment, such as when the unit is placed on the user's belt or held in hand in the landscape or portrait orientation. In practical usage, the unit can be placed more randomly, including in hand and dangling, inside a pant pocket, in a handbag, or in other unconventional places on the body. Under these situations, sensor misalignment error may be more severe, so a fast and effective estimation method is needed to identify and compensate for the additional misalignment error associated with random placements.

3. More alternative positioning methods can be explored for GPS denied places. For example, besides Wi-Fi positioning systems, bluetooth beacon positioning systems have become more popular because of the wide acceptance of it as a standard. Also, instead of an RSSI-based positioning mechanism, other mechanisms based on Time Difference Of Arrival (TDOA) or wireless signal fingerprinting can potentially provide higher accuracy. In addition, feature matching based positioning techniques are attractive for some deep indoor scenarios where GPS and wireless infrastructures are unavailable. In these scenarios, map matching or camera vision matching may be needed to provide MEMS sensors a proper initial absolute location and/or provide constant correction updates.

4. Finally, integration of various low-cost systems into a real product, with different positioning sub-systems and applications, is recommended for future exploration. This thesis work presents three dedicated prototypes to prove the concept, but these prototype configurations will be different from the final product when a more compact form factor is adopted. A more compact form factor is required to fit the system in a smartphone or wearable devices with GPS, wireless connectivity, and MEMS sensor integration. Power consumption and cost reduction are also important design aspects to be considered. More sophisticated system optimization and algorithm tuning are required to leverage the ideas of this thesis for practical deployment.

References

Agilent [2013] GNSS Technologies and Receiver Testing - Application Note, Agilent, May 2013.

Antonello [2011] Antonello, R. and Oboe R., Microsensors, Publisher: InTech, 2011.

Ali [2013] Ali, A., Chang, H-W., Georgy, J., Syed, Z., Goodall, C., "Heading Misalignment Estimation between Portable Devices and Pedestrians," ION GNSS, Nashville, TN, September 2013.

Attia [2013] M. Attia, A. Moussa and N. El-Sheimy, "Map Aided Pedestrian Dead Reckoning Using Buildings Information for Indoor Navigation Applications," Positioning, Vol. 4 No. 3, 2013.

Ayazi [2011] Ayazi, F., "Multi-DOF Inertial MEMS: from gaming to dead reckoning, " Transducers, 2011.

Bahl et al., [2000] Bahl, P. and Padmanabhan, V.N., "RADAR: an in-building RF-based user location and tracking system, " in: Proceedings of the Nineteenth Annual Joint Conference of the IEEE Computer and Communications Societies, INFOCOM 2000, vol. 2, 2000.

Bar-Itzhack [1985] Bar-Itzhack, I. Y., and Oshman, Y., "Attitude Determination from Vector Observations: Quaternion Estimation, " IEEE Transactions on Aerospace and Electronic Systems, Vol. AES-21, 1985.

Bensky [2008], Bensky, A., Wireless Positioning Technologies and Applications, Artech House, 2008.

Bhushan [2010] Bhushan, B. Introduction to Nanotechnology, Springer Handbook of Nanotechnology, 2010.

Bicking [1998] Bicking, R. E. Fundamentals of Pressure Sensor Technology, Sensors Magazine, Nov., 1998.

Bosch [2012] Bosch BMP280 product, accessible at http://www.bosch-sensortec.com/en/homepage/products_3/environmental_sensors_1/bmp280/bmp280 , 2012

Bosch [2013] Bosch BMX055 product, accessible at http://www.bosch-sensortec.com/en/homepage/products_3/9_axis_sensors_5/ecompass_2/bmx055_1/bmx055 , 2013

Bullock, J. B. [2012], Chowdhary, M., Rubin, D., Leimer, D., Turetzky, G., Jarvis, M., "Continuous Indoor Positioning Using GNSS, Wi-Fi, and MEMS Dead Reckoning," Proceedings of the 25th International Technical Meeting of The Satellite Division of the Institute of Navigation , Nashville, TN, Sept. 2012.

Caruso [1998] M.J.Caruso, T.Bratland, C.H.Smith, R.Schneider, "A New Perspective on Magnetic Field Sensing, "Sensors Expo Proceedings, Oct. 1998.

Chiang [2011] Chiang Chia-Fang, Graham, A.B., Messana, M.W., Provine, J., Buchman, D.T., O'Brien, G.J., Kenny, T.W., "Capacitive absolute pressure sensor with independent electrode and membrane sizes for improved fractional capacitance change," Solid-State Sensors, Actuators and Microsystems Conference (TRANSDUCERS), 2011 16th International , June 2011.

Cho [2006] Cho S.Y., Choi W.S., "Performance Enhancement of Low-Cost Land Navigation System for Location-Based Service," ETRI Journal, Vol. 28, No.2, Apr. 2006.

Crassidi [2004] J.L. Crassidis and J.L. Junkins, Optimal Estimation of Dynamic Systems , Chapman & Hall/CRC, 2004.

Diebel [2006] Diebel, J. , "Representing attitude: Euler angles, unit quaternions, and rotation vectors, " Technical Report, University of Stanford, Mar, 2006.

Ekahau [2010] Ekahau, accessible at <http://www.ekahau.com/> , Nov. 2010.

El-Sheimy [2007] El-Sheimy,N.,Niu,X., "The promise of MEMS to the navigation community",Inside GNSS, Invited Paper, Mar./Apr. 2007

El-Sheimy [2008] El-Sheimy, N., H. Hou and X. Niu, "Analysis and Modeling of Inertial Sensors Using Allan Variance, "IEEE Transactions on Instrumentation and Measurement, 57(1), 2008.

El-Sheimy [2009] El-Sheimy, N., ENGO 623 Course Lecture Note, University of Calgary, Canada, 2009.

FCC [2014], FCC Commission Document, accessible at <http://www.fcc.gov/document/proposes-new-indoor-requirements-and-revisions-existing-e911-rules> , 2014.

Farrell [2008] Farrell, J.A., Aided Navigation: GPS with High Rate Sensors, New York: McGraw-Hill, 2008.

Frank [2009], Frank K., Krach B., Catterall N., Robertson P., "Development and Evaluation of a Combined WLAN & Inertial Indoor Pedestrian Positioning System, "Proceedings of the 22nd

International Technical Meeting of The Satellite Division of the Institute of Navigation, Sept. 2009.

IEEE [2008] IEEE Std 952™-1997 (R2008) IEEE Standard Specification Format Guide and Test Procedure for Single-Axis Laser Gyroscopes, IEEE, 2008.

Foxlin, E. [2005], "Pedestrian Tracking with Shoe-Mounted Inertial Sensors, "IEEE Computer Graphics and Applications, Vol. 25, No. 6, 2005.

GCM [1996], NGA WGS 84 Geoid Calculator, accessible at http://earth-info.nga.mil/GandG/wgs84/gravitymod/wgs84_180/intptW.html , 1996.

Gebre [2006] D. Gebre-Egziabher, G.Elkaim, J. Powell, B. Parkinson , "Calibration of Strapdown Magnetometers in Magnetic Field Domain," ASCE Journal of Aerospace Engineering, Vol. 19, No. 2, 2006.

Gezici [2008], Gezici S., "A Survey on Wireless Position Estimation," Wireless Personal Communications, Vol. 44, No. 3, 2008.

GPS [2014] Official U.S. Government information about the Global Positioning System (GPS), accessible at <http://www.gps.gov/multimedia/images/constellation.jpg> 2014.

Godha [2006] S Godha and G Lachapelle,"Foot mounted inertial system for pedestrian navigation," Measurement Science Technology, 2008.

Gonzalo Seco-Granados [2012], "Challenges in Indoor Global Navigation Satellite Systems, " IEEE Signal Processing Magazine, Mar. 2012.

Goodall [2012], Goodall, C., Carmichael, S., El-Sheimy, N. and Scannell, B., "INS Face Off MEMS versus FOGs," Inside GNSS, Jul. / Aug., 2012.

Grejner-Brzezinska [2008], Grejner-Brzezinska, D.A.; Toth, C.; Moafipoor, S., "A Step Ahead: Human Motion, Machine Learning Combine for Personal Navigation, " GPS World, Vol. 19, No. 11, 2008.

Grewal [2008] S. Grewal, A. Andrews, Kalman Filtering, Theory and Practice Using Matlab, 3rd ed. Publish by John Wiley & Sons, 2008.

Groves [2008], Groves P., Principles of GNSS, Inertial, and Multisensor Integrated Navigation Systems, Artech House, 2008.

GSM [2003] 3GPP: the current standardization body for GSM, accessible at <http://www.3gpp.org> , 2003.

G-M [1992-1], Goshen-Meskin, D.,Bar-Itzhack, I.Y., "Observability Analysis of Piece-Wise Constant Systems-PartI: Theory", IEEE Transaction on Aerospace and Electronic Systems, Vol.28,No.4, Oct. 1992.

G-M [1992-2], Goshen-Meskin, D.,Bar-Itzhack, I.Y., "Observability Analysis of Piece-Wise Constant Systems-PartII: Application to Inertial Navigation In-Flight Alignment, " IEEE Transaction on Aerospace and Electronic Systems, Vol.28,No.4, Oct. 1992.

Ham [1983], Ham, F.M., Brown, R.G. (1983), "Observability, Eigenvalues, and Kalman Filtering," IEEE Transaction on Aerospace and Electronic Systems, Vol.1, No.2, Mar.1983.

Honeywell [2003] magnetometer max/min method from Honeywell Application Note 2003.

Invensense [2011] Invensense, MPU-6000/MPU-6050 Product Specification, accessible at <http://www.invensense.com/mems/gyro/mpu6050.html> , 2011.

Invensense [2012] Invensense, MPU-9150 Product Specification, accessible at <http://www.invensense.com/mems/gyro/mpu9150.html> , 2012.

Kempe [2011] Kempe, V., Inertial MEMS Principles and Practice, Cambridge University Press, 2011.

Klema [1980], Klema, V. C. , Laub, A. J., "The singular value decomposition: Its computation and some applications", IEEE Trans. Autom. Control, vol. AC-25, no. 2, Apr. 1980.

Kuniper [1999] J. B. Kuniper, Quaternions and Rotation Sequences: A Primer with Applications to Orbits, Aerospace and Virtual Reality, Princeton University Press, 1999.

Kwakkel [2008] Kwakkel,S.P., Lachapelle, G., Cannon, M.E., , "GNSS Aided In Situ Human Lower Limb Kinematics During Running", Proceedings of the 21st International Technical Meeting of the Satellite Division of The Institute of Navigation, Sep. , 2008.

Lachapelle [2001] Lachapelle, G. , Advanced GPS Theory and Applications, ENGO 625 Course Lecture Notes, University of Calgary, Canada, 2001.

Langley [2014] Langley, R., "Orbit Data and Resources on Active GNSS Satellites," GPS World, Jan. 2014.

Liu [2012] Liu, Chang, Foundations of MEMS, Second Edition, Pearson Education, Inc., 2012.

MacGougan [2003], MacGougan, G. , High Sensitivity GPS Performance Analysis in Degraded Signal Environments, MSc Thesis, Department of Geomatics Engineering, University of Calgary, 2003.

Markley [2003] F. L. Markley, "Attitude Error Representations for Kalman Filtering", Journal of Guidance, Control, and Dynamics, Vol. 26, No. 2, 2003.

Markley [2004] F. L. Markley, "Multiplicative vs. Additive Filtering for Spacecraft Attitude Determination," 6th Cranfield Conference on Dynamics and Control of Systems and Structures in Space, Cranfield University Press, UK, 2004.

Markley [2008-1] F. L. Markley, "Unit Quaternion from Rotation Matrix," Journal of Guidance, Control, and Dynamics , Vol. 31, No. 2, Mar.-Apr. 2008.

Markley [2008-2] F. L. Markley, "Optimal Attitude Matrix from Two Vector Measurements," Journal of Guidance, Control, and Dynamics , Vol. 31, No. 3, May–June 2008.

Markley [2008-3] F. L. Markley and J. E. Sedlak, "Kalman Filter for Spinning Spacecraft Attitude Estimation," Journal of Guidance, Control and Dynamics, 2008.

Moafipoor [2008], Moafipoor, S., Grejner-Brzezinska, D. A. and Toth, C. K., "Multi-Sensor Personal Navigator Supported by Adaptive Knowledge Based System: Performance Assessment, " Position, Location and Navigation Symposium, 2008 IEEE/ION, 2008.

Mohamed [2012] A. Mohamed and A. Mamatas, Fundamentals of GNSS-Aided Inertial Navigation, Automatic Flight Control Systems - Latest Developments, Dr. Thomas Lombaerts (Ed.), InTech, Dec. 2013.

Mohri [1995] K.Mohri, K.Bushida, M.Noda, H.Yoshida, L.V.Panina, T.Uchiyama, "Magneto-Impedance Element," IEEE Transaction on Magnetics, Vol.31, No.4, 1995.

Nasiri [2011] Nasiri,S.,Lim M.,Housholder M., "A Critical Review of the Market Status and Industry Challenges of Producing Consumer Grade MEMS Gyroscopes", Invensense White Paper, 2011.

NetStumbler [2010] Net Stumbler, Software accessible at <http://www.netstumbler.com> , Nov. 2010.

Novatel [2010] Novatel LCI Product brief, accessible at <http://novatel.com/assets/Documents/Papers/LCI.pdf> , 2010.

Nguyen [2012] Nguyen, C., EE245 Lecture Notes on MEMS design, UC Berkeley, USA, 2012.

O'Keefe [2008], K. O'Keefe, ENGO585 Course Lab Notes, University of Calgary, Canada, 2008.

Parviainen [2008], Parviainen, J. Kantola, J. Collin, J. [2008], "Differential barometry in personal navigation," Position, Location and Navigation Symposium, 2008 IEEE/ION, May 2008.

Petovello, M. [2003] Real-Time Integration of a Tactical-Grade IMU and GPS for High-Accuracy Position and Navigation, Ph.D. thesis, University of Calgary, Canada, 2003.

Petovello, M. [2009], ENGO699.18 Course Lab Note, Department of Geomatics Engineering, University of Calgary, Canada, 2009.

Qin [2006], Qin, Y., Inertial Navigation, Science Press, 2006.

Rappaport[2002], Rappaport T.S., Wireless Communications Principles and Practices, 2nd ed. Upper Saddle River, NJ: Prentice Hall, 2002.

Ristic [2012], Ristic Lj., "Sensor fusion and MEMS for 10-DoF solutions, " EE Times, accessible at http://www.eetimes.com/document.asp?doc_id=1279870 , Sep. 2012.

Sabatini [2006] A.M. Sabatini, "Quaternion-based extended Kalman filter for determining orientation by inertial and magnetic sensing, "IEEE Transactions On Biomedical Engineering; N. 53, 2006.

Sabatini, A. M. [2008], "Adaptive Filtering Algorithms Enhance the Accuracy of Low-Cost Inertial/Magnetic Sensing in Pedestrian Navigation Systems, "International Journal of Computational Intelligence and Applications, Vol. 7, No.3, 2008.

Samama [2008], Samama, N., "Global positioning: technologies and performance," John Wiley & Sons publish, 2008.

Samuels [1996] Samuels,H., "Single- and Dual-Axis Micromachined Accelerometers, " Analog Dialogue Volume 30, Number 4, 1996.

Schuhmann [2008], Schuhmann S., Herrmann K., Rothermel K., Blumenthal J., Timmermann D., Improved Weighted Centroid Localization in Smart Ubiquitous Environments, Ubiquitous Intelligence and Computing, Springer Berlin, 2008.

Seco-Granados [2012], G. Seco-Granados, J. Lopez-Salcedo, D. Jimenez-Banos, and G. Lopez-Risueno, "Challenges in indoor global navigation satellite systems: unveiling its core features in signal processing," IEEE Signal Processing, Magazine, vol. 29, no. 2, Mar. 2012.

Senturia [2001] Senturia, Stephen D. Microsystem Design. Boston, MA: Kluwer Academic Publishers, 2001.

Shaeffer [2013] Shaeffer, D. K., "MEMS inertial sensors: A tutorial overview, " IEEE Communications Magazine 51(4), 2013.

Sharma [2007] A. Sharma, M. F. Zaman, and F. Ayazi, "A 104 dB dynamic range transimpedance-based CMOS ASIC for tuning fork microgyroscopes," IEEE Journal of Solid-State Circuits, 2007.

Sharma [2008] K. Sharma, I. Macwan, L. Zhang, L. Hmurcik, X. Xiong, "Design Optimization of MEMS Comb Accelerometer", American Society for Engineering Education Zone 1 Conference, Mar. 2008.

Shin [2005], Shin, E.H., "Estimation Techniques for Low-Cost Inertial Navigation", Ph.D. thesis, University of Calgary, May 2005.

Shuster [1993] M. D. Shuster, "A Survey of Attitude Representations," The Journal of the Astronautical Sciences, Vol. 41, No. 4, Oct.–Dec. 1993.

Skyhook [2014] Skyhook, accessible at <http://www.skyhookwireless.com/coverage-map>, Nov. 2014.

Soehren, W., Hawkinson, W. [2008], "A Prototype Personal Navigation System, "Aerospace and Electronic Systems Magazine, IEEE, Vol. 23, No.4, 2008.

STM [2010] ST Microelectronics, L3G4200D product introduction, accessible at http://www.st.com/web/catalog/sense_power/FM89/SC1288/PF250373 , 2010.

STM [2011] ST Microelectronics Datasheet, LSM330DLC iNEMO inertial module: 3D accelerometer and 3D gyroscope , 2011.

STM [2012] ST Microelectronics, LPS331 product introduction, accessible at http://www.st.com/web/catalog/sense_power/FM89/SC1316/PF251601 , 2012.

STM [2013] ST Microelectronics Press Release, accessible at <http://www.st.com/web/en/press/t3408> , 2013.

STM [2013-2] ST Microelectronics Datasheet, LSM9DS0 iNEMO inertial module: 3D accelerometer, 3D gyroscope, 3D magnetometer, 2013.

Syed [2009], Syed Z. F., Design and Implementation Issues of a Portable Navigation System, Ph.D. thesis, University of Calgary, Feb. 2009.

Sye [2013], Syed, Z.; Georgy, J.; Ali, A.; Chang, H.-W.; and Goodall, C. , "Showing Smartphones the Way Inside Real-time, Continuous, Reliable, Indoor/Outdoor Localization, " GPS World, , Vol. 24, No. 3, Mar. 2013.

Tomé [2008], Tomé ,P. and Yalak, O., "Improvement of orientation estimation in pedestrian navigation by compensation of magnetic disturbances, " Journal of The Institute of Navigation, Vol. 55, No. 3, 2008.

Wan [1998] , Wan, D., Pang, J. (1998), Initial Alignment of Inertial Navigation System , Southeast University Press, China, 1998.

Xing [2008] Xing, Z. and Gebre-Egziabhe,Demoz, "Modeling and Bounding Low Cost Inertial Sensor Errors," Position, Location and Navigation Symposium, 2008 IEEE/ION, 2008.

Yazdi [1998]Yazdi N., Ayazi F. and Najafi K. , "Micromachined Inertial Sensors, " Proceedings of the IEEE, Vol. 86, No. 8, Aug. 1998.

Yole [2013] Yole Développement, "New Technologies for the Next-Generation Inertial MEMS, " Webinar, Nov. 2013.

Yoshinaga [2010] Yoshinaga,T. and Nomura,M. , "Trends in R&D in TSV Technology for 3D LSI Packaging, " Science & Technology Trends - Quarterly Review No.37 Oct. 2010.

Younis [2011] M.I. Younis, MEMS Linear and Nonlinear Statics and Dynamics, Springer 2011.

Zhang [2004] Zhang, T., Wang, B.,Han, Z., Li, J. , "Analysis on Observability of SINS/GPS, " Proceedings of 5th World Congress on Intelligent Control and Automation, June 2004.

Zhang [2012] Zhang, X., Deng, J., Zhao, X., Jia, Z., "A Smartpower Hybrid Positioning System," Proceedings of the 25th International Technical Meeting of The Satellite Division of the Institute of Navigation , Nashville, TN, Sep. 2012.

Zhao [2009] Zhao, X., Syed, Z., Wright, B., El-Sheimy, N., "An Economical and Effective Multi-sensor Integration for Portable Navigation System," Proceedings of the 22th International Technical Meeting of the Satellite Division of the Institute of Navigation, Sept. 2009.

Zhao [2010] Zhao, X., Goodall, C., Syed, Z., Wright, B., El-Sheimy, N., "Wi-Fi Assisted Multi-sensor Personal Navigation System for Indoor Environments," Proceedings of the 2010 International Technical Meeting of The Institute of Navigation, Jan. 2010.

Zhao [2011] Zhao, X., "Multi-Sensors Observability Analysis on Pedestrian Navigation System," Proceedings of the 24th International Technical Meeting of the Satellite Division of the Institute of Navigation, Sept. 2011.

APPENDIX A: MEMS SENSORS FABRICATION

MEMS sensor technology is the combination of intrinsic microsensor elements, microactuator, signal-processing, and analog to digital interface blocks. MEMS sensors convert the forces caused by the acceleration or rotation input into some physical changes such as deflection of masses or derivations of stresses, which are then captured by a corresponding transducer and transformed into an electrical signal. The most frequently used transducers in MEMS are capacitors with comb or plate shapes. The piezoresistive or piezoelectric devices also play a significant role. All the above implementation is coupled with some resonance excitations of the mechanical structure, which results in high sensitivity and performance [Kempe 2011]. A brief overview of MEMS fabrication is first introduced, as it is relevant to the shape and other properties of the MEMS sensors; the detailed technologies, however, are beyond the scope of this thesis.

MEMS development stems from the microelectronics industry combining with the conventional techniques developed for integrated circuit (IC) processing, and then it is extended to MEMS specific processes. Referring to FigureA-1, the device fabrication consists of two phases:

- The **front-end process** in the top row involves the fabrication of structures and elements on the silicon wafer, there are three iterative building blocks:
 1. Deposit thin films of material on a substrate.
 2. Transfer a patterned mask on top of the films by photolithographic imaging.
 3. Etch the films selectively to the mask.
- The **back-end process** given in the bottom row, which involves die preparation from wafer dicing, die testing, packaging, and assembly of individual silicon chips.

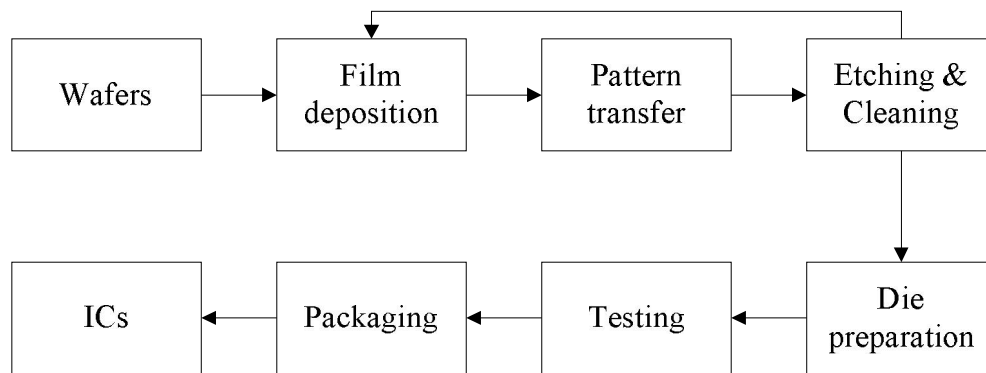


Figure A-1 From wafer to IC: basic fabrication process

More than standard IC fabrication, MEMS fabrication focuses on the mechanical properties, especially for material used to form the mechanical structures of the sensors. This includes structures such as beams, suspended bridges, cantilevers, and membranes etc. One of the basic building blocks in MEMS processing is the ability to deposit films of material having a thickness between a few nanometers and about 100 μm [Liu 2012], which is generally thicker than conventional IC. Depending on the material deposited there are many different deposition processes including Physical Vapour Deposition (PVD) techniques and Chemical Vapour Deposition (CVD) techniques. Usually MEMS fabrication requires deeper etching and thicker deposition of materials with a high aspect ratio for better mechanical performance, such as high sensitivity and signal-to-noise ratio.

Photolithography is a process step that uses light to transfer a geometric pattern to the substrate surface. It is a critical step to get the shapes of the microstructures. With this process it is possible to selectively remove or add parts of material to the substrate. For MEMS devices with movable parts, a unit process is required to release the movable parts from the substrate. If the target object is embedded in a silicon substrate, it can be released by bulk micromachining,

where bulk material of the substrate is selectively etched away. Alternatively, in the modern process, surface micromachining can be used. A mechanical oxide layer known as the sacrificial layer is deposited first to act as a temporary mechanical layer onto which the actual device layers are built; subsequently, a thin film layer of polysilicon is deposited and patterned and this layer is the structural mechanical layer; lastly, the temporary sacrificial layer is removed thereby allowing the structural layer to move. There are two classes of etching processes: wet etching where the material is dissolved when immersed in a chemical solution; dry etching where the material is sputtered or dissolved using reactive ions or a vapor phase etchant.

A MEMS chip typically contains moving parts that must be protected in a stable environment in terms of external vibration, particles, variation on humidity, temperature, pressure etc. Therefore, an encapsulation process is of particular concern, which contributes a significant portion of the overall cost. Through Silicon Via (TSV) is an enabling packaging technology that allows electrical connections between the MEMS die and other ASICs to be formed through a silicon wafer or multi-wafer devices [Yoshinaga 2010]. Hereby chips are stacked vertically with electrical contacts through the silicon to minimize electrical path lengths and thus enhance the electrical and thermal performance. This also minimizes the chip size and parasitic capacitances. Electrical connections through a silicon wafer allow for reduced die footprints and interlayer connectivity. TSVs minimize die size, allow conventional or flip-chip bonding, and help minimize the cost of the final device. Another efficient packing approach invented by InvenSense in its proprietary Nasiri fabrication platform builds the CMOS and MEMS processes on separate dies and then bonds them together, face-to-face in a small, cost effective standard package [Nasiri 2011]. This approach reduces the number of MEMS manufacturing steps,

supports wafer-level testing hence reducing back-end packaging and testing costs, and improves yield.

To sum up, MEMS technology offers a complete sensor solution and supports electronics on a single integrated circuit chip. Many techniques and materials used in IC fabrication are reused in MEMS fabrication for the advantages of low cost, high reliability, and performance. However, MEMS fabrication is still different from IC fabrication in some aspects. The uniqueness of MEMS devices and processes requires a customized design and fabrication process techniques for different products. Going forward we see a clear trend for smaller, more cost effective MEMS devices. But MEMS size reduction cannot last forever. For example in an inertial sensor, a minimal mass is needed for motion detection. Nowadays, die size reduction is mostly achieved by packaging innovation that adds extra manufacturing cost but reduces die size.

APPENDIX B: MEMS SENSORS OPERATION PRINCIPLE

MEMS sensors have improved rapidly over the past three decades, primarily due to the advancement made in the evolution of microelectronics fabrication and reduced sensitivity on the packaging. In addition to the expected technological improvements such as size minimization and power reduction, two additional significant breakthroughs have impacted sensor development:

- Three orthogonal axes of MEMS gyroscopes, accelerometers and magnetometers, and barometer can now be fabricated on a planar substrates integrated circuit. This greatly reduces manufacturing and assembly costs. In precise positioning applications, for example, MEMS gyro becomes a good candidate that was previously dominated by fiber optic gyroscopes (FOG) [Goodall 2012]; but the cost of MEMS system was less expensive than FOG navigation system by an order of two.
- Key performance metrics of MEMS sensors such as resolution, sensitivity, biases, and power consumption have improved by an order of magnitude during the decade [El-Sheimy 2007]. This is due to the development of IC processes, new materials, MEMS structural design, integrated circuitry design, and advanced digital signal processing. As a result, inexpensive MEMS sensors have reached automotive-grade standards and will likely continue advancing to penetrate standards for low-end tactical-grade uses in the near future.

To meet the requirements of motion tracking in navigation, a ten degrees-of-freedom fusion of three-axis accelerometers, three-axis gyroscopes, three-axis magnetometers, and a barometer are applied to measure three dimensional rotation, acceleration, and altitude. As measurement errors

inherently exist in sensor output, many trade-offs are considered to meet application specifications. Therefore, a thorough understanding of MEMS sensor design and operation mechanism are essential for navigation system design and they are introduced in details in this appendix.

B.1 MEMS Sensors: State-of-the-art and Future Trend

Traditionally, MEMS sensors have been predominantly used in the automotive, industrial, and medical sectors. The recent availability of low cost, compact sized, and low power MEMS sensors have made these devices proliferate into consumer applications such as smartphones, tablets, gaming consoles, and wearable devices. Yole Développement estimated the inertial MEMS sensors industry will reach \$5.4 billion by 2018, up from \$4 billion in 2013 [Yole 2013]. MEMS technologies and applications are quite diverse, among their applications navigation emerges as a must-have feature in many modern devices. Combining MEMS accelerometers with gyroscopes, magnetometers, and a barometer allows for accurate computation of the position, velocity, acceleration, and altitude of the device. Integrating these with a GNSS receiver in the device empowers seamless outdoor and indoor navigation to become a reality. This section presents an overview of the current MEMS sensors status and its technological trends.

Fuelled by the rapid development of consumer electronic applications and MEMS technology, silicon MEMS-based sensors are no longer too expensive for consumer electronics and there prices have fallen into an acceptable range for wide spread adoption in the consumer market. First and foremost, the trend that all MEMS sensors have in common is a continuous improvement in performance, cost, power consumption, and package size. In 1998 Yazdi pointed

out that MEMS performance enhancement had improved by a factor of 10 every two years since 1991[Yazdi 1998]. Though this speed has slowed down in the 2000s, MEMS inertial sensors have since been improving by one to two orders-of-magnitude in key performance areas like noise and power consumption. The improvement was mainly driven by higher precision micro-fabrication, reduced sensitivity to packaging, new MEMS structure design, and more advanced electronics and signal processing.

Table B-1 Comparison of IMU performance

Unit Parameter	Tactical-grade	High-end MEMS	Low-end MEMS
Gyro bias stability (°/hr)	<1.0	~10	10-100
Gyro ARW (° / √ hr)	~0.05	~0.6	1-10
Gyro nonlinearity (% of full scale)	~0.01	~0.1	~0.2
Acc. VRW (mg/ √ hz)	N/A	0.1	0.2-0.6
Acc. nonlinearity (% of full scale)	~0.025	~0.2	~0.5
Power (Watt)	~10	0.1-1	~0.01
Size (mm*mm*mm)	168 x 195 x 146	24x 38x 10	4*4*1
Cost (US\$)	~10,000	100-500	1-3
Application	Ground or airborne survey	Inertial navigation; Robotics	Mobile devices; Gaming

Table B-1 compares the key performance parameters of some cutting-edge Inertial Measurement Units (IMUs) that emerged during 2010-2012. It breaks down IMU devices into three categories:

- **Tactical grade IMUs**, which consist of fiber optic gyroscopes and high-end micromechanical accelerometers. These parameters mainly reference Novatel's LCI IMU, originally designed by Northrop-Grumman Litef GMBH [Novatel 2010]. Companies like Honeywell and KVH have the tactical Ring Laser Gyro with similar performance.
- **High-end MEMS**, whose performances approach tactical-grade IMU but are available at a more affordable price. ADI's ADIS16445 [ADI 2012] was mainly referenced as an example of this type. Others vendors, such as Silicon Sensing and Intersense have provided similar products as well.
- **Low-end MEMS** refers to those tiny ICs used for mobile devices. Obviously they have great advantages in terms of cost, power consumption, size, and weight. The 6-axis inertial module MPU6050 from Invensense [Invensense 2011] and LSM330DLC model from ST Microelectronics [STM 2011] were referenced as examples representing the leading edge of this category as of 2011, but later on more vendors came up with comparable products. Clearly, the low-end MEMS sensors are the most cost-effective solution, thus they are the first choice for the majority of the consumer products. Tactical and high-end MEMS IMUs maintain a niche in areas where high performance is required.

Another trend is to integrate multiple types of MEMS sensors in a single package. Starting from 2011, leading sensor manufacturers began proposing combinations of discrete devices: 6-axis e-compasses (accelerometer plus magnetometer), 6-axis Inertial Measurement Units (IMU) combos (accelerometer plus gyroscope), and 9-axis combo solution (gyroscope plus e-compass).

For instance, ST Microelectronics [STM 2013-2] launched LSM9DS0 in a 4x4x1 mm system-in-package featuring a 3-axis gyroscope, a 3-axis accelerometer and a 3-axis magnetometer function on the same die. This new structure, combined with an Au-Au hermetic bonding process allows ST to shrink the space required by the 6-axis function by more than 35%. For another example, the MPU-9150 is a motion tracking MEMS that combines a 3D accelerometer, a 3D gyroscope from Invensense [Invensense2012], and a 3D digital compass from AKM in the same package: a 4x4x1mm LGA package. Bosch [Bosch 2013] also brought a 9-axis sensor BMX055 to market. It can be predicted that sensing technology, such as pressure, humidity, temperature, and ambient light, will be integrated into combo units in the future. Although multimode sensor integration faces many technological challenges in assembly, packaging, and testing, yet the benefits in cost and size improvements will ultimately pay off.

MEMS sensor development is driven by different waves of new applications. Gaming consoles were the first wave boosting sensor usage in consumer electronics. LBS was the second wave as focused on in the thesis. Looking ahead, the Internet of Things (IOT) might be the next wave.

This wave will be widely applied everywhere, from wearable electronics to medical care systems, and from intelligent traffic to environment monitoring systems. Therefore, MEMS sensors will see a transition from a single measurement solution to a total, comprehensive solution. As such, some of the latest ICs have already expanded their features and include some sensors fusion processing capabilities on chip. Many sensor tasks like context detection, activity recognition, online sensor calibration and motion tracking need to occur continuously in the background. In addition, implementing sensor processing in the applications processor is expensive in terms of battery life. Recently, the concept of a sensors hub has become popular, first seen in the Galaxy S4 and iPhone 5S in 2013. A sensor hub is a processing element that can

be dedicated to dealing with real-time demands from sensors; it can be implemented either from a low-power microcontroller or even inside a sensor IC, supposing some memory and an embedded processor are available on chip.

Finally, new MEMS sensor types are emerging and the underlying technology is still evolving rapidly. Among them, non-intrusive infrared (IR) proximity sensors for proximity sensing are very popular. These can detect bodies in the vicinity of the device and are perfectly used on smartphones. Active light sensors can provide the ambient light intensity within a certain measurement distance. The combination of air pressure, humidity, temperature sensors, ultraviolet sensor and gas sensor provides a finer granularity of the local environment and location awareness, offering environment context useful for navigation.

B.2 Sensor Operation Principle

Many sensor providers have different manufacturing approaches, even for the same type of sensor. For example, magnetometer design processes are radically different. Therefore the MEMS industry is very fragmented and MEMS in general do not follow the same roadmap that the semiconductor industry does. This section gives an overview of mainstream MEMS sensor technologies that can be used for navigation.

B.2.1 Accelerometers

Most MEMS accelerometer designs apply some variant of Newton's Second Law of motion:

$F = ma$, to sense the response of an inertial mass (also known as proof mass).

An accelerometer consists of two electrodes – a moveable electrode (the inertial mass) and a fixed electrode. Under acceleration, the proof mass will be deflected by the accelerating force, and this deflection may be detected.

Many sensing principles, including piezoresistive, silicon capacitive, piezoelectric, and thermal flow, have been developed for acceleration measurements. Up to now, silicon capacitive accelerometers have largely dominated the market. Capacitive sensing is based on detecting small changes in capacitance due to relative displacement of the proof mass. Compared to the other types of MEMS accelerometers, capacitive accelerometers have high sensitivity, low power consumption, low noise level, stable DC characteristics and less temperature dependence. In addition, Integrating with CMOS sensing circuits is much easier for capacitive accelerometers, due to their simple structures and fabrication processes. Therefore, capacitive sensing mechanisms became the most popular selection.

The fundamental behavior of an accelerometer can be understood by an idealized spring-mass system as illustrated in Figure B-1 below. In this system, a proof mass, m , is suspended on a mechanical frame by a spring, k , and responds to an input acceleration force, F . The input force causes a displacement x of the mass. The displacement is sensed by electrostatic means: a capacitor, $CS(x)$, is used with one terminal residing on the mass and the other terminal on the fixed frame. The proof mass is also subjected to a damping force proportional to its velocity, represented by a damping coefficient b in the figure. In inertial sensors, air damping is typically the main damping factor, thus it is important to hermetically seal the mechanical elements to allow operation of the sensor at low pressure [Shaeffer 2013].

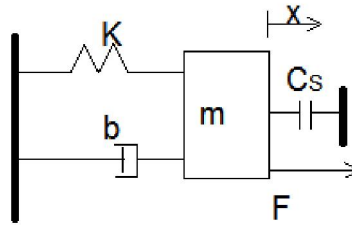


Figure B-1 Spring-mass-dashpot system

The mechanical equation of Spring-mass-dashpot in Figure 3-2 can be derived in a second-order canonical form as:

$$m\ddot{x}(t) + b\dot{x}(t) + kx(t) = F(t) \quad (\text{B. 1})$$

Applying the Laplace transform, the force-displacement is characterized by its transfer function.

$$\frac{x(s)}{F(s)} = \frac{1}{ms^2 + bs + k} = \frac{1/m}{s^2 + \frac{\omega_0}{Q}s + \omega_0^2} \quad (\text{B. 2})$$

Where, the undamped resonant frequency ω_0 , damping coefficient α and quality factor Q are given below [Senturia2001].

$$\omega_0 = \sqrt{\frac{k}{m}} \quad (\text{B. 3})$$

$$\alpha = \frac{b}{2m} \quad (\text{B. 4})$$

$$Q = \frac{m\omega_0}{b} = \frac{\omega_0}{2\alpha} \quad (\text{B. 5})$$

Usually the accelerometer operates in quasi-static state such that the operation frequency of the proof mass is much less than the natural mechanical frequency of the structure. Thus the system transfer function in (B.2) can be simplified ($s=j\omega \rightarrow 0$) as:

$$x = \frac{F}{k} = \frac{F}{m \cdot \omega_0^2} = \frac{a}{\omega_0^2} \quad (\text{B. 6})$$

As a transducer, the accelerometer converts mechanical energy to electrical energy. As a sensor, additional electronic circuitry is used to interpret or quantify the changes in capacitance with proportional changes in acceleration. Therefore, capacitive sensing is a critical technique relying on the variation of capacitance appearing when the geometry of a capacitor is changing.

Capacitance has the following relationship with dimensions:

$$C = \varepsilon \frac{A}{d} \quad (\text{B.7})$$

Where:

A = the area of the electrodes

d = the distance between the electrodes

ε = the dielectric constant.

A change in any of these parameters will be measured by readout circuitry as a change in capacitance. For small displacements, the effect of attractive electrostatic force on the system dynamics may be modeled by an equivalent negative spring constant, which shows that electrostatic forces reduce the effective spring constant of the system. Compared to a parallel plate capacitor structure, comb-finger capacitors do not suffer from this problem to the first order of approximation [Shaeffer2013], as the electrostatic force is not position-dependent. In addition, the differential capacitors have higher sensitivity and can be configured to give a linear response, and are therefore preferred in many designs. A basic differential structure is shown in Figure B-2(a) and it is equivalent to two variable capacitors in series, as showing in Figure B-2(b).

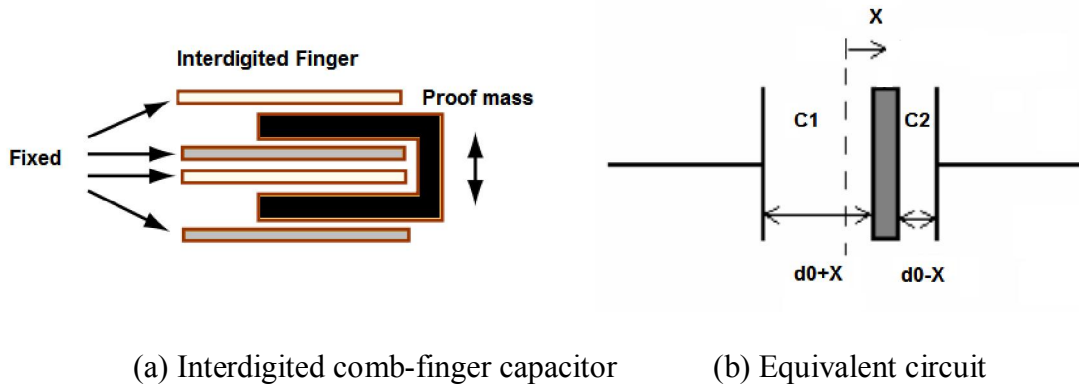


Figure B-2 A basic differential structure of accelerometer

Some trans-impedance circuits can be developed to detect the differential capacitance change ΔC , which is proportional to the displacement x [Sharma 2007].

$$\Delta C = C1 - C2 = 2C_0 \frac{x}{d_0} \quad (\text{B.8})$$

Many leading MEMS manufacturers have designed comb-finger capacitor structures in accelerometers. Analog Devices first designed a comb capacitor accelerometer in the 1990s: the movable parts consist of four folded-beams, a proof mass and some movable fingers. The fixed parts include two anchors and some left/right fixed fingers [Yazdi 1998]. Bosch's silicon-based accelerometer has inter-digitated fingers that are patterned in a thick epitaxy polysilicon film using a deep reactive ion etching technique. These thick structures have high aspect ratios with a working capacitance near 1 pF [Bhushan 2010]. ST Micro's accelerometers were fabricated with the 0.8-micron, surface micro-machining THELMA (Thick Epitaxial Layer for Micro-gyroscopes and Accelerometers) process combing variably thick and thin poly-silicon layers for structures and interconnections [STM 2013]. This enables the integration of linear and angular mechanical elements in a single chip, thus delivering significant cost and size benefits.

B.2.2 Gyroscopes

Gyroscopes are sensors designed for measuring angular rotations about some specific axes with respect to inertial space [Antonello 2011]. Classical spinning mass gyroscope has a free movable axis called gimbal, it is based on the angular momentum of a rotating body. Gyroscopic effects cause precession that can be detected as a measure of angular rate. Later on, optical gyroscopes became available; it was based on Sagnac effect made of a ring laser or fiber with two counter-rotating light beams circulating around an optical path of a certain radius. These traditional designs cannot meet the requirements of low-cost, low-power, and miniaturized devices due to limitations of micro-fabrication techniques. Almost all modern consumer MEMS gyroscopes are of a vibratory type, based on sensing Coriolis acceleration, which is acceleration produced due to the changing direction in space of the velocity of a moving system.

The operation of vibratory gyroscopes is governed by the equation of relative motion [El-Sheimy 2008], the particle velocity $V^i = \dot{r}^i$ as viewed in the inertial frame-i is related to the velocity $V^r = \dot{r}^r$ in the rotating frame-r by:

$$\dot{r}^i = \dot{r}^r + \Omega \times r^r \quad (\text{B.9})$$

Where:

r^r = the time-dependent position vector in the rotating frame

$\Omega = (\Omega_x, \Omega_y, \Omega_z)^t$ is the rotation vector with respect to the rotating frame.

Applying this time derivative relationship again, we can get the acceleration of the particle in the inertial frame as:

$$\ddot{r}^i = \ddot{r}^r + 2\Omega \times \dot{r}^r + \Omega \times (\Omega \times r^r) + \dot{\Omega} \times r^r \quad (\text{B.10})$$

As Newton's Second Law only applies in the inertial frame, $F^i = m\ddot{r}^i$, hence the apparent acceleration in the rotating frame, \ddot{r}^r , yields the following relationship in Equation (B.11).

$$m\ddot{r}^r = F^i - 2m\Omega \times \dot{r}^r - m\Omega \times (\Omega \times r^r) - m\dot{\Omega} \times r^r \quad (\text{B.11})$$

Where $-2m\Omega \times \dot{r}^r$ is known as Coriolis acceleration force;

$-m\Omega \times (\Omega \times r^r)$ is the centrifugal force.

When the angular rate is much smaller than proof mass resonant frequency, this term can be neglected; and the remaining term $-m\dot{\Omega} \times r^r$ is due to a non-constant rotation rate of the rotating frame, it can neglected as well when the sensors have relatively small output bandwidths. With the knowledge of \ddot{r}^r and neglecting the last two terms in Equation (B.11), the following mechanical equation of proof mass motion can be derived [Antonello 2011].

$$M\ddot{r}^r + D\dot{r}^r + Kr^r = F^i - 2m\Omega \times \dot{r}^r \quad (\text{B.12})$$

Where M, D and K are positive definite mass, damping and stiffness matrices.

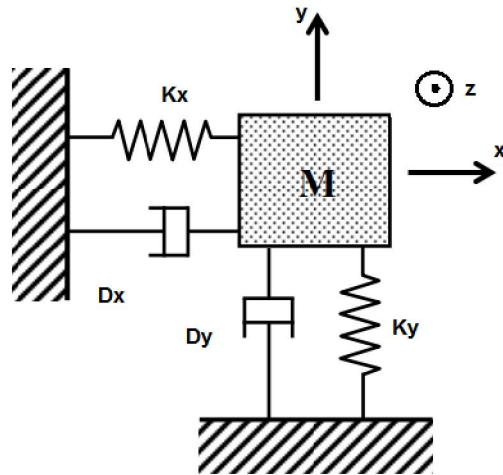


Figure B-3 A simplified model for Z-axis gyroscope

Based on the above classical mechanics principles, a single axis vibrating gyroscope can be built. As illustrated in Figure B-3, the gyro frame rotates about the z axis, orthogonal to the x-y plane. A proof mass M is attached to the rotating sensor frame by elastic suspensions. Two degrees of mechanical freedom are required, one for the drive and one for motion sensing. The proof mass is first put into drive mode of vibration along the x-axis, with a controlled-amplitude of oscillation. Once in motion, the proof-mass is sensitive to angular rotation about the z-axis perpendicular to the plane. This rotation thus induces a vibratory displacement from the Coriolis force along the y-axis, known as sense mode to measure the angular rate. Referring to Equation (B.12), the motion equations in x-y plane become:

$$m_x \ddot{x}^r + d_x \dot{x}^r + k_x x^r = F_x^i + 2m\Omega_z \dot{y}^r \quad (\text{B.13})$$

$$m_y \ddot{y}^r + d_y \dot{y}^r + k_y y^r = F_y^i - 2m\Omega_z \dot{x}^r \quad (\text{B.14})$$

Assume the solution to (B.13), which is the x-displacement along the drive axis, is given by a sinusoidal form

$$x = -X_d \sin(\omega_d t) \quad (\text{B.15})$$

And there is also no external excitation to the sense mode, i.e. $F_y^i = 0$. The resulting system has one degree of freedom along the sensing y-axis, governed by

$$m_y \ddot{y}^r + d_y \dot{y}^r + k_y y^r = 2m\Omega_z X_d \omega_d \cos(\omega_d t) \quad (\text{B.16})$$

That is a typical second-order non-homogeneous linear different equation [Younis 2011]. By introducing natural frequency ω_s and quality factor Q_s of the sense mode, (B.16) becomes

$$\ddot{y}^r + \frac{\omega_s}{Q_s} \dot{y}^r + \omega_s^2 y^r = 2\Omega_z X_0 \omega_d \cos(\omega_d t) \quad (\text{B.17})$$

Where:

$$w_s = \sqrt{k_y/m_y}$$

$$Q_s = w_s m_y / d_y$$

A convenient way to express this solution is through a form of an amplitude Y and a phase θ as:

$$y_s(t) = Y \cos(w_s t - \theta) \quad (\text{B.18})$$

Where:

$$Y = \frac{2w_s X_d \Omega_z}{\sqrt{(w_s^2 - w_d^2)^2 + (\frac{w_s w_d}{Q_s})^2}} \quad (\text{B.19})$$

$$\theta = \tan^{-1}\left(\frac{w_s w_d}{Q_s(w_s^2 - w_d^2)}\right) \quad (\text{B.20})$$

From Eq. (B.19), we can see that the sensing amplitude output is proportional to the input angular rate Ω_z . If the sense and drive resonant frequency is equal (i.e. $w_s = w_d$), the output signal will be amplified by quality factor Q_s of the sense mode, resulting in high gain.

Figure B-4 shows the block diagram of a typical vibratory gyroscope. It consists of a drive actuator and is represented by the equivalent drive-mode dynamic transfer function. The drive amplitude X_0 must be maintained very accurately since any variation will contribute directly to the sense output. Therefore, the drive loop is controlled by an automatic gain control loop. In the sense branch, the Coriolis term is twice the product of the input angular rate and the velocity of the drive axis oscillator in quadrature which produces a modulated signal. The spring-mass sensing MEMS is equivalent to a sense-mode dynamic transfer function. Consequently, the gyroscope output needs to be demodulated by multiplying the in-phase drive signal coming from a phase-locked loop (PLL). The result was passed through a low-pass filter (LPF). Lastly, the

gain was adjusted to compensate for temperature and any other scale factors

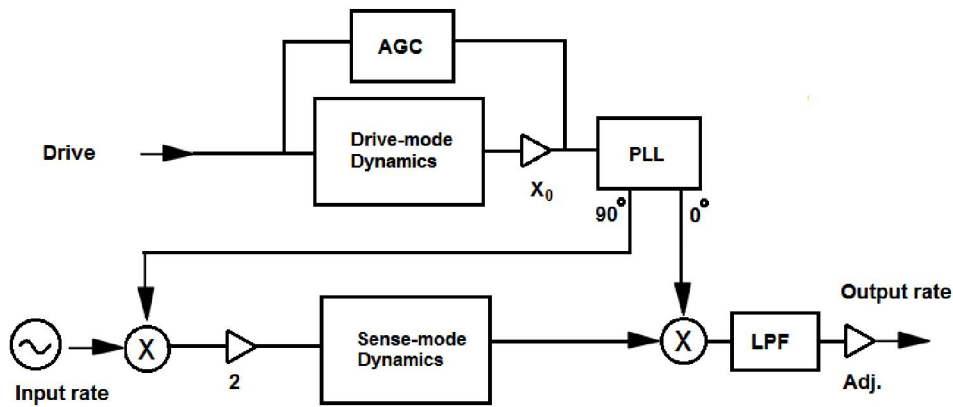


Figure B-4 Block diagram of vibratory gyroscope

Common MEMS designs utilize suspended plates that provide movement with two Degrees Of Freedom. Basic structure types include translation-based gyroscopes (like tuning forks) and rotation-based gyroscopes (like vibrating plates and shells). Figure B-5 [Antonello 2011] illustrates the most conventional types of Coriolis vibrating gyroscopes where $\Omega(t)$ is the input angular rate, (1) is the primary driving vibration mode and (2) is the sensing mode induced by the Coriolis force.

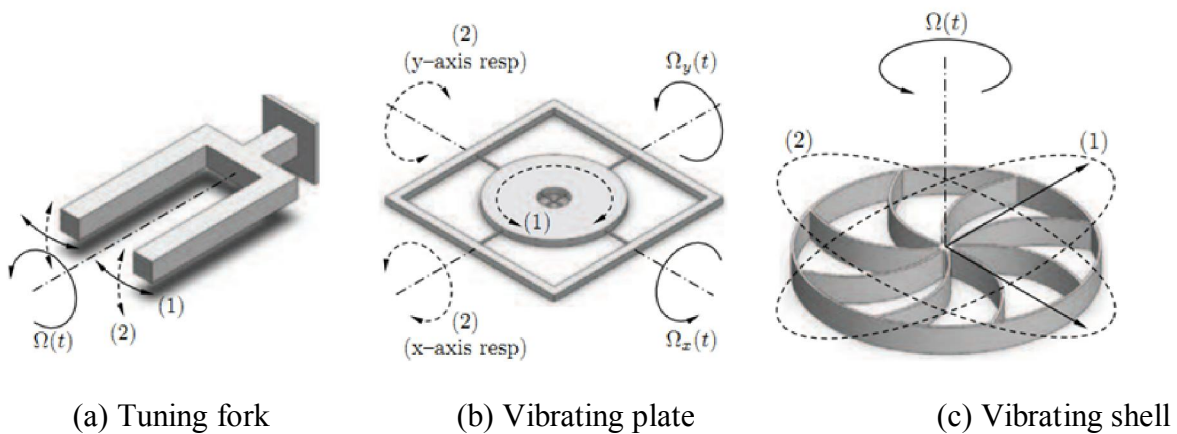


Figure B-5 Mechanical structure design of Coriolis vibrating gyroscope

Tuning fork gyroscopes (TFGs) are a classical type of vibrating gyroscope consisting of two tines that are connected to a junction bar. The two tines are driven in opposite directions with the same amplitude. When rotated, the Coriolis force causes a differential sinusoidal force to develop on the individual tines, orthogonal to the driving vibration, as shown in FigureB-5 (a). The vibrating plate gyroscope is driven to vibrate about its axis of symmetry, as shown in FigureB-5 (b), then rotation about either in-plane axis, the X or Y axis, results in the plate tilting. This tilt can be detected with capacitive electrodes underneath. Shown in FigureB-5(c), the vibrating shell has a circular shape that has eight support springs. These supports give it a balanced ring with two identical flexural modes that have equal natural frequencies. The electrostatic force vibrates the ring in an in-plane elliptically shaped primary flexural pattern (1). When the device is rotated around its normal axis, energy is transferred to the secondary pattern (2). This symmetrical structure is less temperature sensitive since both vibration modes change similarly with temperature changes.

In 1987, Charles Stark Draper Laboratory was the first to demonstrate a working MEMS gyro on silicon [Yazdi 1998]. About ten years later, Robert Bosch GmbH introduced the first silicon MEMS gyro for electronic stability program systems for automotive applications. Since then, consumer applications began to emerge. More recently, gaming consoles, smart phones, and wearable applications have pushed innovations for low-cost implementation of MEMS gyroscopes. The tuning fork is by far the most commercially successfully type of gyroscope, well suited for low-cost surfaces and bulk micromachining technologies. An integrated 3-axis MEMS gyroscope with signal processing ASIC has become main stream.

Two companies are notably successful in the modern MEMS gyroscope arena: ST Microelectronics and Invensense. In 2010, ST Microelectronics launched its three-axis gyroscope,

the L3G4200D. This gyro is fabricated with the same THELMA process used to build accelerometers [STM 2010]. The packaged gyro is an ASIC plus MEMS stacked die, where the MEMS sensor uses tuning fork mass structures to measure pitch, roll, and yaw. Rotation of the device around three-dimensional axes will cause deflections of the different planes, which are detected by banks of interdigitated capacitor plates. Invensense's three-axis digital gyroscope, the ITG-3200 [Invensense 2009] is built using patented Nasiri-Fabrication process, where the MEMS layer is sandwiched between a fusion-bonded cap wafer and the ASIC. The ASIC and MEMS are bonded using a eutectic metal bond, so the overall die size and cost are low.

B.2.3 Magnetometers

The Earth's magnetic field is a vector quantity that has both magnitude and direction. Its magnitude ranges from 25 to 65 μT ($1 \mu\text{T}=0.01$ Gauss) and its direction has a component parallel to the Earth's surface that always points toward magnetic North. This forms the basis for all magnetometer measurements. In general, the requirement of a magnetometer for navigation is quite demanding, as Earth's magnetic field is a relatively weak signal compared to many surrounding electro-magnetic interferences. Meanwhile, a high resolution is preferred in order to derive an accurate heading for navigation.

Unlike MEMS gyroscope designs where a simple mechanical structure and basic physics was utilized to calculate roll, pitch, and yaw from with one direct measurement for each variable, magnetometers measure the magnetic field in various ways. There are several popular methods commonly used for low-cost MEMS products in mobile devices. The first type utilizes an Anisotropic Magneto-Resistance (AMR) sensor that lends itself well to the Earth's field sensing range. AMR sensors are made of a permalloy thin film deposited on a silicon wafer and is

patterned as a resistive strip. The properties of the AMR thin film cause it to change resistance in the order of 3% in the presence of a magnetic field. Typically, four of these resistors are connected in a Wheatstone bridge configuration so that both magnitude and direction of a field along a single axis can be measured; Figure B-6 shows the concept of the measurement [Caruso 1998]. AMRs became mature at the end of the 1990s. The HMC series produced by Honeywell typically have dynamic ranges of hundreds of μT and resolutions on the order of nT. AMR technology has good sensitivity and reasonably good temperature stability. The limitation of this method is that as time goes by, or temperature increases, the directional magnetization loses its directionality; therefore calibration and additional magnetization resets are required.

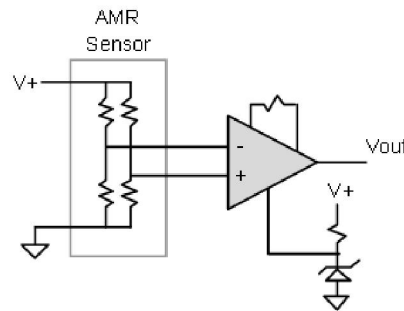


Figure B-6 AMR sensor circuit

The Giant Magneto-Impedance (GMI) sensor is a highly sensitive micro magnetic sensor based on the magneto-impedance effect [Mohri 1995]. When a soft ferromagnetic conductor (e.g. amorphous wire) is subjected to a small alternating current (ac), a large change in the ac complex impedance of the conductor can be detected by applying a magnetic field change. Compared to the small percent change in resistance observed in the AMR sensor, this phenomenon exhibits a large change, thus making the GMI extremely sensitive. Figure B-7 illustrates this concept: an ac

current invoked through a wire-shaped material along the wire axis, yielding a circular magnetic field based on Faraday's law.

$$\text{Farady's law: } V = -nA \frac{dB}{dt} \quad (\text{B.21})$$

Where:

V = output voltage

B = the flux density passing through a coil

A = the cross-sectional area of the coil

n = the number of turns in the coil

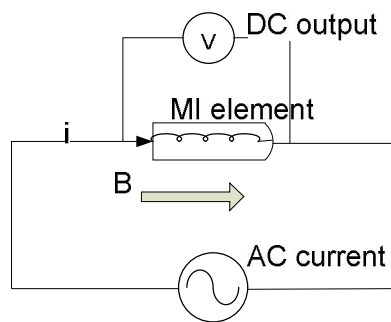


Figure B-7 Concept of magneto-impedance effect

The collective result of this process is the charge distribution concentrating on the surface. This is known as the skin effect. The application of the magnetic field increases the skin depth while decreasing the circumferential permeability, consequently impedance is altered via the permeability, which is governed by the external magnetic field. This field can be measured from the DC voltage output. Aichi Steel has developed magneto-impedance magnetometers with high resolution; the drawback is MI sensors are bulk assembled sensors with a relatively larger chip size compared to other technology. Similarly, Yamaha and ALPS, manufacturers from Japan, developed Giant Magneto-Resistive (GMR) magnetometers, where large magnetic field

dependent changes in resistance are made in thin-film ferromagnet/non-magnetic metallic multi-layers [Caruso 1998].

Another type of magnetometer widely used in mobile devices functions based on the Hall Effect. It works on the principle that a voltage V_{hall} can be developed in a direction transverse to the current flow in a system of charged particles in a magnetic field, owing to the Lorentz force F .

$$F = q (\mathbf{v} \times \mathbf{B}) \quad (\text{B.22})$$

Where:

q = the charge of free carriers

\mathbf{v} = the velocity of the free carriers

\mathbf{B} = the magnetic field

Figure B-8 below illustrates this relationship.

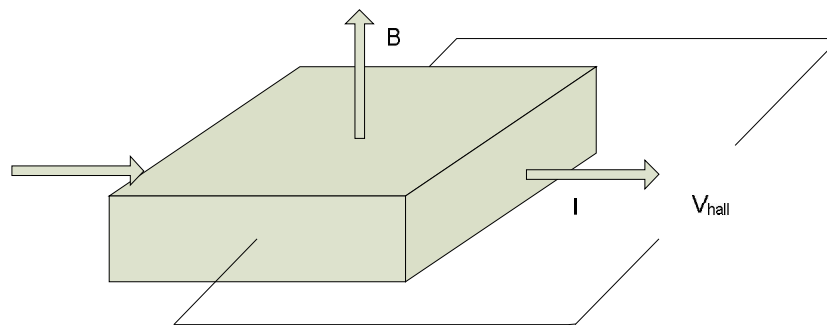


Figure B-8 Hall effect principle

By measuring the Hall voltage output across the metallic surface, the proportional magnetic field can be derived. This method is very low-cost, small sized, and low power, thus it is predominantly used in smartphones today. These sensors can be found in AKM's products for

many smartphones. The main drawback, however, is the comparatively low sensitivity for magnetic sensing and the Hall device needs temperature compensation because increasing in temperature increases the electron motilities.

B.2.4 Barometer

Pressure sensors are the earliest MEMS sensors successfully applied in a wide-range of applications including automotive systems, industrial control, medical diagnostics, and consumer applications. For barometer applications on a mobile device, atmospheric pressure measurement can be used to estimate vertical elevation, which has higher resolution than GPS. Usually air pressure on Earth ranges from a few hundred millibars at high altitude to a little more than one thousand millibars at sea level. One standard atmosphere equals 1,013 mbar at sea level.

A MEMS pressure sensor consists of a flexible diaphragm that deforms in the presence of a pressure difference [Bicking 1998]. Barometers usually give an absolute pressure measurement, where the reference is an internal vacuum in a sealed cavity. So there is only one inlet allowing air pressure to be applied to one side of the diaphragm. The pressure difference between the sealed cavity and the surrounding environment produces a deflection of the diaphragm, which is then converted to an electrical signal.

The deflection in a barometer can be measured by either capacitive sensing or piezoresistive sensing. In capacitive technology, the pressure diaphragm is one plate of a capacitor that changes its value under pressure-induced displacement. Capacitive pressure sensors are known to have superior performance to piezoresistive pressure sensors in terms of their package stress, sensitivity, and temperature dependence [Chiang 2011]. However, capacitive sensors have lower output signals with small deflection of a plane, so the signal conditioning and readout are much

more complicated. Also, wirebonds can easily pick up noise without shielding and are very sensitive to moisture.

In contrast, piezoresistive pressure-sensor technology has become a low-cost, batch-fabrication manufacturing technology more widely used for barometers. Piezoresistors are integrated across the diaphragm. The change in ambient pressure forces a deformation of the diaphragm, resulting in a change of resistance. This resistance change is translated into an output voltage using a Wheat-stone bridge and then calculated into pressure. For constant temperature operation, the sensors can include a temperature controller for compensation.

The following Figure B-9 shows a silicon diaphragm using MEMS micromachining technology [Ristic 2012]. A sealed vacuum cavity is formed at the top of the silicon substrate. Then piezoresistive elements are placed at the edge of the diaphragm where the stress is the largest. The package needs to have at least one opening hole since pressure sensors need to be physically exposed to the medium.

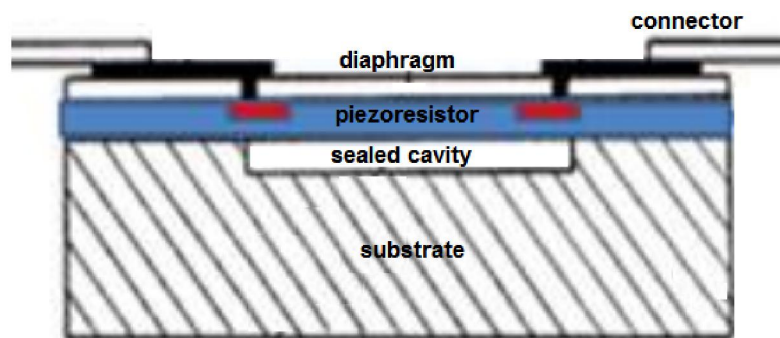


Figure B-9 Silicon fabrication of piezoresistive diaphragm

MEMS manufacturers have fabricated such pressure-sensing devices using proprietary technology. For example, ST's LPS331AP [STM 2012] VENSENS fabrication process allows

the integration of a cavity into monocrystalline silicon. Bosch's latest BMP280 [Bosch 2012] uses an Advanced Porous Silicon Membrane (APSM) technology to transfer a vacuum cavity. Both sensors are CMOS compatible with low power and small size; the integration of temperature sensors with factory calibration of pressures and temperatures enables a low temperature coefficient. As a result, they can achieve resolutions within 1 meter.

APPENDIX C: ATTITUDE REPRESENTATION

In almost all sensors applications, it is often needed to know the orientation or attitude of the rigid body that the sensor is attached to in free space, with respect to a reference frame attached to the Earth. The aim of this section is to review some of the commonly used attitude parameterizations used to describe a device's attitude. Usually aerospace and pedestrian navigation have different conventions on attitude definitions. Consistent and clear definitions are essential to remove fragmentation in sensor implementations from different industries. This section clarifies conventions for attitude representations in the sensor fusion algorithms.

Attitude and rotation transformation can be accomplished in multiple ways: yaw-pitch-roll Euler angles, rotation Direction Cosine Matrix (DCM), or quaternions. The Euler rotation angles are intuitively easy to understand but contain ambiguities. Problem-free representations of the transformation can be done using DCM; however this matrix contains 9 variables in a 3 by 3 matrix. The most efficient way is represented by normalized quaternions, which use only 4 values with a unit-norm constraint. This section presents their definitions and relationship.

C.1 Coordinate Definition

C.1.1 Navigation Frame

The navigation frame, also known as the local-level frame or the world coordinate frame, is a local tangent plane coordinate system fixed in inertial space. It provides local reference directions near the Earth's surface for navigation. The vector in navigation coordinates is denoted as \mathbf{x}^n . The mathematics described in attitude sensors fusion only applies when the navigation frame is rotationally fixed. For personal navigation applications, it is acceptable to

assume a slowly-rotating coordinate system, such as the one rigidly attached to earth, to be a valid navigation coordinate system, despite its non-zero angular velocity [Diebel 06].

East-North-Up (ENU) and North-East-Down (NED) are two common right-handed coordinate systems. The origin of both coordinate systems is usually chosen to be the vehicle's center of gravity. In NED coordinates, the X-axis is in the north direction, the Y-axis is east, and the Z-axis is down. NED coordinates have some advantage because the direction of the clockwise heading changes is positive with respect to a downward Z-axis. It is popular in airspace, since most objects of interest are underneath, it is more reasonable to define down as a positive number.

On the other hand, in ENU coordinates, the X-axis is in the east direction, the Y-axis is north, and the Z-axis is up. This convention is preferred in land navigation because altitude intuitively increases in the upward direction. The coordinate transformation between ENU and NED is

$$\mathbf{R}_{ned}^{enu} = \mathbf{R}_{enu}^{ned} = \begin{pmatrix} 0 & 1 & 0 \\ 1 & 0 & 0 \\ 0 & 0 & -1 \end{pmatrix} \quad (\text{C.1})$$

ENU is selected in this thesis to be in line with Android's latest convention for smartphone applications, as illustrated in Figure C-1.

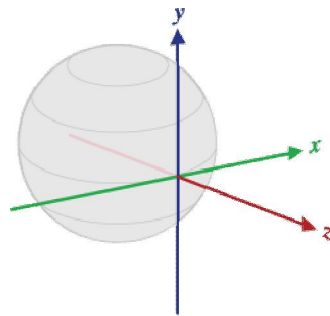


Figure C-1 East-North-Up (ENU) definition for navigation frame

C.1.2 Body Frame

The body frame, also known as the sensors frame or phone frame, is a coordinate system rigidly attached to the object for attitude estimation. The body frame is the frame in which multiple sensors are resolved. The vector in the body frame coordinate is denoted as \mathbf{x}^b . Consider a phone form-factor device with multiple MEMS sensors, as shown below in Figure C-2, the body frame axes are defined as:

- X-axis is lateral and points to the right of the device
- Y axis is longitudinal and points to the forward direction
- Z-axis points upwards completing the right hand rule, we call it Right-Forward-Up (RFU) convention.

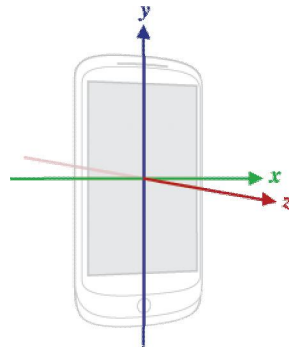


Figure C-2 Right-Forward-Up (RFU) definition for body frame

C.2 Euler Angle

Leonhard Euler proved that any orientation of a rigid body in 3-dimensional Euclidean space can be expressed in terms of up to three elemental rotations around coordinate axes. Euler angles represent these three composed rotations that move a reference frame to a given referred frame [Kuniper 1999]. These three Euler angles are roll, pitch, and yaw (also known as heading and

azimuth). Roll, pitch, and yaw angles are denoted as (R, P, H) in this document; they are also commonly referenced as (ϕ , θ , ψ) in many literatures [Shuster 1993].

The Roll-pitch-yaw coordinates are fixed with the sensors consistent with the body frame definition, as illustrated in the Figure C-3. The roll axis is along the forward direction of the device motion; the pitch axis points out to the right-hand side; and the yaw axis points up. All the Euler angles are defined such that turning clockwise is positive.

To ensure a one-to-one mapping of all possible yaw-pitch-roll angles to all possible orientations, one of the Euler angles must be restricted to a 180° range. For mobile conventions, the roll angle is the angle restricted from -90° to 90° . For aerospace conventions, pitch is restricted to the range of -90° to 90° . Usually the pitch angle of ± 90 degree causes a singularity issue; it is sometimes called ambiguity or often referred to as gimbal lock. At this point, the difference of yaw and roll are completely undetermined. This can be avoided by using quaternion expressions, as introduced later.

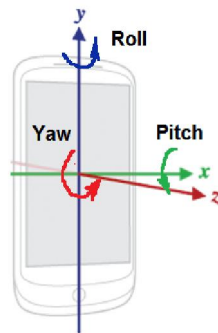


Figure C-3 Roll, pitch and yaw definition

C.3 Direction Cosine Matrix and Rotation Matrix

The Direction Cosine Matrix (DCM) is a 3×3 rotation matrix transforming vectors from one orthogonal basis to another. Suppose a vector \mathbf{x}^a in some frame a and a vector \mathbf{x}^b is frame b, then

$$\mathbf{x}^b = C_a^b \mathbf{x}^a = \begin{pmatrix} \mathbf{i}_a \cdot \mathbf{i}_b & \mathbf{j}_a \cdot \mathbf{i}_b & \mathbf{k}_a \cdot \mathbf{i}_b \\ \mathbf{i}_a \cdot \mathbf{j}_b & \mathbf{j}_a \cdot \mathbf{j}_b & \mathbf{k}_a \cdot \mathbf{j}_b \\ \mathbf{i}_a \cdot \mathbf{k}_b & \mathbf{j}_a \cdot \mathbf{k}_b & \mathbf{k}_a \cdot \mathbf{k}_b \end{pmatrix} \mathbf{x}^a \quad (\text{C.2})$$

Where $(\mathbf{i}_a, \mathbf{j}_a, \mathbf{k}_a)$ and $(\mathbf{i}_b, \mathbf{j}_b, \mathbf{k}_b)$ are the orthonormal bases of frame a and b, respectively.

The rotation matrix C_a^b notation indicates a transformation from the a-frame to the b-frame.

Because the basis vectors are of unit length, the dot products in the rotation matrix define the cosines of the angles between the vector pairs, therefore the rotation matrix is also commonly known as the direction cosines matrix [Mohamed 2012].

In mechanics and geometry, the 3D rotation group is a is the group of all rotations about the origin of three-dimensional Euclidean space \mathbf{R}^3 , often denoted as SO(3) [Kuniper 1999], the Special Orthogonal group of all rotations about the origin of three-dimensional Euclidean space \mathbf{R}^3 under the operation of composition. The DCM is a widely used attitude representation with three degrees of freedom. Transformations between navigation to body frames are particularly useful. In sensors fusion, sensors measure values in the body frame, whereas positions are normally derived in the navigation frame. This can be seen from of the following vector transformation:

$$\mathbf{v}^n = C_b^n \mathbf{v}^b \quad (\text{C.3})$$

Where:

v^b is a vector, v , resolved in the body fixed coordinate system

v^n is the same vector resolved in the navigation frame

C_b^n is the rotation matrix from the body frame to the navigation frame

Three dimensional rotation transformations can be decomposed by three consecutive rotations. Out of the 27 possible rotation sequences of three axes, there are only 12 that satisfy the constraint that no two consecutive numbers in a valid sequence may be equal [Diebel 2006]. The following derivation adopts one of the common sequences: yaw angle rotation along the z-axis first; pitch angle rotation along x-axis next; roll angle rotation along y-axis last, all following Euler's angle definition in the RFU body and ENU navigation frame conventions.

Denote $(x, y, z)^n$ as a vector in the navigation frame and after three successive rotations, it transforms to the body frame $(x''', y''', z''')^b$, as illustrated in Figure C-4 below.

$$(x, y, z)^n \xrightarrow{R_z(H)} (x', y', z')^1 \xrightarrow{R_x(P)} (x'', y'', z'')^2 \xrightarrow{R_y(R)} (x''', y''', z''')^b$$

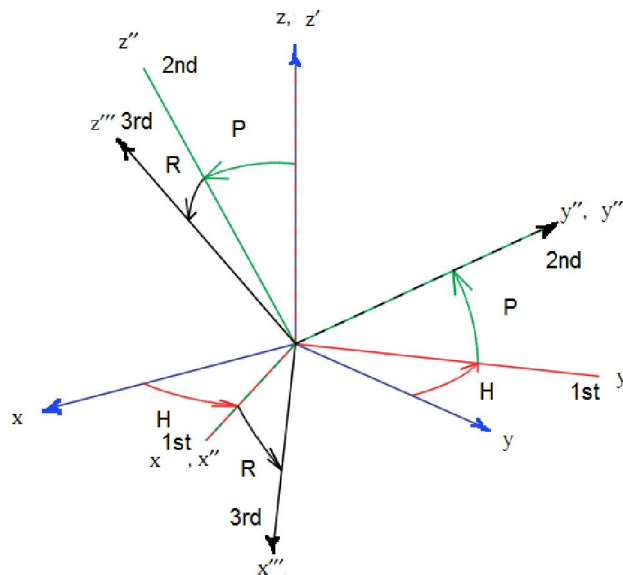


Figure C-4 Navigation to body frame transformation: yaw→pitch→roll sequence

Rotation matrix $C_n^b(R, P, H)$ can be found by concatenating successive rotations as

$$C_n^b = R_y(R)R_x(P)R_z(H) \quad (C.4)$$

Where the individual rotation matrices about the x, y and z axes have angles P, R and H, are as follows:

$$R_x(P) = \begin{pmatrix} 1 & 0 & 0 \\ 0 & \cos P & \sin P \\ 0 & -\sin P & \cos P \end{pmatrix} \quad (C.5)$$

$$R_y(R) = \begin{pmatrix} \cos R & 0 & -\sin R \\ 0 & 1 & 0 \\ \sin R & 0 & \cos R \end{pmatrix} \quad (C.6)$$

$$R_z(H) = \begin{pmatrix} \cos H & \sin H & 0 \\ -\sin H & \cos H & 0 \\ 0 & 0 & 1 \end{pmatrix} \quad (C.7)$$

Therefore,

$$\begin{aligned} C_n^b &= R_y(R)R_x(P)R_z(H) \\ &= \begin{pmatrix} \cos R \cos H - \sin P \sin R \sin H & \cos R \sin H + \sin R \sin P \cos H & -\cos P \sin R \\ -\cos P \sin H & \cos P \cos H & \sin P \\ \sin R \cos H + \sin P \cos R \sin H & \sin R \sin H - \sin P \cos R \cos H & \cos P \cos R \end{pmatrix} \quad (C.8) \end{aligned}$$

C.4 Quaternions

The quaternions, hyper-complex numbers with four components, were first introduced by William Rowan Hamilton in the 19th century. Quaternion is a preferred attitude representation in three dimensional rotations: it is computationally efficient and numerically stable without singularity. A quaternion has four elements consisting of a triplet of vector part and one scalar part defined as:

$$\bar{q} = q_1 i + q_2 j + q_3 k + q_4 \quad (\text{C.9})$$

Where the bases elements i, j , and k are defined as:

$$i^2 = j^2 = k^2 = ijk = -1$$

Markley [Markley 008-1], Sabatini [Sabatini 2006] all use this expression in the references which will be adopted in this thesis. An overbar, \bar{q} , is used for quaternions notation.

Since a three degree of freedom attitude is represented by a four dimensional vector, the quaternions are not independent and need to obey the normalization constraint with a unit norm.

$$|\bar{q}|^2 = q_1^2 + q_2^2 + q_3^2 + q_4^2 = 1 \quad (\text{C.10})$$

From the definition of the quaternion basis above, we can obtain a formula for quaternion product, denoted as \otimes . It is more convenient to write the quaternions product of \bar{p} and \bar{q} in matrix multiplication as [Crassidi 2004]:

$$\begin{aligned} \bar{p} \otimes \bar{q} &= \begin{bmatrix} p_4 & p_3 & -p_2 & p_1 \\ -p_3 & p_4 & p_1 & p_2 \\ p_2 & -p_1 & p_4 & p_3 \\ -p_1 & -p_2 & -p_3 & p_4 \end{bmatrix} \bar{q} = [\Psi(\bar{p}) \quad \bar{p}] \bar{q} \\ &= \begin{bmatrix} q_4 & -q_3 & q_2 & q_1 \\ q_3 & q_4 & -q_1 & q_2 \\ -q_2 & q_1 & q_4 & q_3 \\ -q_1 & -q_2 & -q_3 & q_4 \end{bmatrix} \bar{p} = [\Xi(\bar{q}) \quad \bar{q}] \bar{p} \end{aligned} \quad (\text{C.11})$$

The conjugate quaternions \bar{q}^* and inverse quaternions \bar{q}^{-1} can be defined as

$$\bar{q}^* = -q_1 i - q_2 j - q_3 k + q_4 \quad (\text{C.12})$$

$$\bar{q}^{-1} = \frac{\bar{q}^*}{|\bar{q}|^2} \quad (\text{C.13})$$

The quaternion kinematics equations are linear in quaternion expression as:

$$\dot{\bar{q}} = \frac{1}{2} \begin{bmatrix} w_1 \\ w_2 \\ w_3 \\ 0 \end{bmatrix} \otimes \bar{q} = \frac{1}{2} \Omega(\omega) \bar{q} = \frac{1}{2} \Xi(\bar{q}) \omega \quad (\text{C.14})$$

Where $\omega = [w_1 \ w_2 \ w_3]^t$ is the angular rate vector from gyroscope measurements:

$$\Omega(\omega) = \begin{bmatrix} 0 & w_3 & -w_2 & w_1 \\ -w_3 & 0 & w_1 & w_2 \\ w_2 & -w_1 & 0 & w_3 \\ -w_1 & -w_2 & -w_3 & 0 \end{bmatrix} \text{ is the symmetric skew matrix.}$$

$$\Xi(\bar{q}) = \begin{bmatrix} q_4 & -q_3 & q_2 \\ q_3 & q_4 & -q_1 \\ -q_2 & q_1 & q_4 \\ -q_1 & -q_2 & -q_3 \end{bmatrix} \text{ is the same definition as the quaternion product above.}$$

Another advantage of the quaternion is that successive rotations can be accomplished using quaternion multiplication. Let \bar{q}_1 and \bar{q}_2 be arbitrary unit quaternions, rotation by \bar{q}_1 followed by \bar{q}_2 is given by:

$$R(\bar{q}) = R(\bar{q}_2)R(\bar{q}_1) = R(\bar{q}_2 \otimes \bar{q}_1) \quad (\text{C.15})$$

C.5 Conversion between Quaternion, DCM and Euler Angles

This section introduces the conversion between the most popular attitude representations following H/P/R rotation sequence [Diebel 2006].

C.5.1 Euler Angles -> DCM

$$C_n^b = \begin{pmatrix} \cos R \cos H - \sin P \sin R \sin H & \cos R \sin H + \sin R \sin P \cos H & -\cos P \sin R \\ -\cos P \sin H & \cos P \cos H & \sin P \\ \sin R \cos H + \sin P \cos R \sin H & \sin R \sin H - \sin P \cos R \cos H & \cos P \cos R \end{pmatrix} (\text{C.16})$$

C.5.2 DCM -> Euler Angles

$$R = \text{atan2}(-C_{13}, C_{33}) \quad (\text{C.17})$$

$$P = \text{asin}(C_{23}) \text{ or } \text{atan2}(C_{21}, \sqrt{C_{13}^2 + C_{33}^2})$$

$$H = \text{atan2}(-C_{21}, C_{22})$$

Where C_{ij} is the i th row and j th column in the DCM.

C.5.3 Quaternion -> DCM

$$C_n^b(\bar{q}) = \begin{bmatrix} 1 - 2(q_2^2 + q_3^2) & 2(q_1q_2 + q_3q_4) & 2(q_1q_3 - q_2q_4) \\ 2(q_1q_2 - q_3q_4) & 1 - 2(q_1^2 + q_3^2) & 2(q_2q_3 + q_1q_4) \\ 2(q_1q_3 + q_2q_4) & 2(q_2q_3 - q_1q_4) & 1 - 2(q_1^2 + q_2^2) \end{bmatrix} \quad (\text{C.18})$$

C.5.4 DCM -> Quaternion

There are two methods to derive DCM from quaternion as listed below:

Method 1:

$$q_4 = \frac{1}{2} \sqrt{1 + C_{11} + C_{22} + C_{33}} \quad (\text{C.19})$$

$$q_1 = \frac{1}{2} \sqrt{1 + C_{11} - C_{22} - C_{33}}$$

$$q_2 = \frac{1}{2} \sqrt{1 - C_{11} + C_{22} - C_{33}}$$

$$q_3 = \frac{1}{2} \sqrt{1 - C_{11} - C_{22} + C_{33}}$$

Where the sign of quaternion is determined by following:

$$q_1 = q_1 \cdot \text{sign}(C_{32} - C_{23})$$

$$q_2 = q_2 \cdot \text{sign}(C_{13} - C_{31})$$

$$q_3 = q_3 \cdot \text{sign}(C_{12} - C_{21})$$

Method 2:

First calculate all four elements from the main diagonal of the DCM.

$$tmp_q_1 = \frac{1}{2} \sqrt{1 + C_{11} - C_{22} - C_{33}} \quad (C.20)$$

$$tmp_q_2 = \frac{1}{2} \sqrt{1 - C_{11} + C_{22} - C_{33}}$$

$$tmp_q_3 = \frac{1}{2} \sqrt{1 - C_{11} - C_{22} + C_{33}}$$

$$tmp_q_4 = \frac{1}{2} \sqrt{1 + C_{11} + C_{22} + C_{33}}$$

Usually elements close to zero can cause numerical inaccuracy, but at least one of the quaternions will not be zero due to the unity constraint. So the maximum value from the above temporary quaternions is selected to be the denominator then the quaternions are re-calculated based on Table C-1 below.

Table C-1 Quaternion elements recalculation

Max Re_cal.	tmp_q1	tmp_q2	tmp_q3	tmp_q4
q1	$\frac{1}{2} \sqrt{1 + C_{11} - C_{22} - C_{33}}$	$(C_{12} + C_{21}) / 4tmp_q2$	$(C_{31} + C_{13}) / 4tmp_q3$	$(C_{23} - C_{32}) / 4tmp_q4$
q2	$(C_{12} + C_{21}) / 4tmp_q1$	$\frac{1}{2} \sqrt{1 - C_{11} + C_{22} - C_{33}}$	$(C_{23} + C_{32}) / 4tmp_q3$	$(C_{31} - C_{13}) / 4tmp_q4$
q3	$(C_{13} + C_{31}) / 4tmp_q1$	$(C_{23} + C_{32}) / 4tmp_q2$	$\frac{1}{2} \sqrt{1 - C_{11} - C_{22} + C_{33}}$	$(C_{12} - C_{21}) / 4tmp_q4$
q4	$(C_{23} - C_{32}) / 4tmp_q1$	$(C_{31} - C_{13}) / 4tmp_q2$	$(C_{12} - C_{21}) / 4tmp_q3$	$\frac{1}{2} \sqrt{1 + C_{11} + C_{22} + C_{33}}$

Since the positive and negative quaternions represent the same rotation, we define q₄ to be positive by the following comparison.

If ($q_4 < 0$)

$$\{ q_1, q_2, q_3, q_4 \} = -\{ q_1, q_2, q_3, q_4 \};$$

Both the conversion methods are comparable, but the second method is more numerically stable, thus is recommended in this thesis.

C.5.5 Euler Angles -> Quaternion

$$\begin{aligned} q_1 &= \cos\left(\frac{R}{2}\right) \sin\left(\frac{P}{2}\right) \cos\left(\frac{H}{2}\right) - \sin\left(\frac{R}{2}\right) \cos\left(\frac{P}{2}\right) \sin\left(\frac{H}{2}\right) \\ q_2 &= \cos\left(\frac{R}{2}\right) \sin\left(\frac{P}{2}\right) \sin\left(\frac{H}{2}\right) + \sin\left(\frac{R}{2}\right) \cos\left(\frac{P}{2}\right) \cos\left(\frac{H}{2}\right) \\ q_3 &= \cos\left(\frac{R}{2}\right) \cos\left(\frac{P}{2}\right) \sin\left(\frac{H}{2}\right) + \sin\left(\frac{R}{2}\right) \sin\left(\frac{P}{2}\right) \cos\left(\frac{H}{2}\right) \\ q_4 &= \cos\left(\frac{R}{2}\right) \cos\left(\frac{P}{2}\right) \cos\left(\frac{H}{2}\right) - \sin\left(\frac{R}{2}\right) \sin\left(\frac{P}{2}\right) \sin\left(\frac{H}{2}\right) \end{aligned} \quad (C.21)$$

C.5.6 Quaternion -> Euler Angles

$$\begin{aligned} R &= \text{atan2}(-C_{13}, C_{33}) = \text{atan2}(-2(q_1q_3 - q_2q_4), (1 - 2(q_1^2 + q_2^2))) \\ P &= \text{asin}(C_{23}) = \text{asin}(2(q_2q_3 + q_1q_4)) \\ H &= \text{atan2}(-C_{21}, C_{22}) = \text{atan2}(-2(q_1q_2 - q_3q_4), (1 - 2(q_1^2 + q_3^2))) \end{aligned} \quad (C.22)$$

APPENDIX D: EQUATION DERIVATIONS IN CHAPTER FOUR

D.1: Derivation of $\delta\dot{\bar{q}}(t)$

From Equation (4.3) in Chapter 4,

$$\delta\dot{\bar{q}}(t) = \frac{1}{2} \left\{ \begin{bmatrix} \omega \\ 0 \end{bmatrix} \otimes \delta\bar{q}(t) - \delta\bar{q}(t) \otimes \begin{bmatrix} \hat{\omega} \\ 0 \end{bmatrix} \right\} \quad (\text{D.1})$$

Where the relationship between the true angular rate ω and estimated angular rate $\hat{\omega}$ is given in Equation (4.5) as:

$$\omega = \hat{\omega} - (\delta b + \eta_v) \quad (\text{D.2})$$

Substituting into the above $\delta\dot{\bar{q}}(t)$ equation:

$$\begin{aligned} \delta\dot{\bar{q}}(t) &= \frac{1}{2} \left\{ \begin{bmatrix} \hat{\omega} \\ 0 \end{bmatrix} \otimes \delta\bar{q}(t) - \delta\bar{q}(t) \otimes \begin{bmatrix} \hat{\omega} \\ 0 \end{bmatrix} \right\} - \frac{1}{2} \begin{bmatrix} \delta b + \eta_v \\ 0 \end{bmatrix} \otimes \delta\bar{q}(t) \\ &= \frac{1}{2} \left\{ \begin{bmatrix} -\hat{\omega} \times & \hat{\omega} \\ -\hat{\omega}^T & 0 \end{bmatrix} \cdot \delta\bar{q}(t) - \begin{bmatrix} +\hat{\omega} \times & \hat{\omega} \\ -\hat{\omega}^T & 0 \end{bmatrix} \cdot \delta\bar{q}(t) \right\} - \frac{1}{2} \begin{bmatrix} -(\delta b + \eta_v) \times & (\delta b + \eta_v) \\ -(\delta b + \eta_v)^T & 0 \end{bmatrix} \cdot \delta\bar{q}(t) \quad (\text{D.3}) \\ &= \frac{1}{2} \left\{ \begin{bmatrix} -2\hat{\omega} \times & \mathbf{0}_{3 \times 1} \\ -\mathbf{0}_{3 \times 1}^T & 0 \end{bmatrix} \cdot \delta\bar{q}(t) \right\} - \frac{1}{2} \begin{bmatrix} -(\delta b + \eta_v) \times & (\delta b + \eta_v) \\ -(\delta b + \eta_v)^T & 0 \end{bmatrix} \cdot \delta\bar{q}(t) \end{aligned}$$

For small angle rotation, $\delta\bar{q}(t) = \begin{bmatrix} \delta\rho \\ \delta q_4 \end{bmatrix} \approx \begin{bmatrix} \delta\rho \\ 1 \end{bmatrix}$ and replace the above equation yields:

$$\delta\dot{\bar{q}}(t) = \left\{ \begin{bmatrix} -\hat{\omega} \times & \mathbf{0}_{3 \times 1} \\ -\mathbf{0}_{3 \times 1}^T & 0 \end{bmatrix} - \frac{1}{2} \begin{bmatrix} -(\delta b + \eta_v) \times & (\delta b + \eta_v) \\ -(\delta b + \eta_v)^T & 0 \end{bmatrix} \right\} \cdot \begin{bmatrix} \delta\rho \\ 1 \end{bmatrix} \quad (\text{D.4})$$

Neglecting the second order terms $O(\delta b \cdot \delta \rho)$ and $O(\eta_v \cdot \delta \rho)$:

$$\delta \dot{\bar{q}}(t) = \begin{bmatrix} \delta \dot{\rho} \\ \delta \dot{q}_4 \end{bmatrix} \approx \begin{bmatrix} -[\hat{\omega} \times] \delta \rho - \frac{1}{2}(\delta b + \eta_v) \\ 0 \end{bmatrix} \quad (\text{D.5})$$

D.2: Derivation of Quaternion Transition Matrix

Quaternion differential equation is given by:

$$\dot{\bar{q}} = \begin{bmatrix} \dot{q}_1 \\ \dot{q}_2 \\ \dot{q}_3 \\ \dot{q}_4 \end{bmatrix} = \frac{1}{2} \Omega(\omega) \bar{q} \quad (\text{D.6})$$

In discrete-time form, this first order differential equation can be solved by integrating the quaternions, thus the quaternion transition matrix is expressed as:

$$\Phi_q(\omega) = \exp\left(\int_k^{k+1} \frac{1}{2} \Omega(\omega) dt\right) \quad (\text{D.7})$$

Assume the rotation rate is constant over the integration period $\Delta t = t_{k+1} - t_k$, then:

$$\Phi_q(\omega) = \exp\left(\frac{1}{2} \Omega(\omega) \Delta t\right)$$

From Taylor series expansion:

$$\Phi_q(\omega) = I_{4 \times 4} + \frac{1}{2} \Omega(\omega) \Delta t + \frac{1}{2!} \left(\frac{1}{2} \Omega(\omega) \Delta t\right)^2 + \frac{1}{3!} \left(\frac{1}{2} \Omega(\omega) \Delta t\right)^3 + \dots \quad (\text{D.8})$$

The symmetric skew matrix $\Omega(\omega)$ has the following properties:

$$\Omega(\omega) = \begin{bmatrix} -\omega \times & \omega \\ -\omega^T & 0 \end{bmatrix} = \begin{bmatrix} 0 & \omega_z & -\omega_y & \omega_x \\ -\omega_z & 0 & \omega_x & \omega_y \\ \omega_y & -\omega_x & 0 & \omega_z \\ -\omega_x & -\omega_y & -\omega_z & 0 \end{bmatrix}$$

$$\Omega(\omega)^2 = -|\omega|^2 I_{4 \times 4}$$

$$\Omega(\omega)^3 = -|\omega|^2 \Omega(\omega)$$

$$\Omega(\omega)^4 = |\omega|^4 I_{4 \times 4}$$

$$\Omega(\omega)^5 = |\omega|^4 \Omega(\omega)$$

$$\Omega(\omega)^6 = -|\omega|^6 I_{4 \times 4}$$

...

(D.9)

Substituting each item into Equation (D.8) yields:

$$\begin{aligned} \Phi_q(\omega) &= \left(1 - \frac{1}{2!} \left(\frac{1}{2} \Delta t\right) |\omega|^2 + \frac{1}{4!} \left(\frac{1}{2} \Delta t\right)^4 |\omega|^4 + \dots\right) I_{4 \times 4} + \left(\frac{1}{2} |\omega| \Delta t - \frac{1}{3!} \left(\frac{1}{2} |\omega| \Delta t\right)^3 + \frac{1}{5!} \left(\frac{1}{2} |\omega| \Delta t\right)^5 + \dots\right) \frac{1}{|\omega|} \Omega(\omega) \\ &= \cos\left(\frac{1}{2} |\omega| \Delta t\right) I_{4 \times 4} + \frac{1}{|\omega|} \sin\left(\frac{1}{2} |\omega| \Delta t\right) \Omega(\omega) \end{aligned}$$

(D.10)

Merging the two items together into matrix form, $\Phi_q(\omega)$ can be obtained as:

$$\Phi_q(\omega) = \begin{bmatrix} \cos \frac{\|\theta\|}{2} I_{3 \times 3} - \widehat{\psi}_k^+ \times & \widehat{\psi}_k^+ \\ -\widehat{\psi}_k^{+T} & \cos \frac{\|\theta\|}{2} \end{bmatrix} = \begin{bmatrix} \cos \frac{\|\theta\|}{2} & \frac{\theta_z}{\|\theta\|} \sin \frac{\|\theta\|}{2} & -\frac{\theta_y}{\|\theta\|} \sin \frac{\|\theta\|}{2} & \frac{\theta_x}{\|\theta\|} \sin \frac{\|\theta\|}{2} \\ -\frac{\theta_z}{\|\theta\|} \sin \frac{\|\theta\|}{2} & \cos \frac{\|\theta\|}{2} & \frac{\theta_x}{\|\theta\|} \sin \frac{\|\theta\|}{2} & \frac{\theta_y}{\|\theta\|} \sin \frac{\|\theta\|}{2} \\ \frac{\theta_y}{\|\theta\|} \sin \frac{\|\theta\|}{2} & -\frac{\theta_x}{\|\theta\|} \sin \frac{\|\theta\|}{2} & \cos \frac{\|\theta\|}{2} & \frac{\theta_z}{\|\theta\|} \sin \frac{\|\theta\|}{2} \\ -\frac{\theta_x}{\|\theta\|} \sin \frac{\|\theta\|}{2} & -\frac{\theta_y}{\|\theta\|} \sin \frac{\|\theta\|}{2} & -\frac{\theta_z}{\|\theta\|} \sin \frac{\|\theta\|}{2} & \cos \frac{\|\theta\|}{2} \end{bmatrix} \quad (\text{D.11})$$

Where:

$$\theta_i = \omega_i \Delta t \quad i=x,y,z$$

$$\|\theta\| = \sqrt{\omega_x^2 + \omega_y^2 + \omega_z^2} \Delta t$$

D.3: Derivation of State Transition Matrix Φ

The derivation of state transition matrix Φ is as follows:

$$\delta \dot{\alpha} = -[\hat{\omega} \times] \delta \alpha - (\Delta \beta + \eta_v) \quad (\text{D.12})$$

This is a typical first-order non-homogeneous linear differential equation:

$$\dot{X}(t) = A(t)X(t) + B(t)U(t) \quad (\text{D.13})$$

The general solution is:

$$X(t) = \Phi(t, t_0)X(t_0) + \int_{t_0}^t \Phi(t, \tau)B(\tau)U(\tau)d\tau \quad (\text{D.14})$$

$$\Phi(t, t_0) = e^{\int_{t_0}^t A(\tau)d\tau}$$

In discrete-time, the solution of above equation is:

$$\begin{aligned}\alpha_{k+1} &= e^{-\int_k^{k+1} [\omega \times] dt} \cdot \alpha_k + \int_k^{k+1} [-(\Delta\beta + \eta_v)] e^{-\int_k^{k+1} [\omega \times] dt} dt \\ &= e^{-[\omega \times] \Delta t} \alpha_k - (\Delta\beta + \eta_v) \int_k^{k+1} e^{-[\omega \times] \Delta t} dt\end{aligned}\quad (\text{D.15})$$

Dividing the transition matrix with the following block structure:

$$\Phi = \begin{bmatrix} \Phi_{00} & \Phi_{10} \\ 0 & I_{3 \times 3} \end{bmatrix}\quad (\text{D.16})$$

Where $\Phi_{00} = e^{-[\omega \times] \Delta t}$

$$\Phi_{10} = -\int_k^{k+1} e^{-[\omega \times] \Delta t} dt$$

In discrete time:

$$\begin{aligned}\Phi_{00} &= e^{-[\omega \times] \Delta t} = e^{-[\theta \times]} = I - (\theta \times) + \frac{(\theta \times)^2}{2!} - \frac{(\theta \times)^3}{3!} + \frac{(\theta \times)^4}{4!} - \frac{(\theta \times)^5}{5!} \dots \\ (\theta \times)^2 &= \begin{bmatrix} -(\theta_y^2 + \theta_z^2) & \theta_x \theta_y & \theta_x \theta_z \\ \theta_x \theta_y & -(\theta_x^2 + \theta_z^2) & \theta_y \theta_z \\ \theta_x \theta_z & \theta_y \theta_z & -(\theta_x^2 + \theta_y^2) \end{bmatrix}\end{aligned}\quad (\text{D.17})$$

$$(\theta \times)^3 = -(\theta_x^2 + \theta_y^2 + \theta_z^2) [\theta \times] = -\|\theta\|^2 [\theta \times]$$

$$(\theta \times)^4 = -(\theta_x^2 + \theta_y^2 + \theta_z^2)[\theta \times]^2 = -\|\theta\|^2 [\theta \times]^2$$

...

Organizing the above items:

$$\begin{aligned} \Phi_{00} &= I - (\theta \times) + \frac{(\theta \times)^2}{2!} + \frac{\|\theta\|^2 (\theta \times)}{3!} - \frac{\|\theta\|^2 (\theta \times)^2}{4!} - \frac{\|\theta\|^4 (\theta \times)}{5!} \dots \\ &= I - \left[1 - \frac{\|\theta\|^2}{3!} + \frac{\|\theta\|^4}{5!} - \dots \right] (\theta \times) + \left[\frac{1}{2!} - \frac{\|\theta\|^2}{4!} + \frac{\|\theta\|^4}{6!} - \dots \right] (\theta \times)^2 \\ &= I - \frac{\sin(\|\theta\|)}{\|\theta\|} (\theta \times) + \frac{1 - \cos(\|\theta\|)}{\|\theta\|^2} (\theta \times)^2 \end{aligned} \tag{D.18}$$

Where:

$$[\theta \times] = \begin{bmatrix} 0 & -\theta_z & \theta_y \\ \theta_z & 0 & -\theta_x \\ -\theta_y & \theta_x & 0 \end{bmatrix} = \begin{bmatrix} 0 & -\omega_z & \omega_y \\ \omega_z & 0 & -\omega_x \\ -\omega_y & \omega_x & 0 \end{bmatrix} \Delta t$$

$$(\theta \times)^2 = \begin{bmatrix} -(\theta_y^2 + \theta_z^2) & \theta_x \theta_y & \theta_x \theta_z \\ \theta_x \theta_y & -(\theta_x^2 + \theta_z^2) & \theta_y \theta_z \\ \theta_x \theta_z & \theta_y \theta_z & -(\theta_x^2 + \theta_y^2) \end{bmatrix}$$

Denoting Φ_{10} as:

$$\Phi_{10} = -\int_k^{k+1} e^{-[\omega \times] \Delta t} dt = -M(t)$$

Then:

$$\begin{aligned}
M(t) &= \int_k^{k+1} e^{-[\omega \times] \Delta t} dt = \int_k^{k+1} e^{-[\theta \times]} dt = \int_k^{k+1} \left[I - (\theta \times) + \frac{(\theta \times)^2}{2!} - \frac{(\theta \times)^3}{3!} + \frac{(\theta \times)^4}{4!} - \frac{(\theta \times)^5}{5!} \dots \right] dt \\
&= \Delta t - \int_k^{k+1} (\theta \times) dt + \int_k^{k+1} \frac{(\theta \times)^2}{2!} dt - \int_k^{k+1} \frac{(\theta \times)^3}{3!} dt + \int_k^{k+1} \frac{(\theta \times)^4}{4!} dt - \int_k^{k+1} \frac{(\theta \times)^5}{5!} dt + \dots
\end{aligned} \tag{D.19}$$

Where:

$$\begin{aligned}
\int_k^{k+1} (\theta \times) dt &= \int_k^{k+1} \begin{bmatrix} 0 & -\omega_z & \omega_y \\ \omega_z & 0 & -\omega_x \\ -\omega_y & \omega_x & 0 \end{bmatrix} dt = (\omega \times) \cdot \frac{\Delta t^2}{2} = \frac{(\theta \times)}{2} \Delta t \\
\int_k^{k+1} \frac{(\theta \times)^2}{2!} dt &= \frac{1}{2!} \int_k^{k+1} \begin{bmatrix} -(\omega_y^2 + \omega_z^2) & \theta_x \theta_y & \theta_x \theta_z \\ \theta_x \theta_y & -(\theta_x^2 + \theta_z^2) & \theta_y \theta_z \\ \theta_x \theta_z & \theta_y \theta_z & -(\theta_x^2 + \theta_y^2) \end{bmatrix} dt \\
&= \frac{1}{2!} \int_k^{k+1} \begin{bmatrix} -(\omega_y^2 + \omega_z^2) & \omega_x \omega_y & \omega_x \omega_z \\ \omega_x \omega_y & -(\omega_x^2 + \omega_z^2) & \omega_y \omega_z \\ \omega_x \omega_z & \omega_y \omega_z & -(\omega_x^2 + \omega_y^2) \end{bmatrix} t^2 dt \\
&= \frac{(\omega \times)^2}{2!} \int_k^{k+1} t^2 dt = \frac{(\omega \times)^2}{2!} \cdot \frac{\Delta t^3}{3} = \frac{(\omega \times)^2 \Delta t^3}{3!} = \frac{(\theta \times)^2}{3!} \Delta t
\end{aligned}$$

$$\begin{aligned}
\int_k^{k+1} \frac{(\theta \times)^3}{3!} dt &= \frac{1}{3!} \int_k^{k+1} [(-\|\theta\|^2)(\theta \times)] dt = -\frac{1}{3!} \int_k^{k+1} [(\|\omega\|^2 t^2)(\theta \times)] dt \\
&= -\frac{\|\omega\|^2}{3!} \int_k^{k+1} t^2 \cdot \begin{bmatrix} 0 & -\omega_z & \omega_y \\ \omega_z & 0 & -\omega_x \\ -\omega_y & \omega_x & 0 \end{bmatrix} dt \\
&= -\frac{\|\omega\|^2 \cdot (\omega \times)}{3!} \int_k^{k+1} t^3 dt = -\frac{\|\omega\|^2 \cdot (\omega \times)}{3!} \cdot \frac{\Delta t^4}{4} \\
&= -\frac{\|\omega\|^2 \cdot (\omega \times) \Delta t^4}{4!} = -\frac{\|\theta\|^2 \cdot (\theta \times)}{4!} \Delta t
\end{aligned}$$

$$\begin{aligned}
\int_k^{k+1} \frac{(\theta \times)^4}{4!} dt &= \frac{1}{4!} \int_k^{k+1} [-\|\theta^2\| \cdot (\theta \times)^2] dt = -\frac{1}{4!} \int_k^{k+1} [(\|\omega\|^2 t^2)(\theta \times)^2] dt \\
&= -\frac{\|\omega\|^2}{4!} \int_k^{k+1} t^2 \cdot \begin{bmatrix} -(\theta_y^2 + \theta_z^2) & \theta_x \theta_y & \theta_x \theta_z \\ \theta_x \theta_y & -(\theta_x^2 + \theta_z^2) & \theta_y \theta_z \\ \theta_x \theta_z & \theta_y \theta_z & -(\theta_x^2 + \theta_y^2) \end{bmatrix} dt \\
&= -\frac{\|\omega\|^2}{4!} \int_k^{k+1} t^2 \cdot \begin{bmatrix} -(\omega_y^2 + \omega_z^2) & \omega_x \omega_y & \omega_x \omega_z \\ \omega_x \omega_y & -(\omega_x^2 + \omega_z^2) & \omega_y \omega_z \\ \omega_x \omega_z & \omega_y \omega_z & -(\omega_x^2 + \omega_y^2) \end{bmatrix} t^2 dt \\
&= -\frac{\|\omega\|^2 \cdot (\omega \times)^2}{4!} \int_k^{k+1} t^4 dt = -\frac{\|\omega\|^2 \cdot (\omega \times)^2}{4!} \cdot \frac{\Delta t^5}{5} \\
&= -\frac{\|\theta\|^2 \cdot (\theta \times)^2}{5!} \Delta t
\end{aligned}$$

$$\begin{aligned}
\int_k^{k+1} \frac{(\theta \times)^5}{5!} dt &= \frac{1}{5!} \int_k^{k+1} [(\|\theta\|^4)(\theta \times)] dt = \frac{1}{5!} \int_k^{k+1} [(\|\omega\|^4 t^4)(\theta \times)] dt \\
&= \frac{\|\omega\|^4}{5!} \int_k^{k+1} t^4 \cdot \begin{bmatrix} 0 & -\omega_z & \omega_y \\ \omega_z & 0 & -\omega_x \\ -\omega_y & \omega_x & 0 \end{bmatrix} t dt \\
&= \frac{\|\omega\|^4 \cdot (\omega \times)}{5!} \int_k^{k+1} t^5 dt = \frac{\|\omega\|^4 \cdot (\omega \times)}{5!} \cdot \frac{\Delta t^6}{6} \\
&= \frac{\|\omega\|^4 \cdot (\omega \times) \Delta t^6}{6!} = \frac{\|\theta\|^4 \cdot (\theta \times)}{6!} \Delta t
\end{aligned}$$

$$\begin{aligned}
\int_k^{k+1} \frac{(\theta \times)^6}{6!} dt &= \frac{1}{6!} \int_k^{k+1} [\|\theta^4\| \cdot (\theta \times)^2] dt = \frac{1}{6!} \int_k^{k+1} [(\|\omega\|^4 t^4)(\theta \times)^2] dt \\
&= \frac{\|\omega\|^4}{6!} \int_k^{k+1} t^4 \cdot \begin{bmatrix} -(\theta_y^2 + \theta_z^2) & \theta_x \theta_y & \theta_x \theta_z \\ \theta_x \theta_y & -(\theta_x^2 + \theta_z^2) & \theta_y \theta_z \\ \theta_x \theta_z & \theta_y \theta_z & -(\theta_x^2 + \theta_y^2) \end{bmatrix} dt \\
&= \frac{\|\omega\|^4}{6!} \int_k^{k+1} t^4 \cdot \begin{bmatrix} -(\omega_y^2 + \omega_z^2) & \omega_x \omega_y & \omega_x \omega_z \\ \omega_x \omega_y & -(\omega_x^2 + \omega_z^2) & \omega_y \omega_z \\ \omega_x \omega_z & \omega_y \omega_z & -(\omega_x^2 + \omega_y^2) \end{bmatrix} t^2 dt \\
&= \frac{\|\omega\|^4 \cdot (\omega \times)^2}{6!} \int_k^{k+1} t^6 dt = \frac{\|\omega\|^4 \cdot (\omega \times)^2}{6!} \cdot \frac{\Delta t^7}{7} \\
&= \frac{\|\theta\|^4 \cdot (\theta \times)^2}{7!} \Delta t
\end{aligned}$$

As a result:

$$\begin{aligned}
M(t) &= \Delta t - \frac{(\theta \times)}{2} \Delta t + \frac{(\theta \times)^2}{3!} \Delta t + \frac{\|\theta\|^2 \cdot (\theta \times)}{4!} \Delta t - \frac{\|\theta\|^2 \cdot (\theta \times)^2}{5!} \Delta t - \frac{\|\theta\|^4 \cdot (\theta \times)}{6!} \Delta t + \frac{\|\theta\|^4 \cdot (\theta \times)^2}{7!} \Delta t - \dots \\
&= \Delta t - \left(\frac{1}{2!} \frac{\|\theta\|^2}{4!} + \frac{\|\theta\|^4}{6!} - \dots \right) (\theta \times) \Delta t + \left(\frac{1}{3!} - \frac{\|\theta\|^2}{5!} + \frac{\|\theta\|^4}{7!} - \dots \right) (\theta \times)^2 \Delta t \\
&= \Delta t - \frac{1 - \cos(\|\theta\|)}{\|\theta\|^2} (\theta \times) \Delta t + \frac{\|\theta\| - \sin(\|\theta\|)}{\|\theta\|^3} (\theta \times)^2 \Delta t
\end{aligned} \tag{D.20}$$

Then:

$$\begin{aligned}
\Phi_{10} &= -M(t) \\
&= -\Delta t + \frac{1 - \cos(\|\theta\|)}{\|\theta\|^2} (\theta \times) \Delta t - \frac{\|\theta\| - \sin(\|\theta\|)}{\|\theta\|^3} (\theta \times)^2 \Delta t \\
&= \frac{1 - \cos(\|\theta\|)}{\|\theta\|^2} (\theta \times) \Delta t - \frac{\|\theta\| - \sin(\|\theta\|)}{\|\theta\|^3} (\theta \times)^2 \Delta t - \Delta t \\
&= \left[\frac{1 - \cos(\|\theta\|)}{\|\theta\|^2} (\theta \times) - \frac{\|\theta\| - \sin(\|\theta\|)}{\|\theta\|^3} (\theta \times)^2 - I_{3 \times 3} \right] \Delta t
\end{aligned} \tag{D.21}$$

Thus:

$$\begin{aligned}
\Phi_{10} &= \frac{1 - \cos(\|\omega\| \Delta t)}{\|\omega\|^2} (\omega \times) - \frac{\|\omega\| \Delta t - \sin(\|\omega\| \Delta t)}{\|\omega\|^3} (\omega \times)(\omega \times) - I_{3 \times 3} \Delta t \\
&= \left[\frac{1 - \cos(\|\theta\|)}{\|\theta\|^2} (\theta \times) - \frac{\|\theta\| - \sin(\|\theta\|)}{\|\theta\|^3} (\theta \times)(\theta \times) - I_{3 \times 3} \right] \Delta t
\end{aligned} \tag{D.22}$$